A Practical Investigation into the Measurement of Forces on the Stator Teeth of Electrical Machines

By

Graeme Rhys Bevan

Submitted to the Department of Electrical Engineering in Fulfilment of the Requirements for the Magister Technologiae in Electrical Engineering at the

CAPE PENINSULA UNIVERSITY OF TECHNOLOGY

SUPERVISOR: E. VOSS

NOVEMBER 2013

Declaration

I, GRAEME BEVAN, submit this thesis in fulfilment of the requirements of the degree of Magister Technologiae (MTech) in Electrical Engineering.

I claim that this is my own original work and that it has not been submitted in this or similar form for a degree at any other tertiary institution.

…….

Graeme Bevan

CANDIDATE

16 / 10 / 2013

…….

DATE

CPUT, Cape Town Campus

……..

PLACE

Acknowledgements

I wish to express my gratitude to all of the following:

- God the Father, Son and Holy Spirit to whom I owe all that I am
- Mr Egon Voss, my supervisor, for his guidance, support and expert advice throughout this project
- The Centre for Postgraduate Studies at CPUT for funding provided
- Andrew Fitzsimmons for his availability, patience and priceless practical input
- Jacques Wheeler at the Centre for Instrumentation Research for sharing his valuable advice and time so freely
- Jonathan Sturgess and Mark Timothy at Alstom Grid UK for their thorough advice regarding electromagnetics and finite element modelling
- Roger Wang at Stellenbosch University for his advice on magnetic circuits
- Andre Veldman at Esteq Engineering for all his help regarding my measurement system
- Andy Meldrum at Oceantech for his help with the silicon steel used in this project
- Rob and the team at Eloff Transformers for their generous assistance
- Patrick Tippoo for wise counsel and continuous encouragement
- My family who always believed in me and have helped in so many ways
- My friends, Robert Smith, Willem Stemmet, Ben de Jager, Matthew Golding and Rochelle Ebel for all their positive input along this journey

Synopsis

Radial and peripheral displacement of stator teeth in electrical machines is known to be the cause of undesired vibration which leads to noise. This thesis serves to investigate the possibility of physically measuring the radial displacement of stator teeth caused by electromagnetic forces which, to the author's knowledge, has not yet been achieved. A simplified practical approach is adopted in order to address the inherent difficulties attached to this problem, and the measurement of displacement is done by means of an experimental rig where a tooth is subjected to magnetic force acting over an air gap.

Three experiments are carried out, each comprising ten tests, the results of which are compared in order to gain some idea as to the magnitudes of displacement which can be expected over a range of applied air gap flux densities. The aim of this work is to observe the displacement response of magnetised EM core material when acted upon by forces, and to see if the measured results agree with the elastic displacement predicted by a well-known formula. It will be shown that although the measured results are in the same range as the predicted results, there is a deviation from the predicted linearity due to certain characteristics of the force rig, which are explained.

The chosen measurement method is capacitive displacement and is shown to be a viable alternative to the more commonly used search coils and vibrometers in past literatures, especially when measuring displacements on the nano-scale. In addition, this study shows the importance of using 3D finite element software to simulate the electromagnetic model when saturation is present in the core of the test specimen. The important findings of this work are discussed in detail, and some ideas put forward, in an attempt to establish a starting point for future related work in the measurement of electromagnetic force-induced displacement of stator teeth in electrical machines.

Table of Contents

List of Figures and Tables

Table **Title** **Page**

List of Symbols and Abbreviations

Roman alphabet

A	Area, m^2
A_{con}	Cross-sectional area of conductor, m^2
A_g	Cross-sectional area of air gap, m^2
A_{path}	Area of a defined path, m^2
$\vec{A}$	Magnetic vector potential, Vs/m
b	Curve fitting coefficient, no unit
$\vec{B}$	Magnetic flux density, T
B_g	Flux density in the air gap, T
B_{gt}	Flux density in the air gap over a specific time, T
$B_{c(ave)}$	Average value for the flux density in the core, T
B_n	Normal component of flux density, T
B_t	Tangential component of flux density, T
c_{con}	Specific heat characteristic of conductor, J/kg°C
d	Distance, m
E	Young's modulus or modulus of elasticity, N/m^2 or Pa
E_{con}	Energy dissipated by conductor, J
f	Frequency, Hz
$\vec{f}_{vw}$	Force density according to virtual work principle, N/m^3
F	Force, N
F_{ave}	Average force, N
F_n	Normal component of force, N
F_t	Tangential component of force, N
$\vec{H}$	Magnetic field strength, A/m

H_g	Magnetic field strength in the air gap, A/m
$H_{c(ave)}$	Average value for magnetic field strength in the core, A/m
i	Instantaneous value for electric current, A
i_p	Peak instantaneous value of electric current, A
I	Current, A
$I_{\Delta Tmax}$	Current effecting maximum temperature change, A
$\vec{J}$	Current density, A/m^2
K	Constant value, no unit
ℓ	Length, m
ℓ_1	Original length of an object, m
ℓ_2	Length of an object after a dimensional change, m
ℓ_c	Length of a path defined through a core, m
ℓ_{con}	Length of conductor, m
ℓ_g	Length of a path defined through an air gap, m
ℓ_{path}	Length of a defined path, m
ℓ_s	Length of a stack of laminations, m
ℓ_x	Length in the x-direction, m
ℓ_{x1}	Original length of an object in the x direction, m
ℓ_{x2}	Length of an object in the x-direction after a dimensional change in the x direction, m
L	Inductance, Vs/A
M_{con}	Mass of conductor, kg
M_s	Magnetic field strength at saturation, A/m
N	Number of turns, no unit
P_{con}	Power dissipated by conductor, W
R	Resistance, Ω
R_{con}	Resistance of conductor, Ω
$\Re$	Reluctance, At/Vs

$\Re_g$ Reluctance of the air gap, At/Vs

$\Re_{cct}$ Reluctance in the circuit, At/Vs

$\Re_{iron}$ Reluctance of the iron, At/Vs

t Time, s

t_{max} Maximum time duration, s

T_{con} Temperature of conductor, °C

V Voltage, V

V_{con} Volume of conductor, m^3

X_l Inductive reactance, Ω

X_c Capacitive reactance, Ω

Greek alphabet

δ Delta, indicates length, m

Δ Delta, indicates a change in the parameter to which it is attached, no unit

ε Epsilon, indicates strain, no unit

ε_x Unit change in length along the x-axis

ε_y Unit change in length along the y-axis

ε_z Unit change in length along the z-axis

ε_r Permittivity to an electric field relative to the permittivity of air, As/Vm

ε_0 Permittivity of air to an electric field, As/Vm

Γ Gamma, indicates a closed contour, no unit

Λ Lambda, indicates magnetic permeance, Vs/At

μ Mu, indicates magnetic permeability, Vs/Am

μ_0 Magnetic permeability of free space (air), Vs/Am

μ_{iron} Magnetic permeability of iron, Vs/Am

μ_r Magnetic relative permeability (relative to that of free space), no unit

ν Nu, indicates Poisson's ratio, no unit

Φ Phi, indicates magnetic flux, Vs

Φ_g	Magnetic flux in the air gap, Vs
ρ	Rho, indicates mass density, kg/m^3
ρ_{con}	Density of conductor, kg/m^3
σ	Sigma, indicates stress, N/m^2 or Pa
σ_{ave}	Average stress over a specific area, N/m^2 or Pa
σ_n	Normal component of stress, N/m^2 or Pa
σ_t	Tangential component of stress, N/m^2 or Pa
ω	Omega, indicates angular velocity, rad/s

Abbreviations

CCD	Charge coupled device
EM	Electrical machine
FBG	Fibre Bragg grating
FE	Finite element
FSO	Full scale output
IM	Induction motor
LAS	Law of approach to saturation
MMF	Magnetomotive force
MST	Maxwell stress tensor
NP	North pole
PMSM	Permanent magnet synchronous machine
RD	Rolling direction
RSM	Reluctance synchronous machine
SP	South pole
SRM	Switched reluctance machine
TD	Transverse direction
VRM	Variable reluctance motor

Chapter 1

Introduction

As life is manifested by movement – made up of actions, reactions, and complex interactions involving a variety of forces – it can be said that no measurement is more essential to human activity than force measurement in its many forms (weight, energy, work, torque, acceleration and pressure). There are four elementary forces found in nature: strong nuclear, electromagnetic, weak nuclear and gravitational. (Griffiths, 1999)

This work is interested in electromagnetic forces which are the primary forces acting in electrical machines (EMs). Magnetic forces will act on a ferrous body when subjected to a magnetic field. This is the principle whereby EMs operate, where air gap forces acting on the rotor produce torque and electrical energy is converted to mechanical energy or vice versa. Electromechanical energy conversion takes place in the air gap of a machine, where the force has two components, namely, radial and peripheral. Noise and vibration of the stator structure are the unwanted by-products of the radial and peripheral forces acting on the stator teeth, and therefore a correct knowledge of the distribution of these forces is useful when trying to reduce these phenomena. It is possible to predict the forces acting on the magnetised parts of an EM by various methods of calculation – the Maxwell stress tensor (MST), virtual work principle, equivalent magnetic charge and equivalent current density being the most popular. These methods are all in agreement and have been proved relatively accurate where the calculation of total force acting on a body is concerned, but give very different local force distributions.

The aim of this work is to investigate the measurement of displacement caused by electromagnetic force acting on a stator tooth. This force is not in the centre of the air gap and will not produce torque, contributing only to the displacement of the tooth. For practical reasons, only the radial displacement of the tooth will be investigated – by means of an experimental force rig – with the intention of laying a foundation for future research into the measurement of such force-induced displacements in EMs.

1.1 Literature review

At the beginning of the twentieth century, the basic contributions with respect to the mechanical force which is exerted by electromagnetic circuits came from Ampere, Kelvin and Maxwell. Subsequent developments on this subject were largely due to the application of their associated fundamental equations. A valuable contribution was made by Steinmetz (1911) on the mechanical forces in magnetic fields, which took a first step toward deriving a general equation for the force exerted by a single circuit. A general equation was then proposed by Doherty and Park (1926) for a multi-circuit system.

A method for the calculation of magnetic force on disconnecting switches was proposed by Dwight (1920), which Roper (1927) attempted to validate by conducting a series of experiments on circular and rectangular circuits and measuring the force by using a lever arm and scale pan with offsetting weights, obtaining agreement to within ten percent of theory to practice. Then Seletzky and Priday (1935) proposed a new method for experimentally validating Dwight's formula by making use of a simple impedance bridge to measure the change of inductance as the switch disconnects, successfully reducing the margin of disagreement between theory and practice to around three percent.

Moving into the second half of the twentieth century, Lee (1957) alluded to the fact that although there were methods available at the time for calculating forces and force densities, the theories differed considerably and gave completely different force densities. He concluded it was actually not necessary to know the differences between the methods if only global (total) force was required, as each theory might be different in differential form (giving force at any one point in the system), but the integrals of each theory (predicting total system performance) might all arrive at the same result. He also conceded there was no experimental information available to verify any one of them.

Carpenter (1959) then presented a new numerical method of implementing a MST for calculating the force exerted on iron parts subject to a magnetic field, which expressed the mechanical force on the iron by means of integrating over a surface. He argued that the common interpretation of Maxwell field stress in iron was incorrect and also that

force calculation by means of surface integrals was a more accurate and simpler approach than the widely accepted virtual work method.

Three decades later, Reyne, *et al.* (1987) presented a paper focusing on magnetic forces with the aim of understanding the complex problems of vibration and noise in EMs. A comparison between "theories based on a simplified magnetisation model" and "theories based on an energy approach" (virtual works) concluded energy methods appeared to be more appropriate. However, the authors warned that limits and uncertainties attached to the subject remained and only a combination of experimental and numerical works would make their solution(s) possible.

There have been numerous holistic publications comparing the various known methods of calculating force, from the likes of Reichert, *et al.* (1976), Ito, *et al.* (1990), Muller (1990), Ren (1994), Belahcen (1999) and Vandevelde and Melkebeek (2001) to name but a few. It is clear from the literature that the resultant local force distribution is different for each method, while all the methods agree on the global force calculated. Hence the challenge remains to physically demonstrate by experiments which method gives the most realistic force distribution.

A new method for determining force distribution and torque was then proposed by Kabashima, *et al.* (1988) by using magnetising currents and the finite element (FE) method – the calculated results being verified experimentally by measurements of flux density and displacement taken by a Gauss meter and load cells, respectively. These were built into a fundamental model constructed to functionally resemble a permanent magnet synchronous motor (PMSM), where the practical results showed close agreement to the theoretical model.

An experimental setup to determine the origins of acoustic noise in a variable reluctance motor (VRM) was then investigated by Cameron, *et al.* (1989) where measurements of current, acceleration and sound output were taken. Resonant vibrations of the stator resulting from the radial electromagnetic forces were identified as the dominant noise

source – the vibrations being at a maximum when a sufficiently large radial force harmonic coincided with a resonant stator frequency.

A few years later a system for the measurement of electromagnetic forces, vibration, noise and resonant frequencies on a squirrel-cage induction motor (IM) was proposed by Verma and Balan (1993) where forces acting on a stator tooth were determined from the induced voltage in a tooth-pitched search-coil; the induced voltage in the coil being proportional to the rate of change of flux linking with it and the forces being proportional to the square of the flux pulsating through the tooth. The same authors then followed up with a general analysis for the determination of radial forces in an IM (1994) that focused on the role played by the harmonic fields in the air gap and the effects of loading – the same method of measurement being used to determine the forces – and then a study on the vibration behaviour of EM stators by means of experimental modal analysis (1998).

Static and dynamic radial force characteristics due to eccentric rotor positioning in a switched reluctance machine (SRM) were then investigated by Garrigan, *et al.* (1999). A magnetic equivalent circuit model was developed to calculate instantaneous radial and tangential forces on the stator as well as global forces on the rotor. Validation was achieved by comparison between FE and experiments. The most interesting observation with regard to static characteristics was that the maximum radial force did not coincide with maximum excitation but rather with the point of saturation in the iron. With regard to dynamic characteristics it was found that by using voltage source excitation with parallel connected windings, natural flux balancing occurred and the radial forces were substantially reduced when compared with series connected windings. Simple pull-force tests were conducted on a test motor to confirm the force vs. current predictions of the static model, with relatively good agreement between experimental and analytical results.

At the turn of the twenty-first century, S. Lee, *et al.* (2000) again pointed out differences in the various force calculation methods known to date and indicated the necessity of force density formula analysis from a mechanical deformation viewpoint, concluding that the magnetic charge method was the most suitable for a mechanical deformation analysis.

Throughout the twentieth century, long-range magnetic forces and magnetostriction have been treated theoretically as separately occurring phenomena and vibrations and noise in EMs have been considered mainly in terms of the long-range forces. This view has been challenged in recent studies by Vandevelde and Melkebeek (2001) (2001) (2002) (2003) (2004), Delaere, *et al.* (2002), Belahcen (1999) (2004), and Shahaj (2010) who introduced the magnetic bimorph concept – a method of manipulating stator teeth magnetostriction so that selected components of the Maxwell force are cancelled out by components of magnetostrictive force. Methods for the measurement of magnetostriction have also been proposed by Vandevelde, *et al.* (2004), Ekreem, *et al.* (2007), Ghalamestani, *et al.* (2010) and Somkun, *et al.* (2012) amongst others.

In an attempt to physically validate a local force formulation, an experiment was conducted by Barre, *et al.* (n.d.), the results of which were compared to predicted deformations calculated with a FE package, using only the energy method (virtual works) to provide the local force density. The measured values were shown to be in close agreement with the simulated values and therefore the energy principle was proved reasonably accurate for determining the deformation of this particular test body – being linear and having specific properties – when subjected to an external magnetic field.

The same team then decided (2006) to compare the mathematically calculated results of four known local force formulations – namely; the equivalent currents method, the Maxwell stress method, the equivalent magnetic charges method and the virtual work (energy) principle – to results obtained from the same test bench as in the previous experiment. The formulation that provided the closest results to those measured in the experiment was that of the energy principle. This result was tested further by comparing the energy principle results to a test bench utilising an electric field instead of a magnetic field. The resulting deformation was again very close to that predicted by the energy principle. These findings are not, however, directly applicable to EMs, as the test body used in both cases was constructed of a gelatin-like ‘soft material’, bearing no relation to the silicon steel used for making the laminations that form the iron core of an EM.

A study conducted by Husain, *et al.* (2010) identified the dominating source of noise and vibration in low to medium power rated PMSMs as electromagnetic, the other two sources being aerodynamic and mechanical. Magnetic radial forces were shown to be the major electromagnetic contributor to noise and vibration as opposed to the torque ripple and cogging torque. Magnetic forces on the stator teeth were calculated by FE using the MST method, the resulting radial displacement along the teeth was predicted by an analytical model, and validation of theory was achieved through the mounting of accelerometers at four orthogonal positions on the stator housing to measure displacement, with closely matched results.

A complete vibration and acoustic analysis of a PMSM by 3-D FE modelling, validated by physical measurements, was performed by Torregrossa, *et al.* (2011) who agreed with the main findings of Husain, *et al.* but focused both on the radial and tangential (peripheral) forces. Torregrossa, *et al.* found that the tangential force peak values were significantly lower than the radial force peak values, but certain harmonics of the tangential force were in fact greater than their corresponding radial harmonic components. Vibration measurements on the external housing surface of the machine were done via laser vibrometer and acoustic measurements were taken via microphone, again showing close agreement with theoretical predictions.

1.2 Problem statement

When the rotating magnetic field in EMs traverses the iron-air boundary between rotor and stator, electromagnetic forces are induced on the stator teeth. Force gives rise to displacement and displacement gives rise to noise. These alternating magnetic forces are made up of two components, namely; radial and peripheral. Peripheral forces produce torque and are absolutely necessary for the operation of the machine. Radial forces do not contribute towards torque and are generally larger than the peripheral forces, making a significant and unnecessary contribution towards vibrations of the stator structure.

As it is not yet possible to measure these forces directly, they have to be derived from measurements of their related phenomena, i.e. displacement, flux density, acceleration of vibration etc. Traditionally, the forces inside a rotating EM have been measured by exploring coils embedded in the stator teeth which are able to measure a change in induced voltage from which the flux density and consequently the force acting on the teeth can be calculated. More recently, vibration sensors placed on the external stator housing have been used. The task of measuring electromagnetic force-induced displacement is a difficult one as these forces cause deflections on an extremely small scale. Moreover, to take measurements inside an EM during operation is even more difficult as the rotor is moving at high speed, the machine structure is completely sealed and the pattern of magnetic flux distribution must not be disturbed.

In order to avoid the pitfalls associated with taking such measurements in an EM, measurements could be taken on a physical model, emulating the conditions associated with force-induced tooth displacement caused by magnetic flux crossing an iron-air boundary. The problem would be to relate this model as closely as possible to an EM in order to obtain meaningful results.

In addition, as there still remains disagreement regarding the calculation of local electromagnetic force distribution (Lee, 1957) (Carpenter, 1959) (Reyne, 1987) (Ren, 1994) (Belahcen, 1999) (Lee, 2000) (Melkebeek, 2001) (Barre, 2006) (Sturgess, 2007) the only foreseeable way to solve this issue in future is by measurement.

1.3 Problem approach

The measurement of tooth displacement caused by radial forces will be attempted in this thesis. A ‘force rig’ will be designed, having a geometry emulating a stator tooth, air gap and rotor iron arrangement. A magnetostatic approach is adopted in order to simplify the practical and experimental conditions, as this work is intended to be a starting point in the measurement of electromagnetic force-induced tooth displacement. The force rig will be constructed of a laminated silicon steel core and energised by magnetic flux, where the average normal flux density in the air gap – and therefore the associated radial forces acting on the tooth – will be relative to that which occurs in the air gap of an EM.

An electromagnetic model of the force rig will be simulated on 2D FE software in order to get an idea of what magnitude of forces are induced on the tooth, when the average normal flux density in the air gap matches that of an EM. This is done to obtain a feeling for the forces created and whether they have a practical use or not. Once the force is known, the expected radial displacement of the tooth can be determined by means of a well-known formula for the deformation of linear elastic materials.

An investigation into the available measuring instruments – able to measure very small displacements and impervious to magnetic fields – will then be undertaken, and their measuring ranges noted. Once a suitable measuring technology is chosen, the design of the force rig(s) will begin. This design will be influenced by the measuring technique, and comprise all the characteristics as stipulated above. Excitation by means of dc coil(s) will be used to provide magnetic flux and, although not supported by experiments, the force production by ac sources will also be explained.

The goal of this thesis is to measure the elastic deformation of magnetised EM core material, which is due both to Maxwell forces and magnetostriction forces, as these two phenomena always naturally occur together. This work is only interested in the ‘end result’ of the elastic radial displacement of a tooth, and therefore a practical distinction is not made between Maxwell and magnetostriction forces. Experiments will be conducted on the force rig(s), in the hope of yielding results applicable to future work in EMs.

1.4 Outline of thesis

The layout of the remaining part of this thesis is as follows:

Chapter 2: In this chapter the focus is on EMs – in particular: the magnetoelastic nature and physical properties of their cores, their magnetic fields – with respect to ac and dc excitation, and the nature of the electromagnetic forces acting on the stator teeth.

Chapter 3: The aim of this chapter is to find the most suitable displacement measuring technology and then incorporate it in the force rig set up. The design process of the force rig(s) is also detailed.

Chapter 4: This chapter explains the test bench being utilised to perform the measurements, the concepts behind the experiments and how they are being done, and finally the results obtained in each case.

Chapter 5: The results of the experiments are analysed in this chapter in an attempt to shed some light on the tooth displacement responses exhibited by the force rig(s) in the previous chapter.

Chapter 6: Here the conclusions of the work are drawn and ideas toward possible future research are discussed. A summary of findings is presented, with some of the more important points being taken under consideration with a view toward future related work.

Chapter 2

Forces and electrical machines

2.1 Stress, strain and Hooke's law (Levinson, 1978)

The magnetic forces acting in EMs cause stresses to be induced in their cores and at iron-air boundaries. The silicon steel of which their cores are constructed is magnetoelastic in nature, meaning that it is able to change shape temporarily under magnetisation. The resulting deformations are usually very small but nevertheless do play an important role. The elastic nature of the core material is linked to the relation between stress and strain. Stress is a quantity describing the magnitude of force acting on a unit area. It has the same dimensions as pressure and is expressed in the same units – namely, newtons per metre squared, or Pascal. Force acting on an area causes a direct stress given by

$$\sigma_{ave} = \frac{F}{A}\left(\frac{N}{m^2}\right) \tag{2.1}$$

Direct stresses are simply those that can be determined by dividing force by area and fall into three categories, namely:

1. axial stress, resulting from pushing or pulling forces,
2. shear stress, resulting from forces exerting a tearing action, or
3. bearing stress, resulting from forces creating a contact (crushing) pressure.

Materials are often strong in one or two of these stress categories but will be weak in at least one of them. For example, a given metal may be strong in compression or tension but be weak in shear, or on the other hand another given metal's principle virtue may be its capability to withstand shearing forces, while being weak in compression and tension.

Stress is a quantity that is not directly measureable and is derived from measured strains in conjunction with certain other properties of the material. (Agilent Technologies, 1999)

According to Newton's third law of motion, for every action there is a reaction. Therefore, where there is stress, there will also be strain, and vice versa. Strain describes the physical change in form of a material. When an object is acted upon by pushing (compressive) or pulling (tensile) forces, it follows that its dimensions – length, width and depth – must change. Similarly, if a member is subjected to a torque or shearing stress, it will tend to twist, which is the case in the shafts of EMs. The stator teeth of an EM are subjected to magnetic tensile forces resulting in radial and peripheral stresses and strains, the former being the focus of this thesis. These force components are described in Section 2.4.3.

Axial strain describes a unit change in length along the axis of the applied force, which is defined as the measured length ℓ_2 of an object due to strain minus the original length ℓ_1 of the object, divided by the original length ℓ_1 of the object. This unit change in length can be defined along each of the x-, y- or z-coordinate axes, depending on the force applied. For example, a change in length along the x-axis caused by an axial stress is given by

$$\varepsilon_x = \frac{\ell_{x2} - \ell_{x1}}{\ell_{x1}} \text{ or } \frac{\Delta\ell_x}{\ell_x} \tag{2.2}$$

In the case of an EM, the axial stresses and strains caused by radial forces will be referred to as radial stresses and strains, to avoid any confusion with the axis of the machine.

Strain is denoted by ε and is a ratio quantity having no units. Therefore, a strain measurement of 0.1 may indicate a dimensional change of 0.1 millimetres per millimetre or 0.1 metres per metre, etc. When there is a change in length along the x-axis (for example) this will cause an object to experience a proportional change along the y- and/or z-axis as a result. A strain in the y- or z-direction may be described as a lateral strain in relation to an axial strain in the x-direction. In the early nineteenth century, a French mathematician named Poisson showed that the ratio of the lateral strain to the axial strain in elastic materials is a constant. This constant, called Poisson's ratio, denoted by ν, is defined as

$$\nu = \frac{\varepsilon_y}{\varepsilon_x} = \frac{\varepsilon_z}{\varepsilon_x} \tag{2.3}$$

Most metals have a Poisson's ratio that lies between the limits of $\frac{1}{3}$ and $\frac{1}{4}$.

The second elastic constant being a function of the given material's physical properties is the material's modulus of elasticity, or Young's modulus, denoted by E, and is named after the nineteenth century British scientist Thomas Young. This constant is defined as a ratio of the axial stress to the associated axial strain, shown by

$$E = \frac{\sigma}{\varepsilon} = \frac{F/A}{\Delta\ell/\ell} = \frac{F\ell}{A\Delta\ell} \tag{2.4}$$

The Young's modulus of a given material is found with the aid of stress-strain diagrams which are determined by experiments. Measurements of strain are taken by means of bonded resistance strain gauges, described in Section 3.1.1, as a function of a measurable increasing load on a standardised 'tensile bar'. Stress is then calculated at each increment in load based on the original cross-sectional area. From this information, the typical stress-strain graph of the given material is plotted, as shown in the example in Figure 2.1.

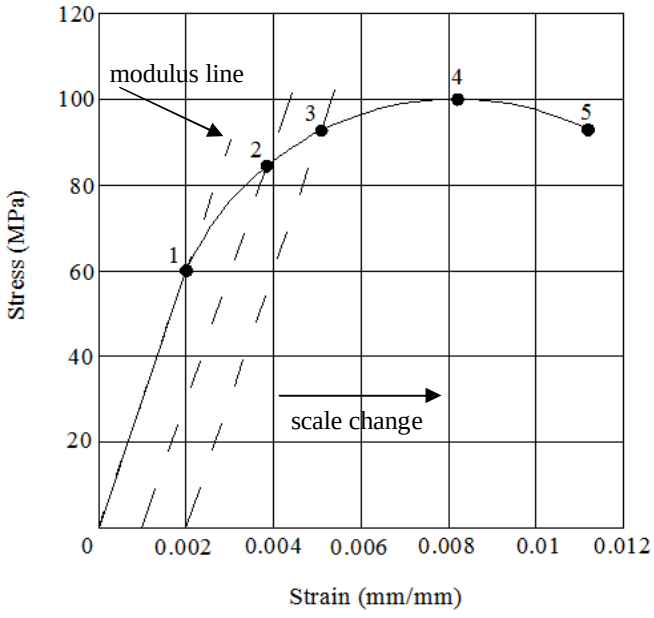

Where:

1 – Proportional limit

2 – Yield strength at 0.1% offset

3 – Yield strength at 0.2% offset

4 – Ultimate strength

5 – Rupture strength

Fig. 2.1 Typical stress-strain diagram, as redrawn from (Levinson, 1978)

Young's modulus describes the linear relationship of stress to strain that only holds true until the proportional limit of a material is reached. The modulus of elasticity is often a fictitious quantity as materials do not behave exactly as they should; therefore most design limits are kept well below the point at which stress and strain cease to have a proportional (linear) relationship. By not permitting the stress of a material to exceed the proportional limit, the material is assumed to elastically return to its original dimensions after stress removal.

The yield strength is the point at which strain begins to rapidly increase with little to no increase in stress. Beyond this point the material is said to deform plastically, meaning that if it is stressed beyond this point, and the stress is then removed, the material will not revert to its original dimensions, but will permanently retain a residual offset or strain. The ultimate strength of a material is the maximum stress developed before the material will begin to rupture. The relationship of stress to strain in the elastic region of a material is defined by Hooke's law.

Hooke's law of elasticity was first discovered by the seventeenth century British physicist, Robert Hooke, who found that the extension of a spring was in direct proportion to the load applied to it – in other words, strain is directly proportional to stress. This is shown by the formula

$$F = -kx \ (N) \tag{2.5}$$

Where:
k = the rate or spring constant (N/m)
x = displacement of the spring's end from equilibrium position (m)
F = restoring force exerted on that end by the spring (N)

Although his law was established only for the case of springs, it has since been applied to all materials that regain their original shape after a force-induced deformation. Given the load (force) applied does not exceed their elastic limit, such materials are known as linear-elastic materials. The displacement response of any elastic material is considered

as similar to that of a linear spring, where a change in length (strain) in the direction of an applied axial stress (force) can be found as follows

$$\Delta\ell = \frac{F\ell}{EA} = \frac{\sigma\ell}{E} \text{ (m)} \tag{2.6}$$

Where:

$\Delta\ell$ = change in length in axial direction (m)

ℓ = original length in axial direction (m)

2.2 Properties of core materials (AK Steel Corporation, 2007)

Cores, such as the stators of EMs, require magnetic materials in a wide variety of properties and characteristics. The most commonly used soft magnetic material is an iron-silicon alloy known as silicon steel or electrical steel. The term 'electrical' refers to the steel's application rather than the method used in its production process. The electrical and magnetic characteristics of these steels are well suited to the requirements of laminated cores where flux polarity reversals and high frequencies are experienced.

Laminations refer to thin sheets of silicon steel which are cut out in the shape of the required core and stacked together until the full stack-length of the core is reached. It is done to restrict eddy currents to individual laminations so as to minimise core loss. Core loss refers to the electrical power dissipated within the core in the form of heat when the core is subjected to an alternating magnetic field, and is generally the most important criterion specified in the grading/selection process. These laminations also need to be insulated from one another, which is done by applying a type of surface insulation on the raw material. Options include oxide coating, enamel coating, and inorganic coating.

Silicon is used as the primary alloying element, as it increases the steel's volume resistivity, thereby reducing the eddy current losses. In addition, silicon also affects the steel's grain structure, which reduces the hysteresis loss in non-oriented electrical steels. Non-oriented refers to silicon steels with isotropic magnetic properties, i.e. the same in

any direction. Oriented refers to silicon steels with anisotropic magnetic properties, i.e. strongly oriented with respect to the rolling direction during processing. Trace elements of aluminium and manganese may also be added to silicon steel – depending on the type of product – but usually remain between 0.1 and 0.5%, added mainly for metallurgical effect. Silicon steels are divided into several classes and further into several grades within each class, according to industry requirements.

2.3 The magnetic field in electrical machines (Vaske, 1976)

In order to ensure the desired actions in EMs, their magnetic fields need special attention. For this reason, the differences between dc and ac excitation and their effects on electromagnets will be pointed out in the following section.

2.3.1 Excitation of the magnetic field

Every current I is inherently linked with a magnetic field. The associated magnetic flux Φ is determined by the number of turns N, the magnetomotive force (MMF) F = IN and the magnetic permeance Λ according to $\Phi = \Lambda F$. If the magnetic circuit consists mainly of non-saturated iron, and the air gap surface A_g of length δ is completely penetrated by the magnetic flux, the magnetic resistance (reluctance) of the iron can be neglected against the latter so that the magnetic permeance is then calculated from $\Lambda = \frac{\mu_0 A_g}{\delta}$.

Where:

μ_0 = the magnetic permeability of free space ($4\pi \times 10^{-7}$ Vs/Am)

2.3.1.1 DC excitation

If the exciting coil of a magnetic circuit with resistance R is connected to a dc voltage V the current is given by Ohm's law as $I = \frac{V}{R}$ and the magnetic flux by

$$\Phi = \Lambda F = \frac{IN\mu_0 A_g}{\delta} = \frac{N\mu_0 A_g}{R} \cdot \frac{V}{\delta}. \qquad (2.7)$$

The magnetic flux Φ can therefore be influenced by the dc voltage V and the air gap length δ, the former being the source of magnetising force and the latter representing the majority of reluctance in the magnetic circuit. The flux is also dependant on the dimensions of both the magnetic circuit and the excitation coil.

2.3.1.2 AC excitation

If the coil of an electromagnet is connected to a sinusoidal ac voltage V, besides its resistance R it will also exhibit a frequency dependant inductive reactance $X_l = \omega L$. The magnetic flux is then given by

$$\Phi = \frac{V}{4.44fN} \tag{2.8}$$

With ac excitation the induced flux is therefore given by the applied voltage V, the pertaining frequency f and the number of turns N. However, it is independent of the air gap length δ and magnetic circuit dimensions. Since Hopkinson's Law (Ohm's law of the magnetic circuit) $\Phi = \Lambda F$ still holds true, the magnetic flux can also, under consideration of the peak current value $i_p = \sqrt{2}I$, be expressed as

$$\Phi = \frac{\sqrt{2}IN\mu_0 A_g}{\delta} = \frac{V}{4.44fN}$$ so that the current I is given as

$$I = \frac{V\delta}{\sqrt{2} \cdot 4.44\mu_0 N^2 f A_g} = \frac{V}{\omega L}$$ with the inductance L given as

$$L = \frac{N^2 \mu_0 A_g}{\delta}. \tag{2.9}$$

While the excitation current I is independent of the dimensions of the magnetic circuit, it depends largely on the reluctance $\Re$ when the excitation is done via alternating current. Table 2.1 shows a comparison of both excitation procedures.

Table 2.1 Comparison of excitation procedures

EXCITATION WITH	DIRECT CURRENT	ALTERNATING CURRENT
Φ , B	$\propto V$, $\frac{1}{\Re}$, $\frac{1}{\delta}$	$\propto V$, $\frac{1}{f}$
I	$\propto V$	$\propto V$, $\Re$, δ

2.3.1.3 Electromagnet

The difference between these excitations can be seen distinctly by considering an electromagnet. With the air gap cross-sectional area A_g, air gap flux density B_g, and permeability of air μ_0, the attraction force in the air gap by dc excitation is according to

$$F = \frac{A_g B_g^2}{2\mu_0} \tag{2.10}$$

so that with (2.9) the induction B_g in the air gap of a dc excited magnet becomes

$$B_g = \frac{\Phi}{A_g} = \frac{IN\mu_0}{\delta} = \frac{\mu_0 N}{R} \cdot \frac{V}{\delta}. \tag{2.11}$$

Voltage V and air gap length δ can therefore be changed allowing the attraction force to be written as $F \propto \left(\frac{V}{\delta}\right)^2$. The resulting dc force characteristic is shown in Figure 2.2.

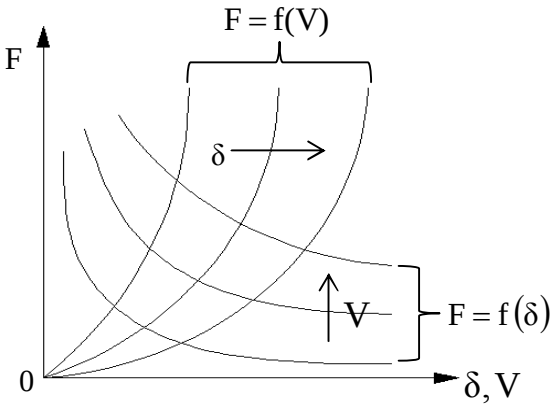

Fig 2.2 DC characteristic (Vaske, 1976)

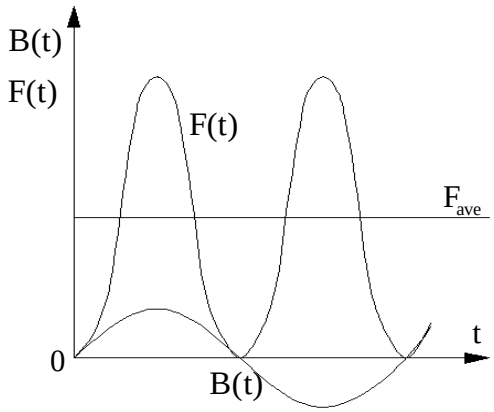

Fig 2.3 AC characteristic (Vaske, 1976)

For ac excitation the induction $B_g \propto i$ changes sinusoidally as $B_{gt} = B_g \sin(\omega t)$ in time. The force now oscillates at double the induction frequency between zero and a maximum. The average value F_{ave} of this ac force is, however, the same as the constant dc attracting force, if the rms value of the ac current equals the dc current, which can therefore be written as $F_{ave} \propto V^2$. This ac force characteristic is shown in Figure 2.3.

2.4 Electromagnetic forces in electrical machines

Force can be generally categorised as being either global force or local forces, meaning either total, or distributed forces, respectively. According to the International Electrotechnical Commission (IEC 60027-1 1992) distributed forces are defined as "mechanical actions on differential volumes or surfaces, as in body forces, surface forces or inertia forces". According to the same standard, total force is defined as "the integral over the volume or the surface of distributed forces". From a dimensional point of view, surface or traction force describes force per unit area, whereas force density describes force per unit volume.

The different types of force density in EMs are well represented by the following mathematical formula (Melkebeek, 2001) derived from the virtual work principle:

$$\vec{f}_{vw} = \vec{J} \times \vec{B} - \frac{1}{2}\vec{H}^2 \nabla \mu + \nabla\left(\frac{1}{2}\vec{H}^2 \frac{\partial \mu}{\partial \rho}\rho\right) \tag{2.12}$$

Where:

$\vec{f}_{vw}$ = force density (N/m^3)

$\vec{J}$ = current density (A/m^2)

$\vec{B}$ = magnetic flux density (Vs/m^2)

$\vec{H}$ = magnetic field intensity (A/m)

∇ = gradient function

μ = magnetic permeability (Vs/Am)

ρ = mass density (kg/m^3)

The first term of the equation $(\vec{J} \times \vec{B})$ indicates a force density experienced by current-carrying conductors in a magnetic field, also known as Lorentz Force. This then describes forces on the stator windings of all EMs and on the rotor bars/windings found in IMs.

The second term of the equation $(\frac{1}{2}\vec{H}^2 \nabla \mu)$ indicates a force density experienced by a magnetic body comprising different permeabilities when subject to an applied magnetic field. The force vector acts down a permeability gradient, that is, from regions of higher permeability to regions of lower permeability. This then describes surface forces acting at material boundaries, where a sudden change in permeability is experienced, and volume forces acting inside nonlinear magnetic materials with varying regions of permeability that change relative to external magnetisation. This type of force density is greatest at the iron-air boundaries in EMs, making a significant contribution to stator teeth deformation, while also being the torque-producing force in the rotors of reluctance machines.

The third term of the equation $\{\nabla\left(\frac{1}{2}\vec{H}^2 \frac{\partial \mu}{\partial \rho}\rho\right)\}$ indicates a force density linked to a change in both external magnetisation and the relationship between the permeability and mass density of the magnetic material. Here the force vector acts down a gradient governed by the strength and direction of magnetisation, and also the internal mechanical strain of the material linked to changes in permeability. This then is able to describe dimensional changes of the internal structure of all magnetic materials with a given mass when subjected to an externally applied magnetic field, also known as magnetostriction.

According to the literature, the forces acting in EMs are often divided up into two parts, although this is not necessarily scientifically correct. These are the long-range 'Maxwell' or 'reluctance' forces – consisting primarily of surface force, and the short-range 'magnetostriction' forces – consisting primarily of volume force. In fact, these forces always occur together in nature, and are separated from each other only in theory to aid in their calculation. It has been stated (Melkebeek, 2002) that the forces exerted on a magnetised body consist of internal surface stress, external surface forces at material

boundaries, internal long-range and short-range volume forces, and external long-range volume forces (e.g. gravity). As already mentioned, all the known force formulations are in agreement as to the calculation of global force but differ quite dramatically when it comes to the force distribution. Coupled with this uncertainty, exists some ambiguity when reading the literature, with respect to the exact meaning of the various forces and where exactly they each fit into the picture. A brief explanation of the relevant forces in this work will therefore be attempted in the following sections.

2.4.1 Maxwell forces (Wignall, 1988) (Zhu, 2006) (Heyns, 2011)

These forces are called 'long-range' forces as they result from 'forced' magnetisation coming from an external source, and 'reluctance' forces as they act in regions of changing permeabilities, which, in effect, causes magnetic reluctance changes. Although these forces are mainly found at material boundaries (surfaces) where permeability change is the greatest, the long-range force distribution also has a volume component, related to permeability change. The stresses proposed by Maxwell have the properties of both a longitudinal stress which acts along flux lines as well as a transverse pressure. The MST method is the most common way of calculating these forces, where, according to Maxwell, by forming a closed surface around a group of field sources and integrating the stresses along this closed surface, the total force on them can be found.

The 2D FE software used in this thesis (Alstom SLIM v3.14) utilises the MST method to calculate the stresses and forces for the electromagnetically simulated model of the force rig(s). It does this by first obtaining the flux density $\vec{B}$ along a path through the centre of the air gap, where $\vec{B} = \vec{\nabla} \times \vec{A}$ (the curl of the magnetic vector potential). The normal and tangential components of the flux density, B_n and B_t, are then used to find the normal and tangential components of the stress, σ_n and σ_t, shown by equations

$$\sigma_n = \frac{B_n^2 - B_t^2}{2\mu_0} \tag{2.13}$$

$$\sigma_t = \frac{B_n B_t}{\mu_0} \tag{2.14}$$

The normal and tangential force components F_n and F_t are then calculated along a closed contour integral Γ which traverses the circumference of the machine along the air gap centre, and multiplied by the stack length ℓ_s of the rotor, shown by equations

$$F_t = \frac{\ell_s}{\mu_0} \oint B_n B_t d\Gamma \tag{2.15}$$

$$F_n = \frac{\ell_s}{2\mu_0} \int_0^{2\pi} (B_n^2 - B_t^2) d\Gamma \tag{2.16}$$

2.4.2 Magnetostriction forces (Cameron, 1989) (Melkebeek, 2002) (Belahcen, 2004)

Magnetostriction may refer to any deformation of a material due to magnetic interactions. These interactions take the form of magnetic forces exerted on the material (long-range) by an external magnetic source as well as interatomic interactions (short-range) leading to internal structure changes as a result of magnetisation or applied mechanical stress. More strictly speaking only the latter is regarded as magnetostriction. Magnetostrictive forces tend to try and compress a magnetic material to increase its effective permeability.

There are several magnetostrictive effects. There is a 'spontaneous' magnetostriction that occurs without an externally applied magnetic field, called the volume effect. A good example of this is the isotropic expansion in iron around its Curie temperature when it is cooled from a higher temperature. This is a relatively weak effect.

The Joule effect causes an anisotropic expansion or contraction of a material in the direction of an applied magnetic field, falling under the category 'forced' magnetostriction. Associated with this type is a 'transverse' magnetostriction acting in a perpendicular direction to the applied field, called the Wiedemann effect. These two effects have a nonlinear characteristic, reaching 'saturation' when the material saturates. The volume of the material is not changed unless higher levels of magnetisation are applied – here these two effects are accompanied by the isotropic component of the forced magnetostriction, which introduces a small change in volume to the material.

The Villari effect is the inverse of the Joule and Wiedemann effect where the magnetic properties (permeability) of a magnetic material change in response to an applied mechanical stress, also known as a 'magnetomechanical' effect.

2.4.3 Radial and peripheral forces

Forces in EMs act on the stator teeth mainly in two directions – namely, radially and peripherally, both resulting in displacement. Radial forces act along the radial axes that point outwards from the centre of the machine, while peripheral forces act in a perpendicular direction to these axes (circumferential). This principle is adapted to the simple iron core shown in Figure 2.4, which may be regarded as the 'magnetic circuit prototype'. A significant portion of these forces in EMs are considered to be Maxwell forces as the flux crosses the air gap and encounters sudden permeability changes at the iron-air boundaries. The result of these forces in EMs is distortion of the stator yoke, resulting in frequency dependant 'mode shapes' of the stator, being the principal cause of vibration and noise in low to medium power rated machines. These forces act as follows:

1) Radial forces pull the teeth into the air gap
2) Peripheral forces pull or 'rock' the teeth sideways

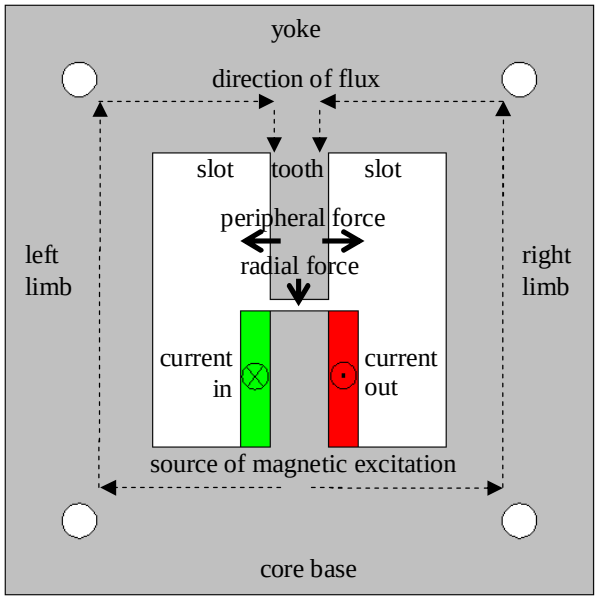

Fig. 2.4 Radial and peripheral forces acting on an iron tooth

2.4.3.1 Radial forces

These forces acting on the stator are of primary significance as the result is unwanted vibration and noise emitted to the external environment; any radial deformation of the rotor is generally regarded as negligible. These forces are found mainly at the tips of the stator teeth, where the flux traverses the iron-air boundary to cross the air gap. This induces Maxwell stresses at these boundaries which have the effect of a tension being experienced by the region of higher permeability and a pressure being experienced by the region of lower permeability. The resulting force acts in the direction from high permeability to low permeability, and hence the force is induced from the iron into the air gap, as shown in Figure 2.4. This ultimately results in displacement of the stator teeth into the air gap, which contributes towards the distortion of the stator core back (yoke). The radial forces in EMs are generally larger than the peripheral forces and are the more dominant source of vibration, while making no contribution whatsoever to the desired output of the machine.

2.4.3.2 Peripheral forces

These forces acting on the rotor are of primary significance as they are the torque-producing forces, essential to the operation of the machine. They do, however, also contribute towards displacement of the stator teeth. They act in a ‘sideways’ direction to a tooth, down the permeability gradient, from tooth into slot, as shown in Figure 2.4. This sideways ‘rocking’ action results in the stator core distorting at the root of the teeth, which also contributes towards vibration. These forces are important for three reasons. Firstly, the tooth can be quite flexible in the peripheral direction, which is in contrast to the radial forces that are attempting to distort a much stronger arch shape. Secondly, a peripheral force on the tooth can cause the core back to distort in a sinusoidal shape, and the core back can be quite flexible in this mode, especially if it is thin in a radial direction, common with high pole number motors. And thirdly, the vibrating action caused by peripheral forces may also cause insulation damage to the stator conductors.

Chapter 3

Force rig design and strain measurement

It has been stated that forces and stresses in materials are not directly measureable; rather they are calculated from the measurement of their associated phenomena. Exploring coils embedded in the stator teeth of EMs have been used (Dye, 1972) (Balan, 1993) (Balan, 1994) (Balan, 1998) which measure changes in induced voltage as the rotor moves. Vibration sensors placed on the external housing of rotating EMs have also been used (Rodriguez, 2007) (Husain, 2010) (Torregrossa, 2011) to measure the vibrational behaviour transmitted from the stator.

In this thesis, measurements of strain on a tooth will be attempted when known forces are applied to it. It appears that measurement of stator teeth displacements in an EM during operation is an extremely difficult task. It has therefore been decided to build a 'force rig', constructed of silicon steel laminations, where a stator tooth, rotor iron and air gap arrangement is emulated. The tooth will be subject to magnetic forces when flux provided by a dc coil crosses the air gap, and the silicon steel core will complete the magnetic circuit. The average normal flux density in the air gap will reach a maximum of around 1T, being a relative average value in the air gaps of EMs.

This thesis is concerned only with the measurement of radial (or normal) tooth displacement. For the purpose of simplifying the terminology from this point forward, this displacement will be referred to as y-displacement, and the associated forces as y-forces, according to the Cartesian coordinate system. For practical reasons, any peripheral (or tangential) displacement and associated forces will be regarded as negligible. As above, this displacement will be referred to as x-displacement, and associated forces as x-forces, from this point forward.

Before designing the rig, it is necessary to investigate what measuring technology will be used, in order that it may be incorporated in the design. Therefore, the first step is to get an idea about what magnitude of strain can be expected, so as to know what measuring

range is required from the measurement system. In order to achieve this, the magnetic circuit prototype shown in Figure 2.4 is modelled, having the above mentioned design criteria, by using 2D FE software. The core is modelled as M-19 silicon steel – being the most commonly used core material in EMs – and an average normal flux density of 1T is created in the air gap, having a 2mm length, by means of exciting the coil, having 100 turns, with 17A dc.

As shown in the flux plot in Figure 3.1, the current enters the page through the left side of the coil and returns through the right side, thereby causing the flux to flow from the south pole (SP) of the coil through the magnetic circuit and return to the north pole (NP) via the tooth and air gap. As explained in Section 2.4.3.1, y-forces are induced from iron into air, down the permeability gradient, tending to elongate the tooth into the air gap.

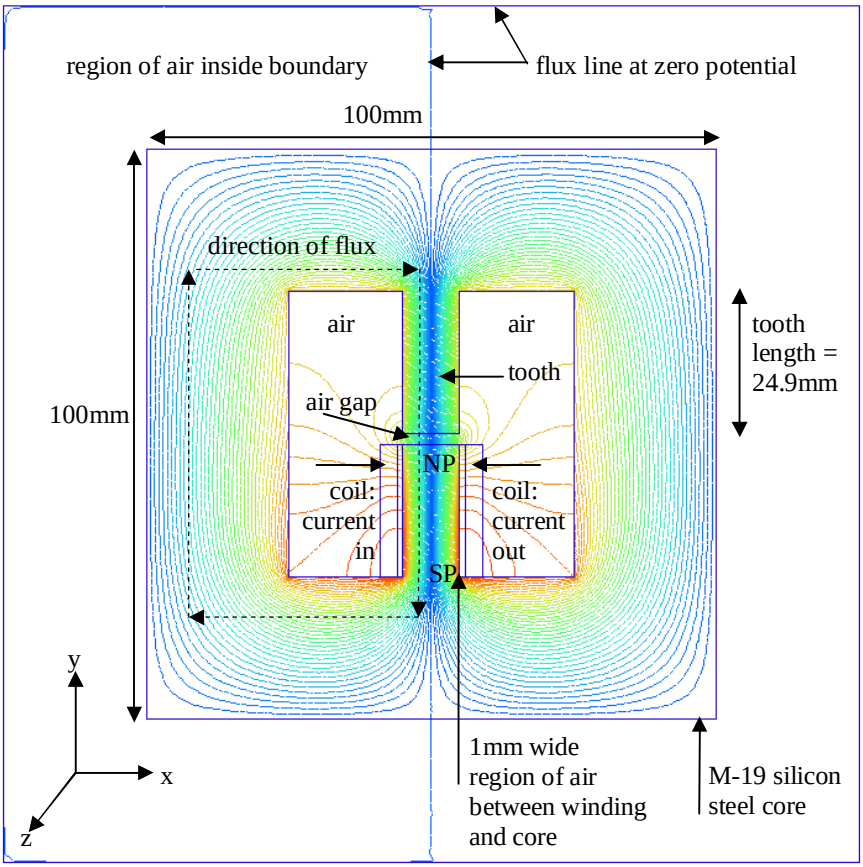

Fig. 3.1 Flux plot for prototype magnetic circuit

The average normal flux density in the air gap is found by defining a path through its centre, as shown in Figure 3.2. The FE software then calculates the values of flux density normal to this paths surface. The discretisation of the mesh in and around the air gap is considered sufficient at this stage.

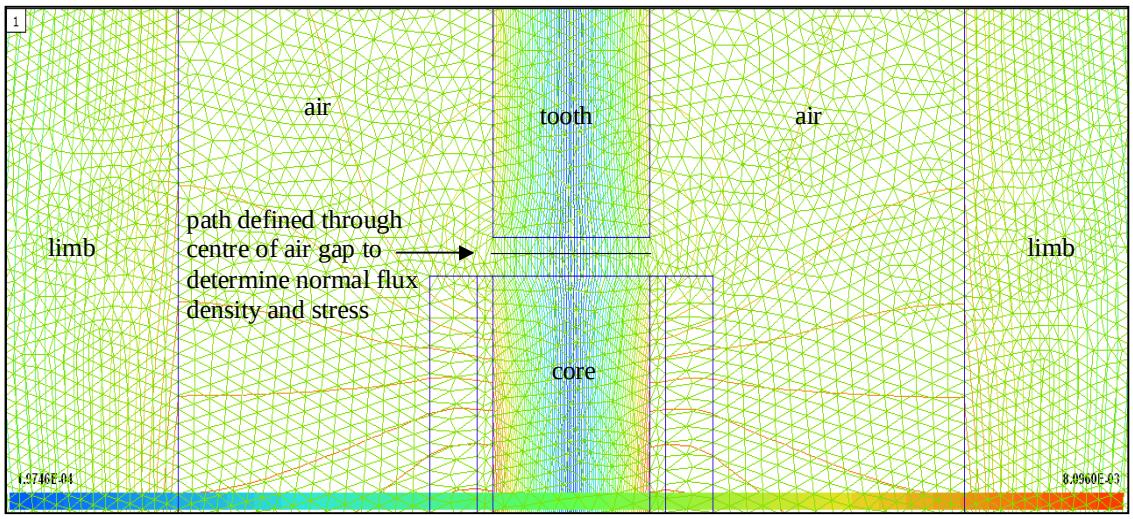

Fig. 3.2 Path defined through the elements for determination of flux density and stress

The flux density graph normal to the defined path is shown in Figure 3.3.

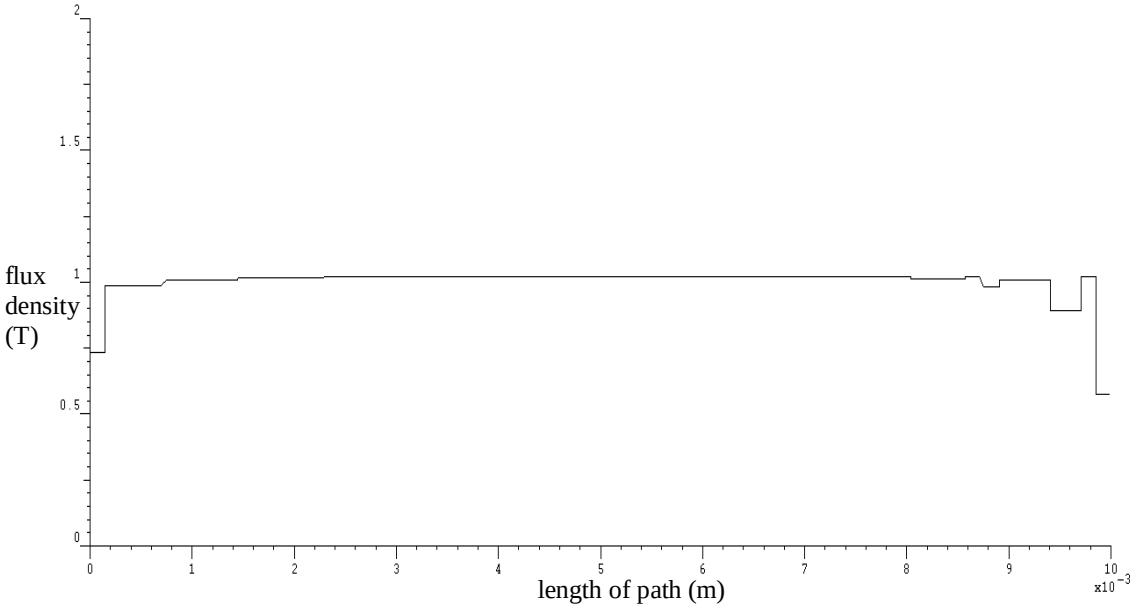

Fig. 3.3 Graph of flux density normal to the path defined through the air gap

According to Hooke's law, it is possible to calculate the y-strain (change in length) of the tooth once the y-stress acting on it is known. The stress in the centre of the air gap is considered sufficient for this exercise, and therefore the same path can be used as in Figure 3.2, where the FE software calculates the stress normal to this path (y-stress). The result is shown in the graph in Figure 3.4, with the average normal stress of 400157Pa calculated by the FE software, shown by the red line. The fact that the stress is shown in the negative y-region of the graph is purely an indication of the way in which the path is defined (left to right) and does not indicate direction (downwards) of the stress. The dips on the left and right hand sides indicate the flux leakage on either side of the tooth.

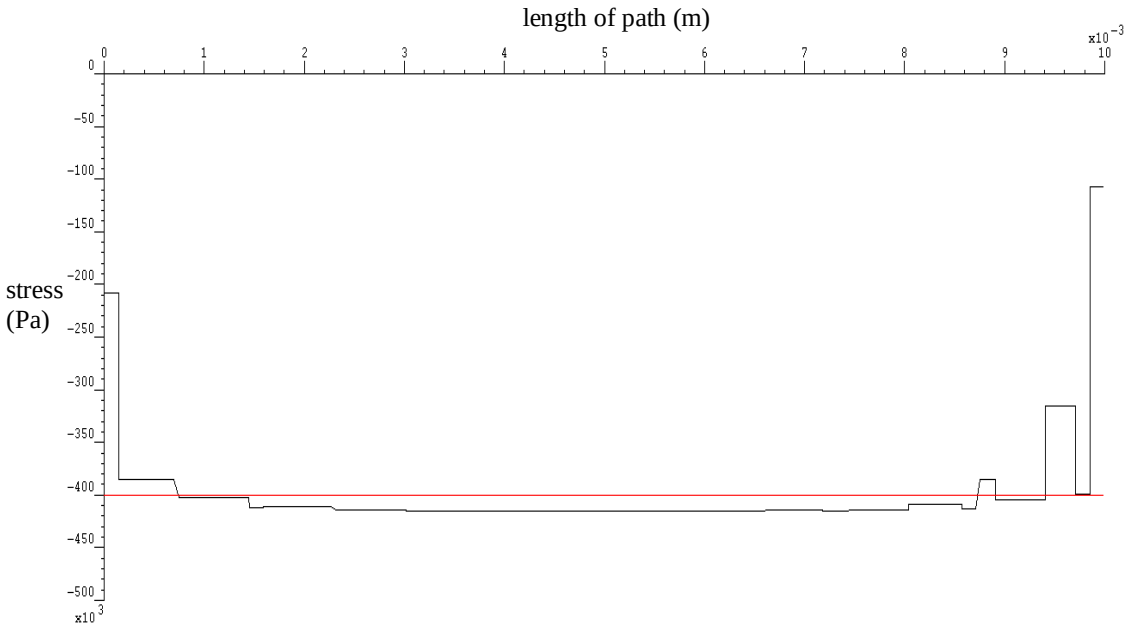

Fig. 3.4 Graph of stress normal to the path defined through the centre of the air gap

Now it is possible to calculate the elastic y-strain of the tooth by using Hooke's Law for deformable materials, according to (2.6), as the stress, original length of the tooth, and the Young's modulus of M-19 silicon steel are all known [refer to Appendix A, where the Young's modulus in the rolling direction (RD) is assumed]. This is calculated according to

$$\Delta\ell = \frac{F\ell}{EA} = \frac{\sigma\ell}{E} = \frac{400157 \times 0.0249}{185 \times 10^9} = 53.86 \times 10^{-9}\,\text{m}$$

Where:

$\Delta\ell$ = change in length (y-direction) of tooth (m)

ℓ = original length (y-direction) of tooth (m)

E = Young's modulus according to manufacturer's data (Pa)

σ = stress normal to the path defined through the air gap (Pa)

Therefore, a measurement technology that is capable of measuring strain in the nanometre range is required. The next step is to conduct an investigation into the possible measurement techniques that are available, and then to choose the appropriate one. Other important factors to take under consideration are the measuring device's susceptibility to magnetic fields and the cost of the measurement system.

3.1 Strain measurement investigation

There are many methods available for measuring strain, each having different measuring ranges and limitations. A brief overview of the types of strain measuring devices looked at for this thesis follows, and the most suitable method is chosen and discussed in more detail.

3.1.1 Electrical resistance strain gauge

Strain gauges operate on the principle where a strain, experienced by the test specimen, causes a change in electrical resistance of the gauge, which is fed through a bridge circuit and the resistance change appears at the output. Strain gauges in this category include the carbon-resistor gauge, the semiconductor (piezoresistive) gauge and the most commonly used of all strain gauges – the bonded metallic wire or metallic foil resistance gauge. The carbon-resistor gauge is the predecessor of the bonded metallic wire and foil gauges. It has high strain sensitivity, can have a short gauge length, is low in cost, but is highly sensitive to temperature and humidity. The semiconductor gauge has the highest strain sensitivity in this category, but exhibits a nonlinear relationship between strain and resistance, affecting its output and the bridge circuit, and has a substantial sensitivity to temperature. The bonded resistance strain gauge, shown in Figure 3.5, has a fairly high

sensitivity to strain, low temperature sensitivity, exhibits a linear relationship between strain and resistance, can have a short gauge length, small physical size and mass, and is low in cost. Important factors that need to be taken into account are the gauge factor, determination of and alignment with the principal axes of strain, transverse sensitivity, temperature effects, the type of bridge circuit to be used as well as shielding and guarding the measurement leads and measuring equipment against electromagnetic interference, mounted gauge resistance and isolation of the gauge from the target specimen. The minimum strain that can be measured with any accuracy by these gauges is in the micrometre range and the measurement systems of these gauges are all highly sensitive to electromagnetic interference. These two factors make electrical resistance strain gauges a practically unsuitable option for this thesis. (Agilent Technologies, 1999)

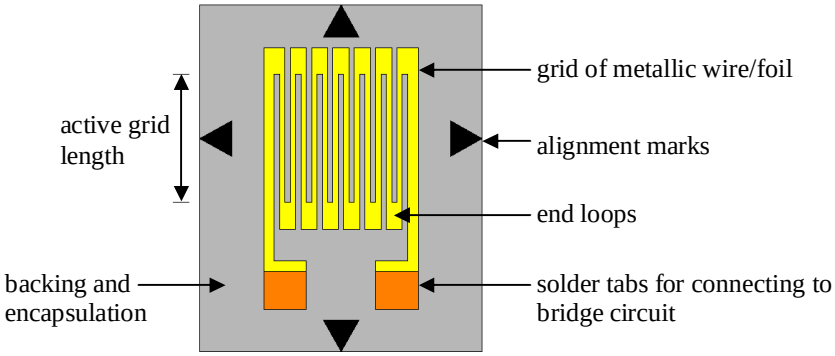

Fig. 3.5 Bonded resistance strain gauge, as redrawn from (Kuphaldt, 2000)

3.1.2 Optical strain gauge using fibre Bragg grating

Fibre-optic sensing overcomes the challenges of transmission loss and electromagnetic interference experienced by nearly all electrical displacement sensors, by using light and optical fibre instead of electricity and copper wire. The fibre Bragg grating (FBG) is one of the most commonly used optical sensors and is able to sense any strain experienced by the fibre-optic cable in which it is incorporated. The Bragg grating, shown in Figure 3.6, is formed by permanently altering the refractive index of a length of photosensitive fibre due to exposure to a periodic distribution of intense light. Light is propagated through the optic fibre and will pass through the Bragg grating which will reflect a very narrow range of wavelengths, the remainder being transmitted to the interrogator through the grating.

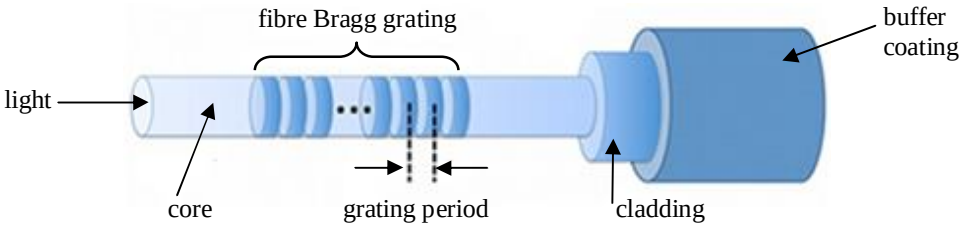

Fig. 3.6 Fibre-optic cable with fibre Bragg grating (National Instruments, 2011)

Any strain or change in temperature experienced by the optic fibre will affect the refractive index and grating period, resulting in a shift of reflected light wavelength from the FBG. For accurate strain measurements, temperature effects need to be compensated by installing a FBG temperature sensor in close proximity to the FBG strain sensor and subtracting the wavelength shift due to temperature from the wavelength shift due to strain. FBG strain sensors are able to measure strains in the nanometre range, and are relatively inexpensive. The interrogators used to process their data, however, are extremely expensive. (National Instruments, 2011)

3.1.3 Confocal displacement sensor

These sensors focus polychromatic white light (light which contains all the colours of the spectrum, each of which having a different wavelength) through a multi-lens optical system onto the measurement target's surface. The white light is dispersed by a specific lens arrangement into monochromatic light and, by factory calibration, each wavelength is assigned a specific distance to the target. The wavelength used for the measurement is only that which is exactly focused on the measurement target. The measuring principle is illustrated in Figure 3.7. Shadowing is avoided by the one axis arrangement of the emitter and receiver. These sensors are non-contact, achieve nanometre resolution, are able to measure deflections on very small targets due to the very small spot size, and are able to measure in small gaps and narrow apertures due to small sensor design. However, the beam requires a clean environment, there is a limited distance between sensor and target, and the high cost puts this sensor outside the financial scope of this thesis.
(Allcock, 2011) (Micro-Epsilon, 2012)

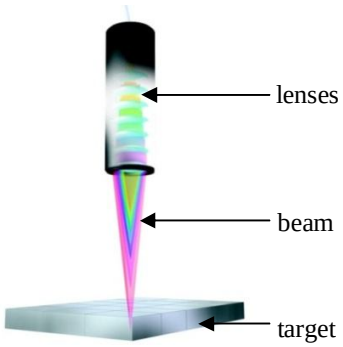

Fig. 3.7 Confocal displacement sensor (Micro-Epsilon, 2012)

3.1.4 Laser triangulation displacement sensor

Laser triangulation sensors use a laser diode to project a visible light spot onto the measurement target. The light reflected from this point is projected through a high quality optical lens system onto a charge coupled device (CCD) array, which transduces photons to electrons, and any change in position of the target with respect to the sensor is analysed to determine the exact displacement of the target. The measuring principle is illustrated in Figure 3.8.

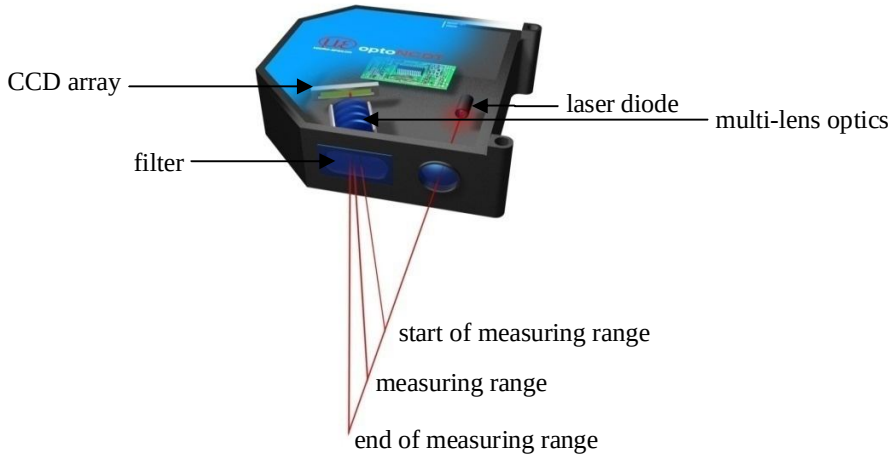

Fig. 3.8 Laser triangulation displacement sensor (Micro-Epsilon, 2012)

As the sensor has no physical contact with the target it is not subject to wear, transmission loss or electromagnetic interference and mounting limitations are avoided. The small light spot enables measurements on very small parts, and measurements can be

taken at large distances enabling difficult target surfaces to be measured, e.g. hot metals. These sensors are non-contact and able to measure in the nanometre range with high accuracy and resolution, but are relatively large, require a clean optical path for reliable operation, special calibration for specific targets and are also very expensive.
(Allcock, 2011) (Micro-Epsilon, 2012)

3.1.5 Eddy current displacement sensor

This sensor employs an inductive measuring principle. It consists of a coil excited with ac producing a magnetic field around it. Eddy currents will be induced in any electrically conducting object placed in this field and, according to Faraday's induction law, these will form an electromagnetic field opposing the field of the coil, causing a change in impedance of the coil. The sensor controller then calculates any change in energy between the coil and the measurement target and converts this quantity into a displacement. The measuring principle is shown in Figure 3.9. The advantage this sensor offers over other inductive displacement sensors is its small size, temperature withstand capabilities and extremely high nanometre resolution. It is also non-contact, highly accurate, immune to dust, dirt, humidity, high pressures, oil and any dielectric material in the measuring gap. However, its output and linearity are dependent on the electric and magnetic characteristics of the target and, for each specific measurement case, individual linearisation and calibration is required. Mainly due to the inevitable electromagnetic interference that would occur due to the nature of the proposed experiment, this option was rendered as unsuitable for this thesis. (Allcock, 2011) (Micro-Epsilon, 2012)

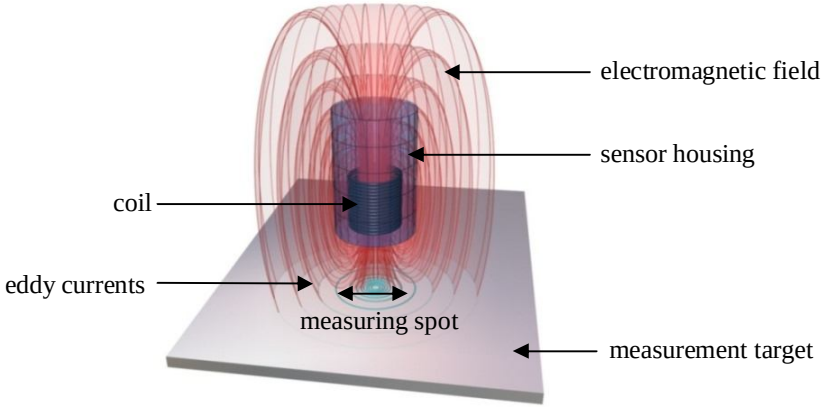

Fig. 3.9 Eddy current displacement sensor (Micro-Epsilon, 2012)

3.1.6 Capacitive displacement sensor

The principle of capacitive displacement measurement is based on the operation of an ideal plate-type capacitor, where the sensor and target form the two plate electrodes. If the sensor capacitor is excited by an alternating current with constant frequency, the alternating voltage amplitude on the sensor is directly proportional to the distance between the electrodes of the capacitor. The amplifier electronics then generate an adjustable compensating voltage and, after demodulation of both voltages, the difference is amplified and an analogue signal appears at the output. The measuring principle is shown in Figure 3.10. As the sensor's construction is that of a guard ring capacitor, it achieves almost ideal resolution and linearity against metal targets. It is also non-contact, has high temperature stability and can measure in the nanometre range with very high accuracy. At the same time, being one of the most precise methods available for non-contact displacement measurement, it is also relatively low in cost. This measuring principle operates best in clean, dry applications, and the cable length between sensor and controller must be short as cable capacitance affects the oscillating circuit tuning. The Micro-Epsilon capaNCDT (capacitive Non-Contact Displacement Transducer) range offers sensors that are able to operate reliably in a magnetic field alternating at 50Hz or less, require only a small target diameter (as low as 3mm) and provide extremely high nanometre resolution. (Allcock, 2011) (Micro-Epsilon, 2012)

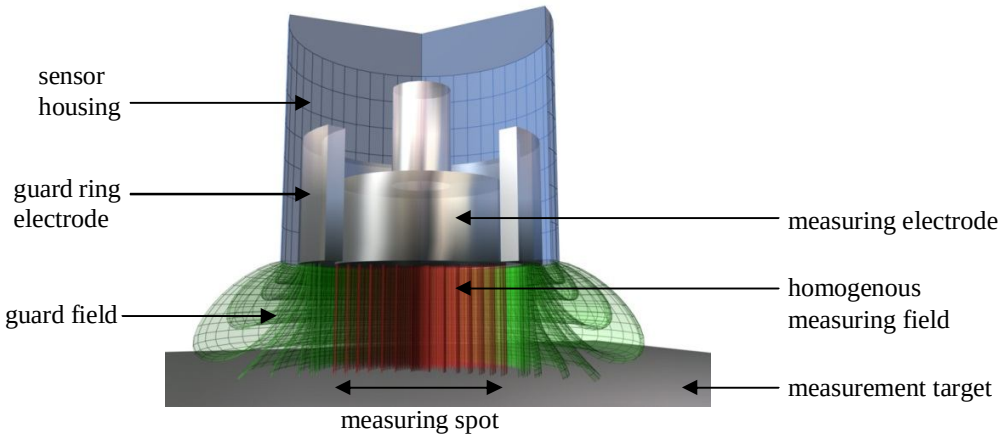

Fig. 3.10 Capacitive displacement sensor (Micro-Epsilon, 2012)

For all the reasons mentioned above it has been decided that the capacitive measuring technique is the most appropriate choice for this thesis. This measuring technology offers a range of different sensors and controllers suited for various applications. The sensor and controller chosen for this application are the CS02 and DT6300 respectively; these are discussed in more detail in the next chapter. It is shown in Section 4.1.1.4 how this measurement system achieves a resolution, under static conditions, of 2 nanometres. In order for this signal to appear at the output, the controller requires a built-in preamplifier to boost the input signal before it is processed through the signal conditioning electronics. A block diagram of the chosen measurement system is shown in Figure 3.11.

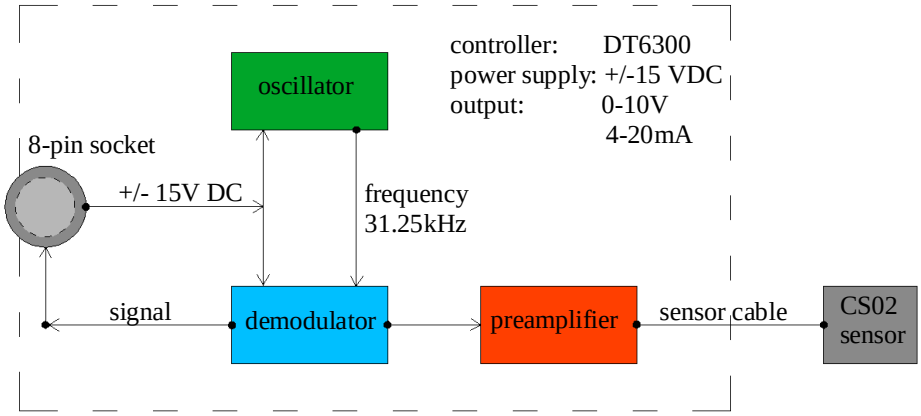

Fig 3.11 Block diagram of capaNCDT measurement system

A photograph of the chosen measurement system is shown in Figure 3.12.

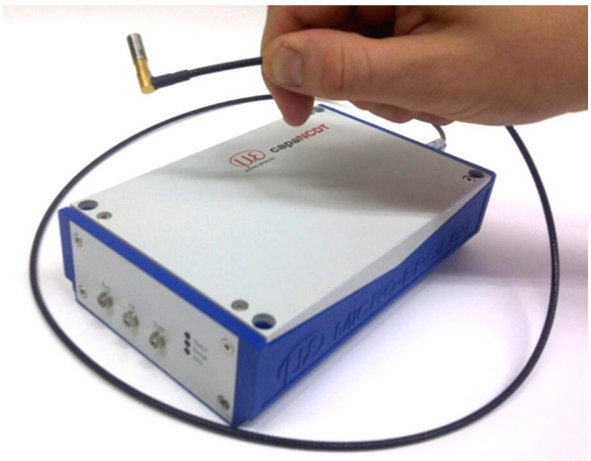

Fig. 3.12 CapaNCDT DT6300 controller with CS02 capacitive displacement sensor

3.2. Force rig design

3.2.1 Core material

Before the core is designed, it is of utmost importance that the material chosen for its construction has suitable magnetic properties. This material would ideally be the same as that used in the construction of EM stators and rotors, i.e. high grade silicon steel. As previously mentioned, the most common grade of silicon steel used in EM construction is M-19. After an extensive search, it was found that this particular grade of silicon steel was not available locally and therefore an alternative had to be found. The search criteria allowed only for higher grades of silicon steel – i.e. improved magnetic properties – so as not to compromise the magnetic characteristics of the rig. It was then found that grade M-15 was locally available in a thickness of 0.35mm, which perfectly suited the requirements of the study.

A comparison between M-15 and M-19 is shown in Table 3.1. Please refer to the stress-strain diagram in Figure 2.1 for an explanation of the properties mentioned. The universal codes for 0.35mm thick M-15 and M-19 silicon steel are M250-35A and M270-35A respectively, and will be used from this point forward.

Table 3.1 Properties of M250-35A and M270-35A (Cogent, 2011)

SILICON STEEL TYPE	M250-35A	M270-35A
YOUNG'S MODULUS (RD)	185×10^9 N/m^2	185×10^9 N/m^2
YOUNG'S MODULUS (TD)	200×10^9 N/m^2	200×10^9 N/m^2
YIELD STRENGTH	455×10^6 N/m^2	450×10^6 N/m^2
TENSILE STRENGTH	575×10^6 N/m^2	565×10^6 N/m^2
LOSS AT 1.5T, 50Hz	2.35 W/kg	2.47 W/kg
RELATIVE PERMEABILITY AT 1.5T	660	700

It can be seen that M250-35A has superior core loss properties, which is useful when ac excitation is used, but is not relevant to this study. Both steels have the same Young's modulus and almost identical yield and tensile strength values. The only disadvantage is that M250-35A will saturate at a slightly lower flux density. This is not considered a problem as the required air gap flux density is required to be no more than 1T.

3.2.2 B-H data for solving of the FE magnetic solution

In order for the FE software to correctly determine the magnetic solution of a given material, it requires data giving the material's flux density B response to applied magnetising force H up to and beyond the material's saturation point. As the M250-35A information supplied by the steel manufacturer (refer to Appendix B) only ranges from 0 – 1.8T, according to their measured Epstein Frame results, it is necessary to extrapolate further information to approximate the points on the B-H curve beyond 1.8T.

A number of mathematical methods are available and in use today. These are purely theoretical and have their drawbacks where accuracy is concerned. A new extrapolation procedure has been proposed by Umenei, *et al*. (2011), derived in conjunction with measured Epstein Frame data – namely, the Law of Approach to Saturation (LAS). It is a data extension algorithm that utilises the following set of equations:

$$M = M_s\left(1-\frac{b}{H^2}\right) \tag{3.1}$$

$$B = \mu_0(H + M_s - M_s\frac{b}{H^2}) \tag{3.2}$$

Where:

M_s = saturation magnetisation (A/m)

b = curve fitting coefficient

μ_0 = permeability of free space ($4\pi\times10^{-7}$) (Vs/Am)

By substituting the last data points from the measured B-H curve and solving the equations simultaneously, new B and H values are obtained. Then, by a process of re-substitution, B and H values are further extrapolated for field strengths beyond measurement range. The B-H curve shown in Figure 3.13 is derived solely from the manufacturer's data and is provided so that the curve approaching saturation may be more clearly seen. The B-H curve shown in Figure 3.14 is from the extrapolated data using LAS, up to 3T, supplied to the FE software for solving of the magnetic solution.

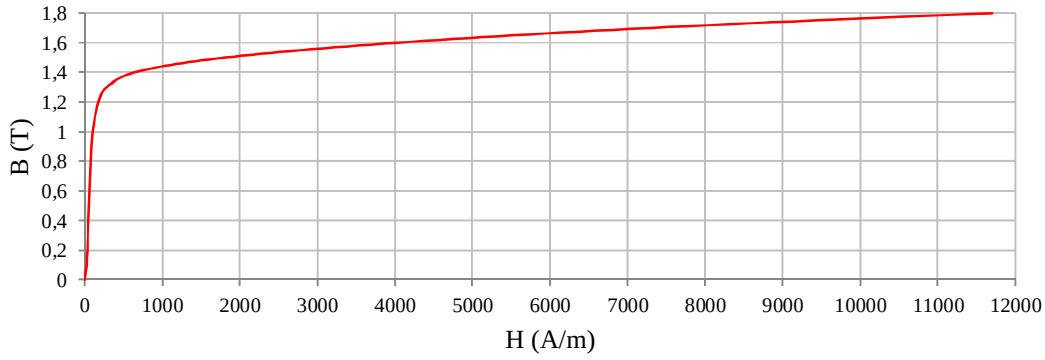

Fig. 3.13 B-H curve for M250-35A

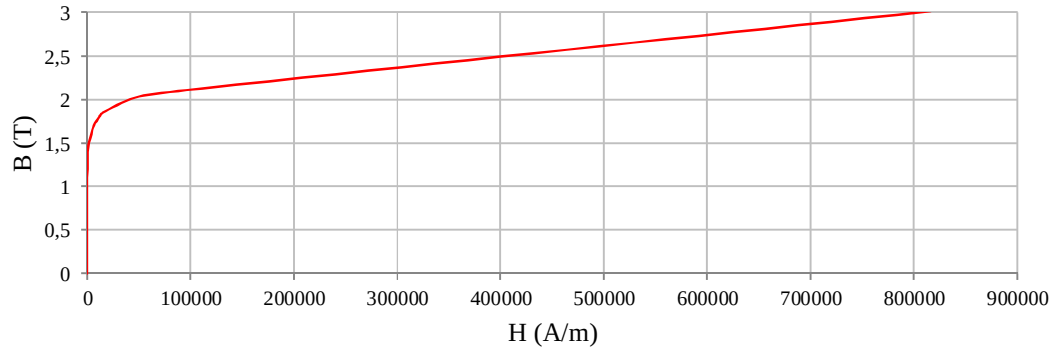

Fig. 3.14 B-H curve for M250-35A using LAS

3.2.3 Design 1

Now that the measuring technology, core material, and information required by the FE software are known, the design process can begin. Since the measuring device measures displacement by sensing the dimensional change in the dielectric (air) between two capacitive plates (the sensor and the measurement target), it follows that the sensor must face the tooth tip. This is because y-displacement of the tooth into the air gap is expected, which would reduce the dielectric between tooth tip and sensor. The tooth tip is therefore the measurement target and the required position of the sensor in the rig is now known.

A good place to start is the prototype magnetic circuit, as seen in Figure 3.1. In order for the sensor to be accommodated in a position facing the tooth tip, a section of the core underneath the tooth – which shall be called the 'lower middle limb' – would have to be removed, creating a cavity suitable for the sensor and sensor cable. A sensor cable with a

90° bend is chosen, enabling the sensor to be inserted into the cavity sideways, and the core base below the cavity may therefore remain closed. The sensor would then be clamped into position. The distance from the top of the sensor to the bottom of the 90^{o} bend is 25mm and the diameter of the sensor is 6mm, giving a slightly oversized cavity in the lower middle limb of dimensions 35mm high by 7mm wide. A major drawback of the sensor cavity is an uneven flux distribution in the air gap, but the required average flux density of 1T can still be achieved by varying the applied MMF to the circuit.

According to the position of the coil in the prototype model, the lower middle limb and tooth would be subjected to excessive heat dissipated by the conductors, and possibly also some movement when the coil is energised. As displacement due to heat-flexing of the tooth would cause measurement errors, the position of the coil must change, leaving either the left or the right limb. Heat-flexing of the limbs will also cause measurement errors, but is expected to be more manageable by comparison. As a balanced flux distribution is desired in the air gap it follows that both limbs should be wound. The same polarity for both excitation coils is required in order that the flux through the tooth is unidirectional. As shown in Figure 3.15, the current now enters the page through the right side of each coil and returns through the left side, resulting in an upwards flux direction.

To promote a homogenous flux distribution in the core, a design similar to that of a transformer E-piece is adopted, where the two limbs are each half the width of the tooth. The height of the yoke and core base are three times the width of the limbs for mechanical stiffness with an extra 20mm added to that of the core base to enable the core to slot into a wooden supporting base. As the volume of the lower middle limb has now been reduced to accommodate the sensor, its sides have been sloped, in an attempt to reduce the possibility of saturation in this region.

The air gap needs special attention as this represents the majority of reluctance in the magnetic circuit, and therefore needs to be kept to a minimum. As it is necessary to physically measure the flux density in the gap during experiments, the minimum gap length is 1.5mm, in order to accommodate the transverse Hall probe of the Gaussmeter. An illustration of force rig Design 1 with flux direction is shown in Figure 3.15.

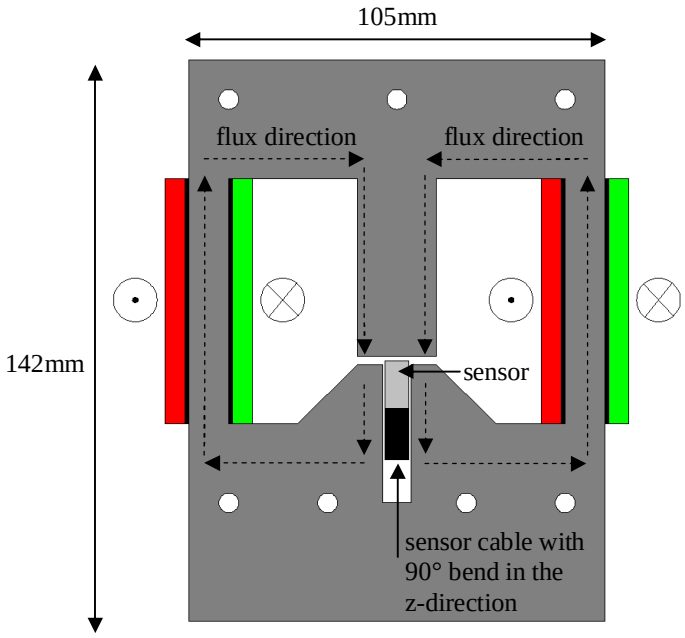

Fig. 3.15 Force rig Design 1 with flux path shown

According to the FE simulation, an average normal flux density of 1T is achieved in the air gap by exciting each coil of 200 turns with a dc current of 10.5A. The 2D flux plot for the simulation is shown in Figure 3.16, and the flux density normal to a path through the centre of the air gap is shown in Figure 3.17, with the average indicated by the red line.

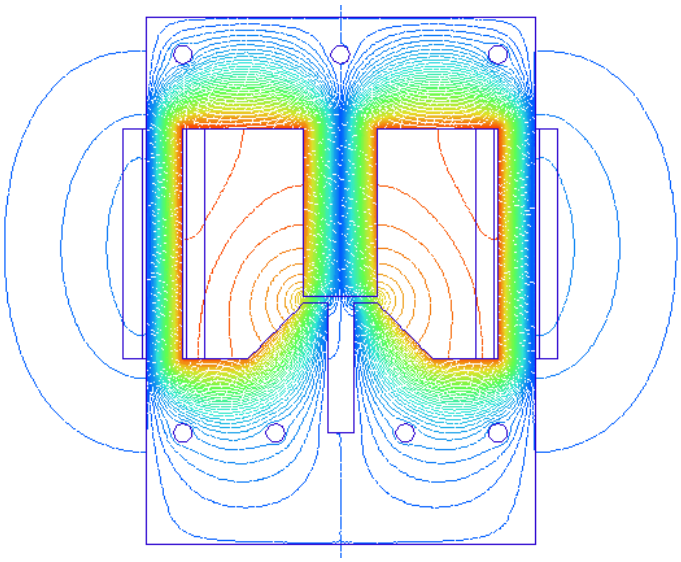

Fig. 3.16 2D flux plot for Design 1

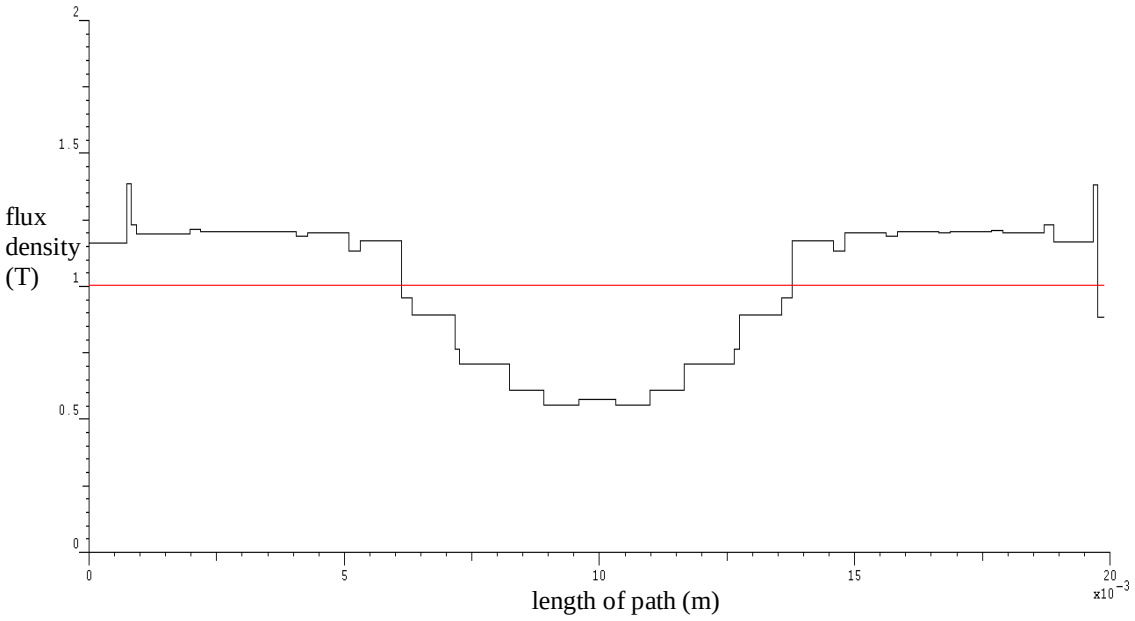

Fig. 3.17 Graph of flux density normal to the path defined through the air gap

It is commonly understood that 2D FE software assumes a depth (z-axis) of 1, that is, 1m. The FE mesh in this design has been specified with a scaling factor of 0.001 which means that the dimensions will change from metres to millimetres, and should affect the model in all directions. It therefore follows that a depth (z-axis) of 1mm is now assumed.

For the construction of the physical rig, a lamination stack length (z-axis) of 10mm is chosen to add mechanical strength while being relative to the FE model by a factor of 10. Nylon bolts and nuts are used to fasten the laminations together so as to interfere with the flux pattern in the core as little as possible. Enamel-coated solid-core copper conductor is used for the coils. This type of insulation allows for increased current-carrying capacity as it can withstand working temperatures up to 180°C (refer to Appendix C). A conductor size of 1mm^2 has been chosen, as it can comfortably carry the required 10.5A dc (refer to Appendix D) and is easy to work with when winding the limbs by hand. Both limbs and other parts of the core are wrapped in adhesive tape before winding the coils, in order to shield the enamel insulation of the conductors from the steel core during the winding process, and also to assist in keeping the laminations fastened together where necessary. A photograph of the magnetic circuit for the first design is shown in Figure 3.18.

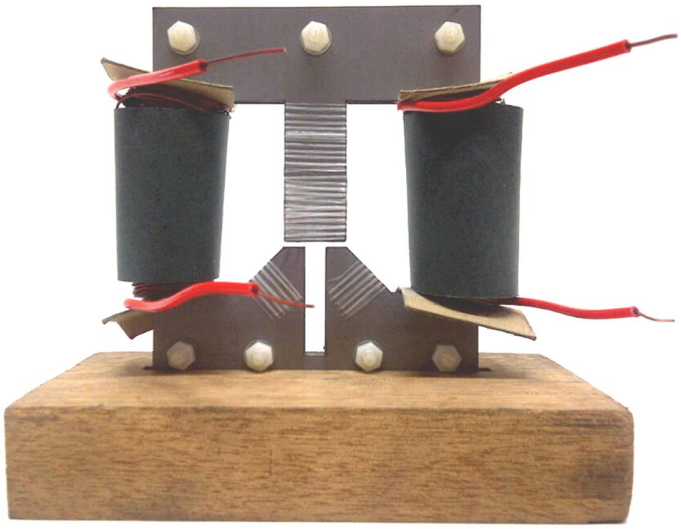

Fig. 3.18 Physical construction of magnetic circuit for Design 1

According to the FE simulation, the average normal flux density in the air gap is 1T. When taking measurements on the force rig, with each coil having 200 turns and excited up to a maximum of 25A (for a very short time due to conductor size), it was not possible to achieve a normal flux density in the air gap of more than 0.35T. The device used to measure the flux density in the air gap is a Brockhaus Messtechnik Model 410 Gaussmeter using a MST-410 transverse Hall voltage probe, shown in Figure 3.19. This equipment was tested and shown to be correctly calibrated at the time of measurement.

Fig. 3.19 Gaussmeter with transverse Hall probe

In addition to the disparity between the simulated and measured air gap flux densities, a number of issues came to light when the CapaNCDT measuring system arrived from Germany, exposing some design flaws in the force rig, which are listed below.

- The sensor requires a measurement target with an extremely flat surface, having no irregularities (polished if possible), but the target in this design is a highly irregular surface due to the lamination stack.
- The sensor requires maximum stability while performing the measurement, and clamping it securely into position in the cavity proved to be extremely difficult.
- The maximum measuring range from sensor to target is 0.2mm, requiring very delicate position adjustment of the sensor, which the sensor cavity arrangement makes very difficult.

After careful consideration of all the facts it was decided to redesign the force rig and simplify it in order to minimise the margin of error. The following design is the result.

3.2.4 Design 2

To increase the flux in a magnetic circuit is a simple case of increasing the MMF, according to F = IN, therefore the number of turns of each coil has been increased from 200 to 300. As flux density is derived from flux per cross-sectional area, it is decided to forego the E-piece design and reduce the width of the tooth from 20mm to 5mm. For the same reason, the stack length (z-axis) of the rig has been reduced to 5mm. The FE simulation of this design shows that, when the average normal flux density in the air gap is 1T, the average normal flux density in the tooth and lower middle limb is below saturation, according to the manufacturer's B-H data. This geometry is therefore considered sufficient for magnetic purposes. The air gap flux distribution in the previous design was concentrated to the left and right hand side due to the sensor cavity in the lower middle limb. As the measurement target must now change, the sensor cavity can be removed, leaving an air gap with two flat surfaces, allowing for an even flux distribution.

The sensor now requires a new target but still needs to measure the y-displacement of the tooth. This can be achieved by the sensor being firmly secured to the side of the tooth,

where the y-displacement of the sensor will be directly proportional to the y-displacement of the tooth. The sensor will now face a polished flat metal target beneath it that is separate from the rig and secured to the wooden supporting base. Position adjustment is now possible through the wooden base – to adjust the height of the target in order to satisfy the measurement range of the sensor – while the sensor remains fixed in position.

A small block of wood with a fashioned groove to fit the sensor could be made and secured to the side of the tooth, by means of acrylic glue, flush with the tooth tip in order for the maximum y-displacement of the tooth to be relayed to the sensor. The sensor would then either be strapped or glued firmly into this groove. This arrangement would allow some distance between the sensor and target from the core, effectively isolating them from the magnetic circuit. Finally, due to challenges that arose when winding the coils by hand during the first design, more space has been provided for the windings (x-axis) this time round. An illustration of force rig Design 2 is shown in Figure 3.20.

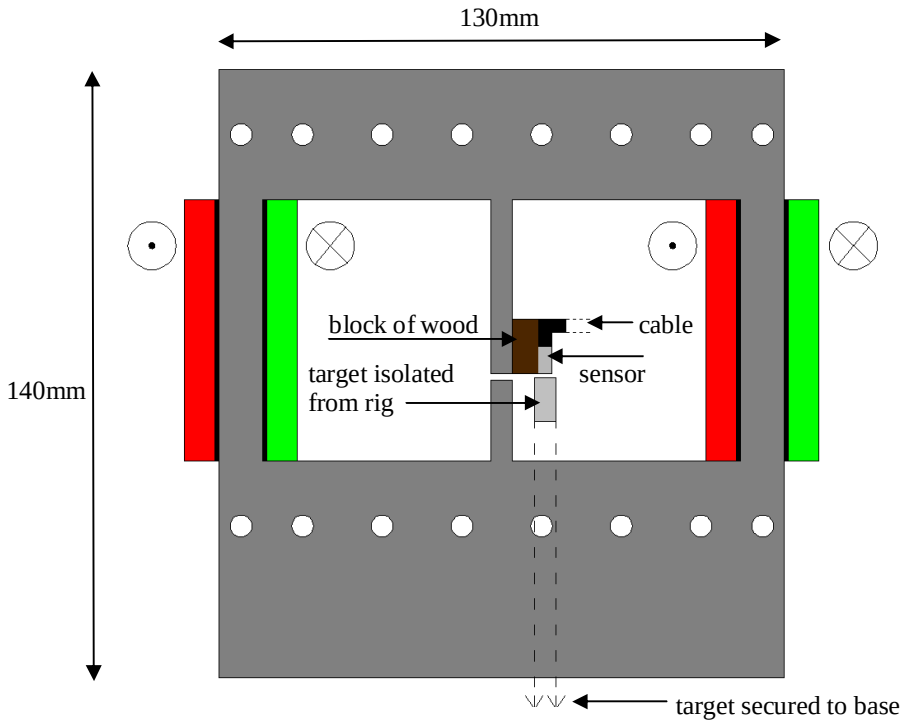

Fig. 3.20 Force rig Design 2

According to the FE simulation, an average normal flux density of 1T is achieved in the air gap by exciting each coil of 300 turns with a dc current of 5.3A. The 2D flux plot for the simulation is shown in Figure 3.21.

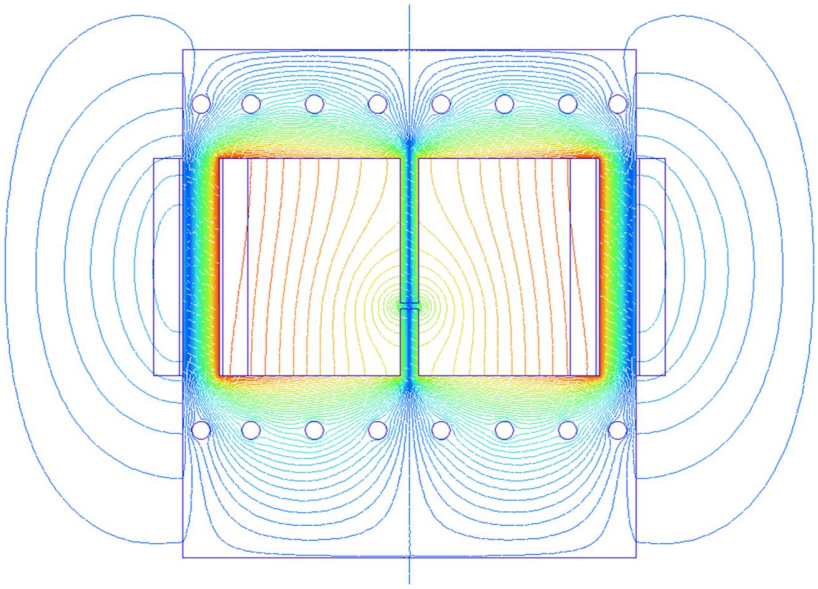

Fig. 3.21 2D flux plot for Design 2

The normal flux density graph obtained by defining a path through the centre of the air gap is shown in Figure 3.22, with the average indicated by the red line.

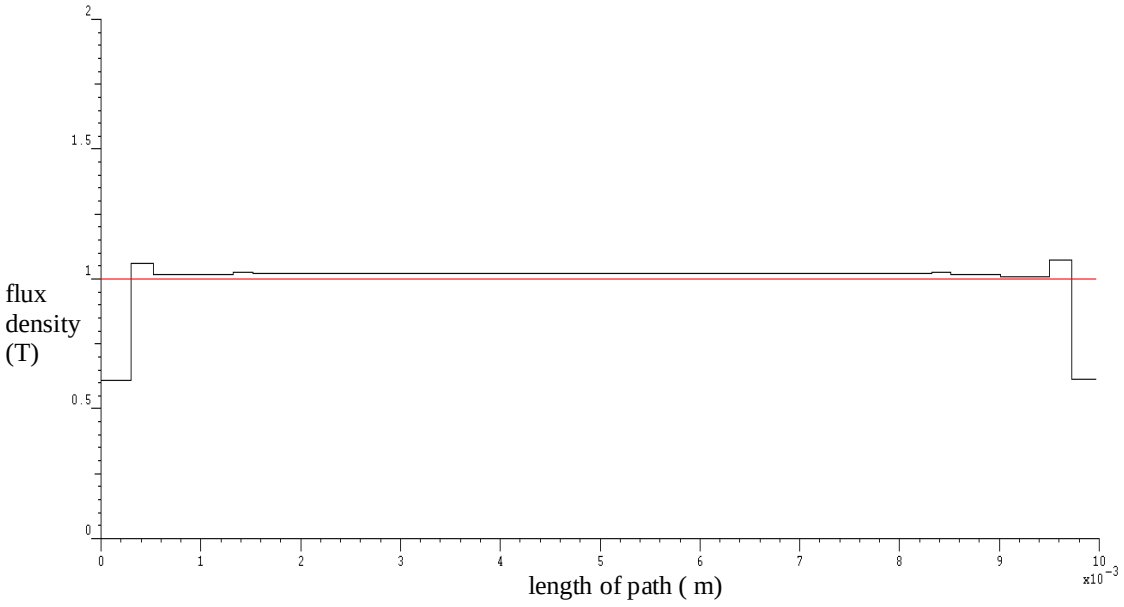

Fig. 3.22 Graph of flux density normal to the path defined through the air gap

A photograph of the magnetic circuit for the second design is shown in Figure 3.23.

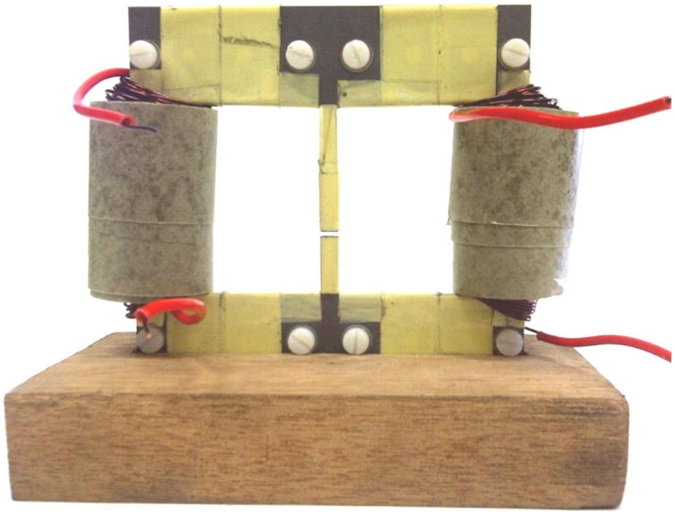

Fig. 3.23 Physical construction of magnetic circuit for Design 2

Once again the flux density measured in the air gap did not match the FE prediction. According to the simulation, the average normal flux density in the air gap is 1T. When taking measurements on the force rig, with the two coils each having 300 turns and again excited up to a maximum of 25A for a short time, it was not possible to achieve a normal flux density in the air gap of more than 0.46T. It has therefore been decided to conduct an analytical investigation by using first principles in order to check the modelling approach.

3.2.4.1 Analytical investigation

If the required flux density in the air gap is known, it is possible to determine the required current in the coil once the number of turns has been chosen. Two methods are used to calculate the current – namely, Ampere's Law for a magnetic field produced by a current-carrying coil, and Hopkinson's Law of the magnetic circuit, with results compared. The flux path is integral to both analytical solutions and is shown in Figure 3.24.

As there is perfect symmetry between the left and the right half of force rig Design 2 and magnetic flux lines form closed loops, it is deemed necessary to model only one half of the rig, i.e. the left half. These results can then be mirrored onto the right half of the rig.

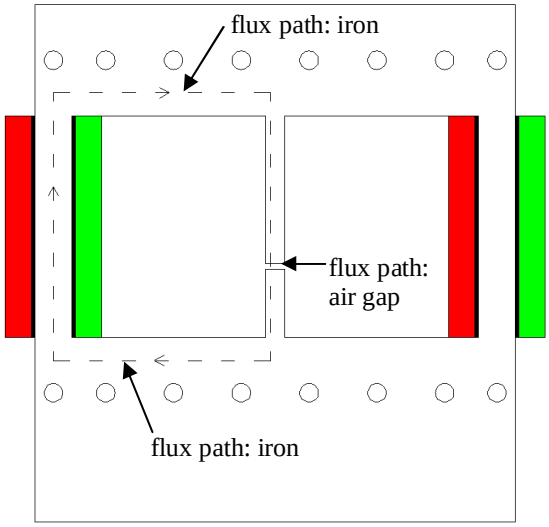

Fig. 3.24 Flux path for left half of Design 2

Ampere's Law states $\oint \mathrm{H} d\ell = \mathrm{NI}$ which means that the summation of the magnetising force H along the total flux path ℓ is equal to the total ampere-turns NI. Values for H along this path can be extracted from the manufacturer's data (refer to Appendix B) once the values for flux density B are known. In order to know the magnetising force in the core an assumption has to be made. As shown in Figure 3.25 below, a number of paths have been defined through the tooth and lower middle limb of the FE model, in order that the flux density normal to these paths may be determined. This is done to formulate an average of flux density in the core when the flux density in the air gap is 1T.

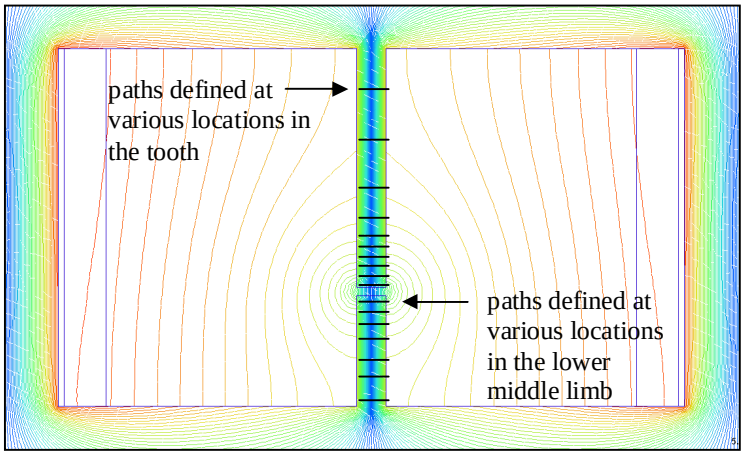

Fig. 3.25 Paths defined in the core

There are ten paths defined at various locations in the tooth. The values of flux density normal to these paths are, from top to bottom: 1.77T, 1.72T, 1.66T, 1.6T, 1.55T, 1.5T, 1.45T, 1.39T, 1.27T and 1.09T. There are seven paths defined at various locations in the lower middle limb. The values of flux density normal to these paths are, from top to bottom: 1.09T, 1.3T, 1.39T, 1.45T, 1.49T, 1.56T and 1.61T. After taking an average of the summation of all values in the tooth and lower middle limb the average flux density in the core $B_{c(ave)}$ can then be assumed to be 1.464T.

As the permeability of air μ_0 is known, and $B = \mu H$, this gives the magnetising force in the air gap $H_g = 795.775 \times 10^3 \frac{A}{m}$. As $B_{c(ave)}$ is known, the manufacturer's B-H data can be consulted to give the average magnetising force in the core $H_{c(ave)} \propto 1226 \frac{A}{m}$.

This method does not take the third dimension (z-axis) into account. There are 300 turns on the coil; the length of the flux path is 0.2609m in the iron and 0.0015m in the air gap. The current required in the left coil, according to Ampere's Law, is therefore

$$\left(H_{c(ave)} \times \ell_c\right) + \left(H_g \times \ell_g\right) = NI \qquad (3.3)$$

$$\left(1226 \times 0.2609\right) + \left(795774.715 \times 0.0015\right) = 300I$$

$$\therefore I \propto 5A$$

This can be confirmed by making use of Hopkinson's Law ($F = \Phi \times \Re$). This method takes the reluctance $\Re$ of the circuit into account and also the 5mm depth of the rig in order to determine the cross-sectional area of the flux path. The current required in the left coil, according to Hopkinson's Law, is determined by

$$\Re_{iron} = \frac{\ell_{path}(m)}{\mu_{iron} \times A_{path}(m^2)} = \frac{0.260912}{0.001194 \times (0.260912 \times 0.005)} = 167.504188 \times 10^3 \frac{At}{Vs} \qquad (3.4)$$

$$\Re_g = \frac{0.0015}{0.000001256 \times (0.0015 \times 0.005)} = 159.235669 \times 10^6 \frac{At}{Vs}$$

$$\Re_{cct} = \Re_{iron} + \Re_g = 159.403173 \times 10^6 \frac{At}{Vs}$$

$$\Phi_g = B_g(T) \times A_g(m^2) = 1 \times (0.0015 \times 0.005) = 7.5 \times 10^{-6} Wb \quad (3.5)$$

$$F = \Phi \times \Re = 7.5 \times 10^{-6} \times 159.403173 \times 10^6 = 1195.524 At \quad (3.6)$$

$$I = \frac{F}{N} = \frac{1195.524}{300} \propto 4A \quad (3.7)$$

Where:

N = number of turns in the coil

I = current flowing in the coil (A)

Φ = magnetic flux in the circuit (Wb)

Both methods are in agreement that a coil of 300 turns excited by between 4 – 5A should produce a normal air gap flux density of around 1T. This verifies the FE simulation and suggests that one or more elements of the physical rig are incongruent with the simulated model. Therefore, a process of elimination of other considered sources of error is undertaken, which includes all of the following.

- The current supplied to each coil was measured with a clamp-on ammeter. The measured currents showed agreement with the output display of the dc power supply and the excitation polarity of each coil was shown to be correct.
- It was investigated whether any significant amount of turns had been shorted together when hand winding the coils. This was not the case, as the measured resistance of each coil was shown to agree with a simple resistance calculation.
- A lamination stacking factor of 0.95 was included in the FE simulation, showing a reduction in air gap flux density of less than 1%.
- As the excitation is dc, eddy currents in the core are not considered a problem.
- As solid laminated plates are used, no reluctance is added by joints in the core.
- The type of silicon steel delivered by the supplier was confirmed to be correct.
- The assumption made about the depth of the FE model was brought into question.

Having eliminated the first six possible sources of error from the list above, only one possibility remained, namely, the assumed depth of 1mm for the FE model. When comparing the geometry of the simulated model and the physical rig, all the dimensions in the x- and y-directions are identical, and therefore the only remaining factor is the z-direction. When scaling the FE mesh, if the z-axis (assumed to be 1m) is not affected by the 0.001 scaling factor, this may result in magnetic saturation setting in to the physical rig a lot sooner than in the FE model, due to a large difference in core volume. If any regions of the core in the physical rig were to become saturated, a MMF drop would occur in the magnetic circuit, resulting in a reduction in the air gap flux density. This may explain the difference in measured and modelled results.

Therefore, in the following design, the stack length (z-direction) of the physical rig is increased, and additional improvements are made to the geometry in other directions, in order to reduce saturation and simplify the design to further minimise the margin of error.

3.2.5 Design 3

A C-shape core design is adopted to simplify the magnetic circuit as much as possible. Due to practical and financial limitations, a 1m stack length is not feasible, and therefore the laminations are cut from two sheets of M250-35A, giving a stack length of 23mm, being four times that of the previous rig. A single source of dc excitation is now used, coming from the left limb wound with the number of turns increased to 1000. The considerable increase in the number of turns will help to overcome any MMF drops that may exist in the circuit, and should decrease the current required to excite the coil, thereby reducing overloading of the conductor. The length of the left limb is doubled in order to accommodate the winding and the width of the limb(s) and height of the yoke and core base are now double that of the previous rig.

Before giving attention to the position of the sensor and target, the most important criterion that must be satisfied is the flux density in the air gap. According to the FE simulation, an average normal flux density of 1T is achieved in the air gap by exciting the coil of 1000 turns with a dc current of 1.3A. However, having taken the disparity in the z-direction between the simulated model and the physical rig into account, the excitation

conditions for the physical rig are no longer expected to match those of the simulated model. For this reason, the design focus will now be on the physical rig only and not the simulated model, with the purpose of achieving the required flux density in the air gap. The reason for the difference between dc excitation requirements of the simulated model and the physical rig is investigated further in Section 5.3.1.3.

With the new design having all of the above mentioned characteristics, it was possible to achieve a normal flux density physically measured in the air gap of 1.015T, at an excitation current of 22.3A dc. This is shown in Figure 3.26.

Fig. 3.26 Flux density measured in the air gap of the magnetic circuit for Design 3

Although the required air gap flux density was achieved, it is clear that there was no significant reduction of current in the conductor. According to Appendix D, a 1mm^2 copper conductor with an insulation temperature rating of 200°C can continuously carry a current of 35A. As the enamel insulation for the conductor being used has a temperature rating of at least 180°C and the current required is less than 25A, the 1mm^2 conductor is able to operate safely, but would generate excessive heat. This would lead to thermal expansion of both the coil and the core, introducing measurement errors, as heat-flexing of both the limb and the coil (being in contact with the core) would widen the air gap.

The coefficients of linear thermal expansion of steel and copper are 13µm/m/°C and 16.6µm/m/°C respectively (The Engineering Toolbox, 2013). This means that, for every 1°C rise in temperature, the left limb, being 120mm long, will elongate in the y-direction by approximately 1.56µm, and the coil, also being 120mm long, will expand in the y-direction by approximately 1.992µm.

The coil therefore needs to be rewound, using thicker gauge conductor to dissipate less heat, and wound onto a 'former' that thermally isolates it from the core. The latter is achieved by placing a 100mm long hollow tube of hard cardboard around the limb to be wound, allowing an air gap ranging between 1 – 10mm between the coil and the core. In addition, flat cut-outs of masonite board are fitted around the limb on each end of the tube, thereby ensuring 10mm of free space above and below the coil. This former achieves, in essence, a 'floating coil' effect, creating a heat barrier between the coil and limb, yoke and core base. This has the disadvantage of 20mm of winding space being lost in the y-direction, meaning that the size of the coil will now increase in the x-direction.

In order that the excitation current may be reduced, the aim is now to achieve 1500 turns on the coil, and a conductor size of $1.5mm^2$ is chosen as a trade-off between greater current-carrying capacity and utilisation of space for maximum number of turns. To check the suitability of this conductor size, Appendix D can be referenced in conjunction with the following mathematical calculation to determine the current effecting the maximum temperature change before insulation breakdown.

$$V_{con} = A_{con} \times \ell_{con} = 1.5\times10^{-6} \times 300 = 0.00045m^3 \tag{3.8}$$

$$M_{con} = V_{con} \times \rho_{con} = 0.00045 \times 8.9\times10^{3} = 4.005kg \tag{3.9}$$

$$E_{con} = M_{con} \times c_{con} \times \Delta T_{con} = 4.005 \times 385 \times 160 = 246708J \tag{3.10}$$

$$P_{con} = \frac{E_{con}}{t_{max}} = \frac{246708}{10} = 24670.8W \tag{3.11}$$

$$I_{\Delta Tmax} = \sqrt{\frac{P_{con}}{R_{con}}} = \sqrt{\frac{24670.8}{4.7}} = 72.45A \quad (3.12)$$

Where:

V_{con} = Volume of conductor (m^3)

A_{con} = Cross-sectional area of conductor (m^2)

ℓ_{con} = Approximated length of conductor (m)

M_{con} = Mass of conductor (kg)

ρ_{con} = Density of (copper) conductor (kg/m^3)

E_{con} = Energy dissipated by conductor (J)

c_{con} = Specific heat characteristic of (copper) conductor (J/kg°C)

ΔT_{con} = Rise in temperature of conductor (°C)
from room temperature (20°C) to insulation breakdown temperature (180°C)

P_{con} = Power dissipated by conductor (W)

t_{max} = Maximum duration of time that current flows in conductor (s)

$I_{\Delta Tmax}$ = Current effecting maximum temperature change (A)

R_{con} = Measured resistance of conductor (Ω)

Therefore, to reach insulation breakdown temperature, the conductor would have to carry 72.45A for 10s. This conductor size is therefore perfectly suitable as the dc power supply being used has a maximum output of 25A. It is now possible to manipulate the above equations and work the calculation back to determine the rise in temperature of the conductor, at the maximum current of 25A, for the maximum time duration of 10s, shown by the following.

$$P_{con} = I^2 \times R_{con} = 25^2 \times 4.7 = 2937.5W$$

$$E_{con} = P_{con} \times t_{max} = 2937.5 \times 10 = 29375J$$

$$\Delta T_{con} = \frac{E_{con}}{M_{con} \times c_{con}} = \frac{29375}{4.005 \times 385} = 19.05°C$$

Therefore, the 1.5mm^2 conductor temperature is raised from 20°C to 39.05°C when it carries 25A for 10s. These are the worst case conditions expected, and precautions have been taken to thermally isolate the steel core from the coil. However, the temperature around the core will still be raised, and for this reason, a thermocouple is connected directly onto the steel of the limb before fitting the former in place, so that the core temperature may be monitored. In addition, the rig will be housed inside a cardboard box with a second thermocouple used to measure the ambient temperature inside the box. This will also isolate the sensor from electrostatic fields in the surrounding environment.

The new coil was then wound onto the former, using the 1.5mm^2 conductor, achieving the required 1500 turns, and this time giving a measured air gap normal flux density of 1.009T at an excitation current of 7.9A dc, shown in Figure 3.30.

Attention can now be given to the position of the sensor and measurement target. The tooth in this design is the upper right limb, to which the target will be attached directly. The target is a flat cut-out of aluminium shaped to fit around the tooth tip and secured in place with acrylic glue. As the target is now in direct contact with the core it is constructed of aluminium so as not to interfere with the flux pattern around the air gap. A clean, polished surface area of at least 10mm in diameter faces the sensor, which is attached to the lower right limb; this more than satisfies the minimum measuring spot of 5mm. Earthing of the target to the controller is achieved by means of a crocodile clip.

A sensor housing has been made from a block of wood in which the sensor is firmly secured to ensure absolute rigidity. This housing is fixed with acrylic glue to the core base. This is done to ensure that any measured y-displacements are due only to the movement of the target and not to any movement of the sensor. The sensor housing is then strapped to the lower right limb to ensure that the sensor position does not change in the x- or z-direction. The sensor is now securely in position.

When securing the target in position, the following procedure is carried out in order to stay within the maximum measuring range of 0.2mm between sensor and target. A 0.04mm (smallest available size) feeler gauge is placed between the sensor and target, and a small weight is then placed on the area of the target directly above the sensor. This is done to ensure that the best possible alignment is achieved between sensor and target as the glue sets into position. Once the glue has been left to dry overnight, with the feeler gauge and small weight in place, these are then removed before any measurements are undertaken. An illustration of the finalised force rig Design 3 is shown in Figure 3.27.

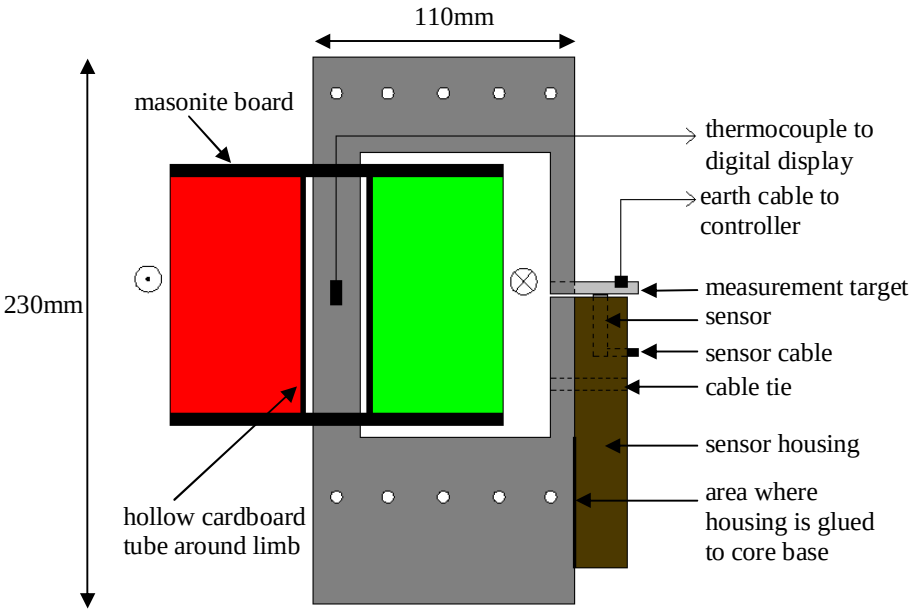

Fig. 3.27 Force rig Design 3

An aerial view of the sensor in position before the target is set in place is shown in Figure 3.28, and the final position of the target relative to the sensor, once both are firmly fixed into position, is shown in Figure 3.29, where the measurement air gap can be clearly seen.

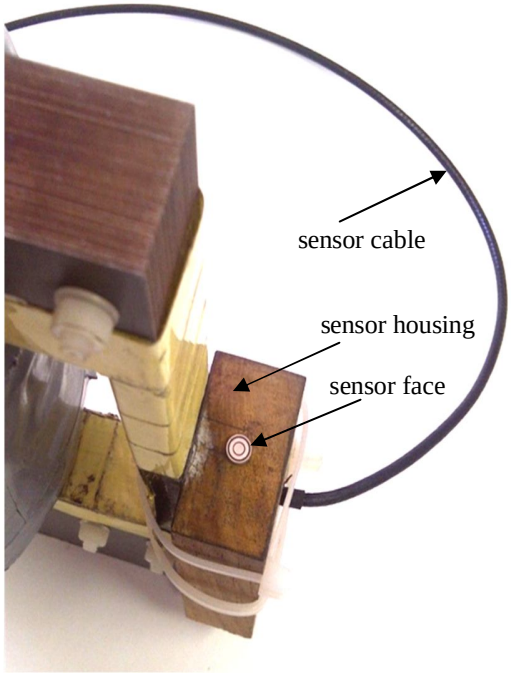

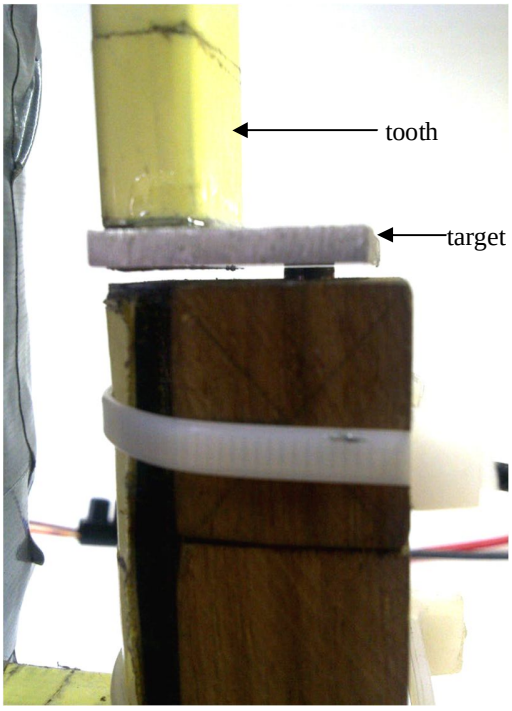

Fig. 3.28 Aerial view of sensor position

Fig. 3.29 Sensor and target in position

A photograph of force rig Design 3 is shown in Figure 3.30, where the air gap normal flux density, temperature of the limb and exciting dc current are digitally displayed.

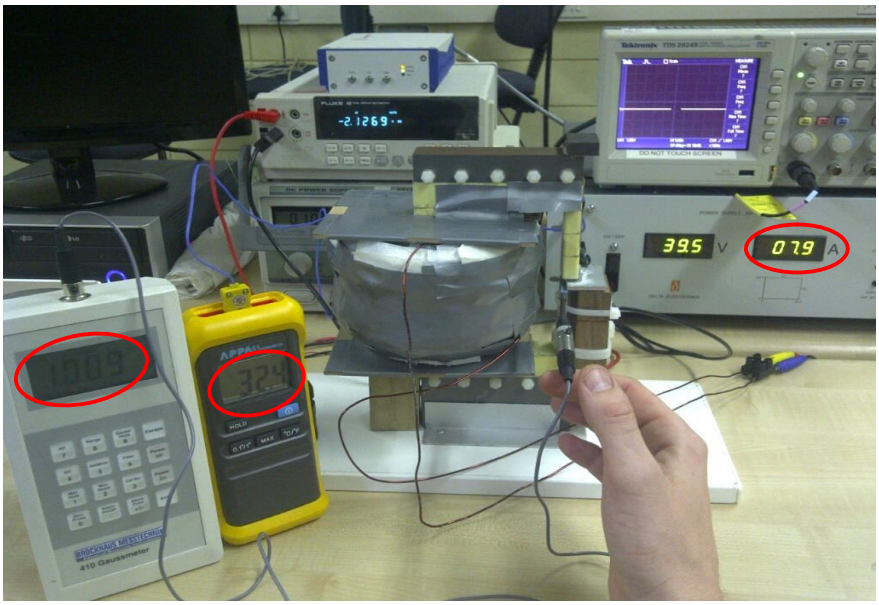

Fig. 3.30 Flux density measured in the air gap of force rig Design 3

Now that the required air gap flux density has been achieved and the thermal expansion of the core has been addressed, there is one final issue, which has to do with the shape of the core. When a C-core is energised, the magnetic attracting force in the air gap, together with induced magnetostriction forces, will cause the entire core structure to constrict, according to a study by Vandevelde and Melkebeek (2001) and illustrated in Figure 3.31.

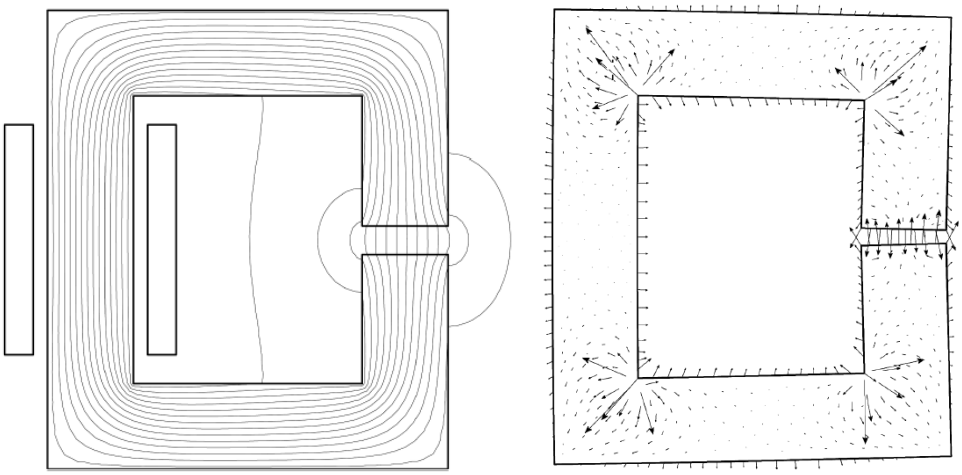

Fig. 3.31 Constriction of a C-core due to magnetic excitation (Melkebeek, 2001)

This flexible constriction of the core, associated with its asymmetrical shape, will cause measurement errors, as the goal of this work is to measure only the elastic y-displacement of the tooth. Although displacement experiments can still be done using this design, it is not the best representation of the conditions in an EM. Therefore, all of the information gathered throughout the design process will now be utilised to produce one final force rig design which follows.

3.2.6 Design 4

In order to cancel out the constriction of the core a symmetrical design is once again adopted where the yoke is supported by two limbs. Two coils are therefore used to provide magnetic excitation, each using 1.5mm^2 copper conductor and having 1000 turns. A maximum core stack length (z-axis) of 26mm is allowed in order to fit the cardboard tube formers for winding the coils around the limbs. This stack length is achieved by using 6 sheets of M250-35A silicon steel for the laser-cut laminations.

The tooth in this design is the middle limb which now extends down to the core base, stopping 1.5mm before reaching it, this space being the air gap. By eliminating the lower middle limb from the design (as in previous designs), the sensor housing can now be secured entirely to the core base, offering greater rigidity. When taking displacement readings via oscilloscope on Design 3, it was noticed that the rate of change in the voltage output (giving displacement) reduced considerably some time before the air gap normal flux reached 1T. This is most likely due to one or more regions of the core being saturated. Therefore, the transformer E-piece shape is once again used, making the tooth double the width of the limbs in order to promote a homogenous flux distribution. The yoke and core base are again at least three times the width of the limbs for mechanical stiffness. A thermocouple is placed directly onto the steel of each limb before the coils are wound, as seen in the photograph of the core in Figure 3.32.

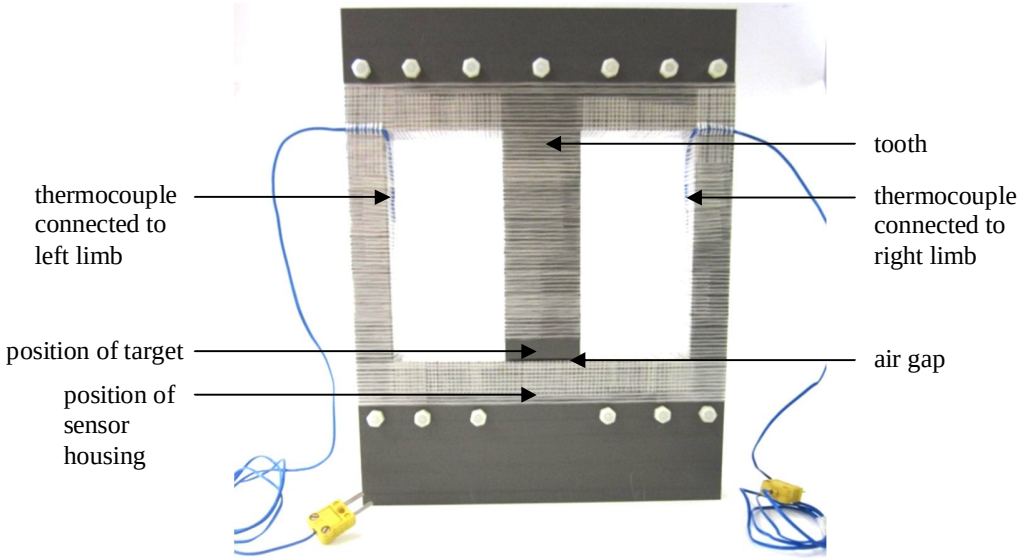

Fig. 3.32 Core structure of Design 4

A photograph of the sensor, in position, and the target, before being placed in position, is shown in Figure 3.33. With each coil achieving 1000 turns, a normal air gap flux density of 1T was physically measured, at a dc current supply of 24A, split in parallel to supply each coil with approximately 12A dc. This is shown in the photograph in Figure 3.34, where the force rig is housed in the cardboard box for temperature and electrostatic field isolation. A photograph of the complete force rig, inside the box, is shown in Figure 3.35.

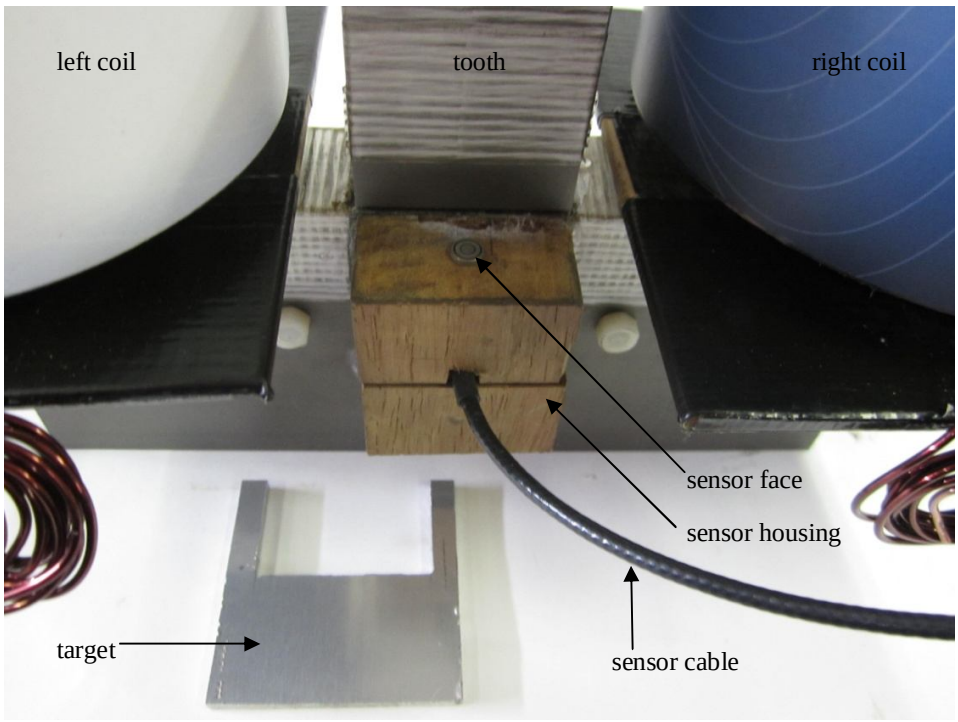

Fig. 3.33 Sensor secured into position before the target is attached to the tooth

An illustration of force rig Design 4 is shown in Figure 3.34.

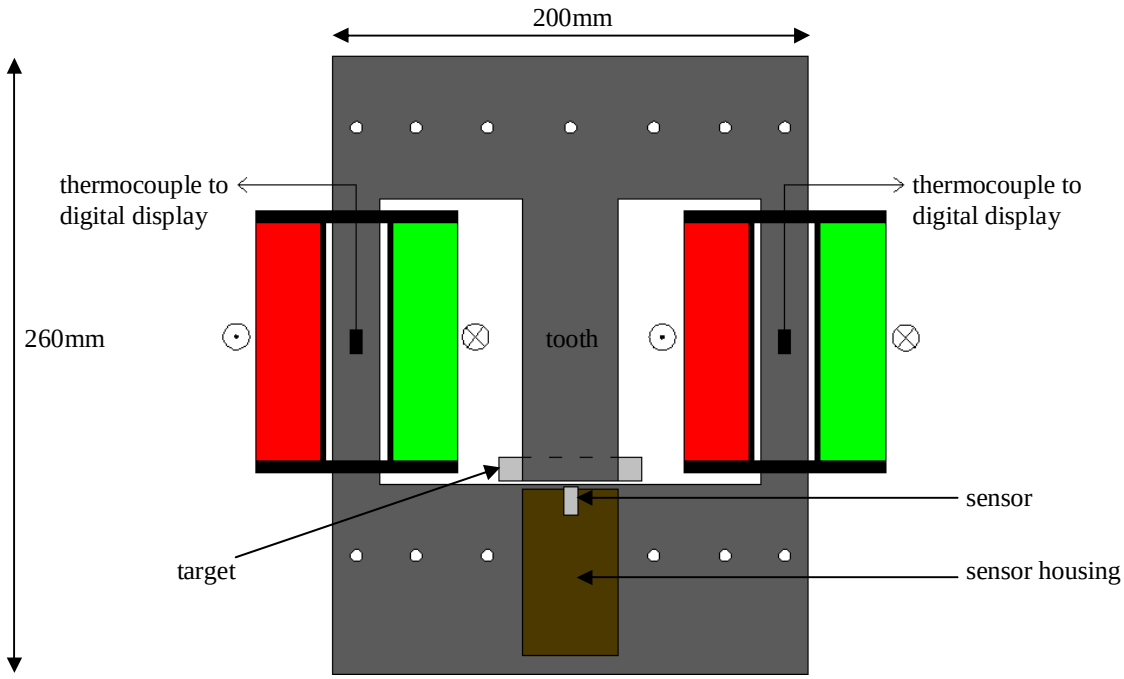

Fig. 3.34 Force rig Design 4

Fig. 3.35 Flux density measured in the air gap of force rig Design 4

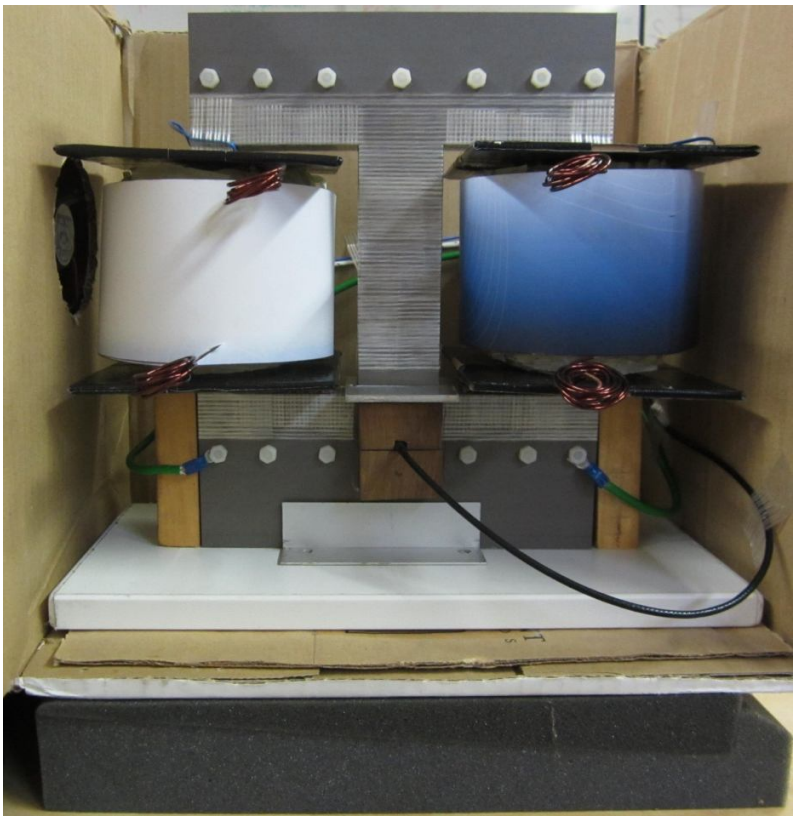

Fig. 3.36 Complete force rig Design 4 inside isolation box

Chapter 4

Force-induced displacement measurement

4.1 The test bench

The test bench, as shown in Figure 4.1, comprises the force rig, isolation box, capacitive displacement measurement system, digital multimeter, oscilloscope, Gaussmeter, a range of known masses, temperature regulating system, vibration damping system, and dc power supplies. The displacement measurement, data acquisition, temperature regulating and vibration damping systems are discussed in more detail in the following sections.

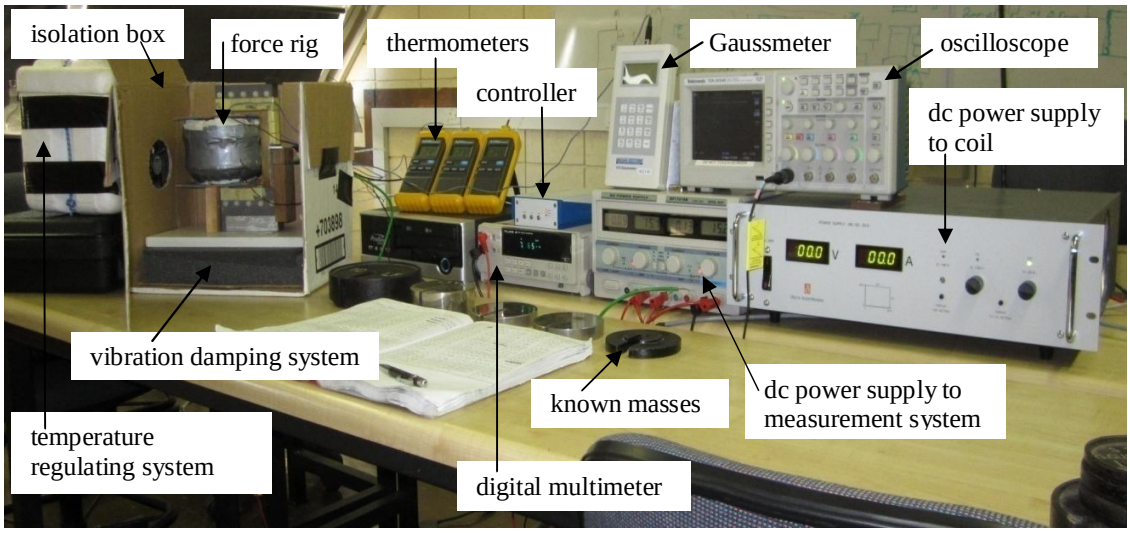

Fig. 4.1 The test bench

4.1.1 The capacitive displacement measurement system

When choosing a measuring system, the most important aspect to consider is its performance criteria relative to the needs of the measurement to be taken. These criteria are divided into static and dynamic system characteristics. Static characteristics describe the performance criteria related to the measurement of quantities either remaining constant or varying very slowly. Dynamic characteristics describe the relationship between the input and output of the system when the quantity to be measured

(measurand) is varying rapidly. It is also important to take under consideration the environmental conditions in which the measuring instrument will have to operate and the accuracy of the system over time. The respective costs of the available options are then weighed up once these preliminary steps have been carefully considered. This process has been carried out in Section 3.1, arriving at the measuring system chosen for this thesis, being capacitive displacement measurement. Dynamic characteristics are not applicable to this study and will therefore not be further explained, but a brief description of some important static characteristics to be considered can be found in Appendix E.

The CapaNCDT measurement system, provided by Micro-Epsilon, consists of a CS02 sensor, CC1C/90 sensor cable and DT6300 controller, the details of which are explained in the sections to follow. The technical specifications for the sensor and controller, as provided by the manufacturer, can be found in Appendix F.

4.1.1.1 Measuring principle (Micro-Epsilon, 2012)

As stated in Section 3.1.6, the measuring principle is based on the operation of an ideal plate-type capacitor, where the sensor and measurement target form the two plate electrodes. When measurement is performed using one sensor only, the target is grounded to the controller. When two or more sensors are used, a function called 'synchronous operation' is employed which eliminates the need for earthing of the target.

Following on from the explanation provided in Section 3.1.6, the CapaNCDT system determines the reactance X_c of the 'capacitor' which is directly proportional to the distance between the plates, according to $X_c = \frac{1}{j\omega\varepsilon_r\varepsilon_0 \frac{A}{d}}$.

As j, ω, ε_r, ε_0 and A remain constant during measurements, they can be replaced by a constant K, where $K = \frac{1}{j\omega\varepsilon_r\varepsilon_0 A}$.

Therefore $X_c = K \times d$ making the reactance only a function of the distance between the plates.

4.1.1.2 The sensor (Micro-Epsilon, 2012)

Because the sensors are designed as guard ring capacitors, as shown in Figure 4.2, the measuring principle is achieved almost ideally in practice. The guard field allows for a perfectly homogenous measuring field giving extremely high accuracy and precision measurements free from interference. The sensor is of tri-axial design meaning that the guard ring electrode, the grounding and the measurement electrode are all located on the front edge of the sensor. The sensor is calibrated at the Micro-Epsilon factory for metallic targets as standard, which perfectly suits the needs of this thesis.

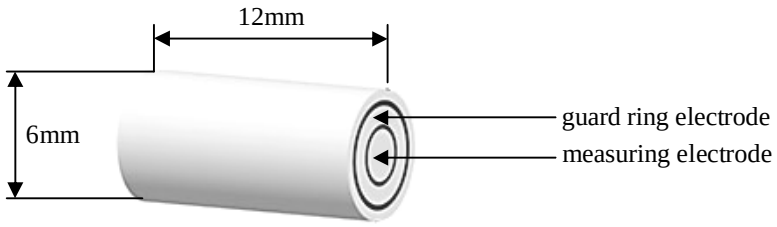

Fig. 4.2 CS02 capacitive displacement sensor (Micro-Epsilon, 2012)

Almost ideal linearity of the measuring signal is attained for metal targets without the need of any electronic linearisation in the controller. Slight changes in the magnetic properties or conductivity of the target do not affect the linearity or sensitivity. The standard measuring range may be adjusted (increased or decreased) at the controller by a factor of 2, where halving the measuring range corresponds to a proportional increase in resolution while doubling the measuring range corresponds to a proportional decrease in resolution. As the measuring process is area related, the target requires a minimum 'measuring spot' or area, which depends on the type of sensor used. The linearity and sensitivity of the sensor is affected when the target is either too small or not 'perfectly' flat (although this is virtually impossible at the nano-level).

If a tilting angle is introduced between the sensor and the target, a measurement error will be incurred, as the field will distort when the edge areas of the sensor move either closer to or further away from the target. However, if the front edge (face) of the sensor were to become shorted by touching the conductive target, it will not damage the preamplifier as the sensor is designed as short circuit proof.

4.1.1.3 The sensor cable (Micro-Epsilon, 2012)

The sensor is connected to the signal conditioning electronics (controller) by a unique, double-screened, low-noise tri-axial cable having a high quality connector on one end which the sensor plugs into. The sensor can be disconnected and reconnected to the cable without the need for recalibration. Due to an almost perfectly impermeable electrical shield, a particularly high quality signal and level of precision is achieved. For this application, the cable has a standard length of 1m which cannot be adjusted, and a 90º bend connector is used, as shown in Figure 4.3.

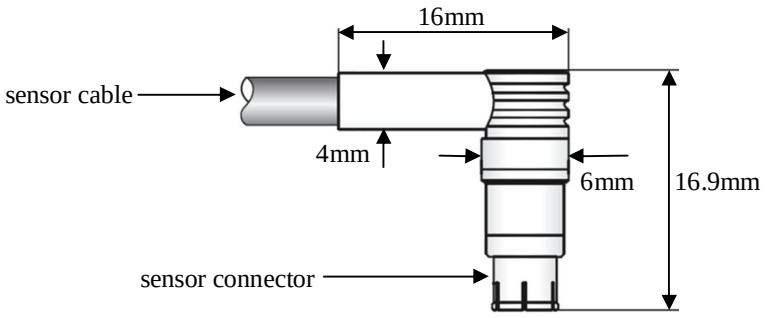

Fig. 4.3 CC1C/90 sensor cable connector (Micro-Epsilon, 2012)

4.1.1.4 The controller (Micro-Epsilon, 2012)

The resolution of this measuring system is governed by the controller in conjunction with the full-scale output (FSO) of the sensor. Shown in Appendix F, a static resolution of 0.001% of 10V (0.2mm) equates to 0.00001 × 0.0002m which arrives at a resolution for this measurement system of 2nm.

The controller consists mainly of an oscillator and demodulator unit stored in aluminium housing. The oscillator supplies the sensor with amplitude stable sinusoidal current at a constant frequency of 31 kHz. The demodulator provides demodulation, linearisation and amplification of the measuring signal. The linearisation function is switched off for metallic targets. On the front of the controller, shown in Figure 4.4, there are three trimmer potentiometers allowing adjustment of the linearity, gain and zero point, as well as three LEDs to indicate the status of the controller, whether or not the sensor is in measuring range and if the zero point has been changed from the factory setting.

On the back of the controller, shown in Figure 4.5, are four female pin-connector sockets for the power (and output) cable, sensor cable, output signal cable and synchronisation cable. Synchronisation is not applicable in this study as only one sensor and controller are used. The 8-wire power cable consists of an outer screening mesh which surrounds all cable wires as well as an inner screening mesh which surrounds the three signal wires, thereby ensuring the high-quality signal. As the displacement measurements in this work are relative to a change in signal voltage, only the output voltage and analogue ground signal wires will be used, and not the output current.

Fig. 4.4 Front of the controller (Micro-Epsilon, 2012)

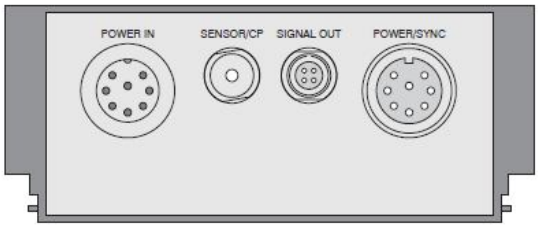

Fig. 4.5 Back of the controller (Micro-Epsilon, 2012)

4.1.2 Data acquisition system

In this work, the primary measurand is the analogue voltage output signal of the capacitive displacement measurement system, which needs to be either displayed or recorded. For this purpose, a Fluke 45 digital multimeter and a Tektronix TDS2024B oscilloscope are used, both shown in the photograph in Figure 4.1. The digital multimeter is purely an analogue-to-digital output signal display device, where a change of 0.0001V equates to 2nm of displacement. The oscilloscope displays the analogue voltage output signal graphically, where the change in voltage output is seen as a function of time; the data for each time period can also be recorded and stored for later use.

In addition to the primary measurand mentioned above, air gap normal flux density is measured using the Brockhaus Messtechnik Model 410 Gaussmeter, having a resolution of 0.001T, and all temperatures are continuously monitored using APPA51 digital thermometers with thermocouple measuring probes, having a resolution of 0.1°C, both of which can be seen in the photograph in Figure 4.1.

4.1.3 Temperature regulating system

In order to perform each measurement at the same core and ambient temperature, a temperature control system was devised. Firstly, the force rig is housed inside a cardboard box to isolate it from the outside environment. A cooler box filled with ice packs and having two cut-outs on opposite ends, one incorporating an input (sucking) fan and one incorporating an output (blowing) fan, is then positioned next to this box. The cut-out with the blowing fan is perfectly aligned to a cut-out in the cardboard box. When connected to the power supply, the sucking fan sucks air into the cooler box, which is cooled by the ice packs and blown onto the force rig by the blowing fan. The temperature of the force rig is thus regulated and this system is shown in the photograph in Figure 4.6.

Fig. 4.6 Temperature regulating system

4.1.4 Vibration damping system

Due to the sensor being extremely sensitive to external vibrations, the rig is insulated from its environment by placing it on Auralex vibration-absorbing foam, used to support studio monitors in professional sound engineering studios, shown in Figure 4.7.

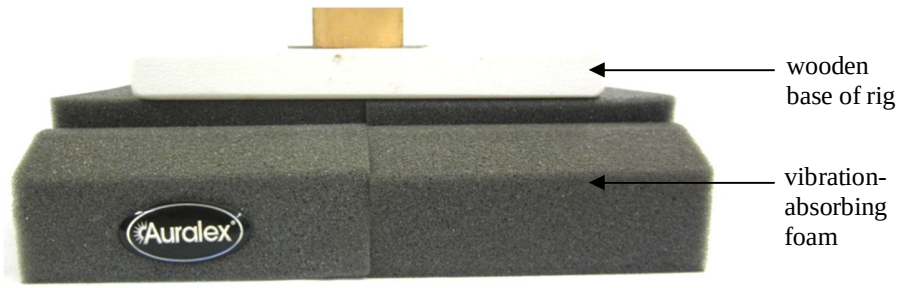

Fig. 4.7 Force rig supported by Auralex vibration-absorbing foam

4.2 Experiments

In this section displacement measurements will be conducted on force rig Design 3 and Design 4 which involve primarily the measurement of output voltage by the capacitive displacement measurement system. A change in output voltage translates directly to a change in air gap length between the sensor and measurement target, which is in direct proportion to the y-displacement of the tooth due to magnetoelastic strain, which is the focus of this thesis. The measurement of air gap flux density and various temperatures are also necessary measurands, the latter being done in order to reduce errors in the primary measurand, therefore making the results more meaningful.

The first two experiments are conducted on force rig Design 3, with the second experiment being done after a physical alteration is introduced to the rig in order to restrain the constriction of the C-shape. The third experiment is conducted on Design 4.

4.2.1 Experiment 1

It has been stated in Section 2.3.1.3 that the magnetic attraction force in the air gap of an electromagnet is given by $F = \frac{A_g B_g^2}{2\mu_0}$ (2.10) which, when applied to the air gap of the force rig, will cause a displacement of the tooth according to the permeability gradient, i.e. from iron into air. According to Wignall, *et al.* (1988) the total flux will leave the iron at right angles when the iron is unsaturated and it is assumed to have an infinite permeability. Under these ideal conditions then, the tangential component of the flux density is neglected when calculating the y-force according to (2.13) and (2.16).

The magnetic y-force, tending to elongate the tooth into the air gap, can be compared to the gravitational force associated with placing a known mass directly onto the area above the tooth, as both these forces result in y-direction tooth displacement. The gravitational force can be determined by multiplying the known mass by a factor of 9.81. Then, by substituting this force into (2.10), the corresponding flux density B that would cause an 'equivalent' magnetic force can be calculated by making B the subject of the formula – as the force is known and the original air gap dimensions and permeability of air remain

constant. Hence, by determining the corresponding values of B associated with the y-forces exerted by a range of known masses, tooth displacements caused by gravitational force can be compared to tooth displacements caused by 'equivalent' magnetic force. An example of this follows, where a known mass of 1kg is chosen, giving a gravitational force of 9.81N, and the cross-sectional area of the air gap for Design 3 is 0.00023m^2.

$$F = \frac{B^2 A}{2\mu_0} \quad \therefore \quad B = \sqrt{\frac{F \times 2\mu_0}{A}} = \sqrt{\frac{9.81 \times 0.000002513}{0.00023}} = 0.3274\text{T}$$

Hence, an air gap flux density of 0.3274T can be said to exert the same y-force on the tooth as 1kg of applied mass. The reason for making this comparison is that the elastic displacement of the tooth, when magnetised, is the result of two primary phenomena – namely, the Maxwell forces at the iron-air boundary, and magnetostriction of the core, as shown by Figure 3.31. On the other hand, the gravitational force exerted by placing a mass onto the area above the tooth will cause the C-core to constrict, and therefore the tooth to displace, but will induce no force at the iron-air boundary.

Although the total gravitational and magnetic forces have been made equal for this experiment, using (2.10), the magnetic force is effecting tooth structure changes which the gravitational force is not. This may well result in a difference in tooth displacement responses due to each respective force. Although the aim of this work is not to make a distinction between Maxwell forces and magnetostriction, the shape of this force rig allows for an experiment where tooth y-displacements caused by 'equated' magnetic and gravitational forces may be compared. This way it can be observed whether or not the elastic displacement associated with an applied magnetic force on the tooth is greater than tooth displacement due to core constriction, associated with applied gravitational force.

Finally, it is not expected that the displacement(s) of the tooth should be exactly as according to (2.10) as the force rig is not operating under idealised conditions, i.e. saturation is expected to occur before an air gap normal flux density of 1.009T is reached (according to oscilloscope readings), and the permeability of the iron is not infinite.

4.2.1.1 Description of experiment

Tests will be conducted measuring the displacement of the tooth when subjected to both gravitational and magnetic forces. Mass increments of 0.5kg are chosen, having the range 0 – 9.5kg, as this maximum exerts a gravitational force on the tooth of 93.195N which, according to (2.10), equates to a magnetic force in the air gap of flux density 1.009T.

A small block of mild steel, as seen in the photograph in Figure 3.30, is secured with steel putty to the area directly above the tooth of the force rig, matching the tooth dimensions in the x- and z- directions. This is done to ensure that the total force exerted by a mass placed onto the block will be applied exclusively to the area above the tooth. This is shown in Figure 4.8 where the concept for this experiment is illustrated.

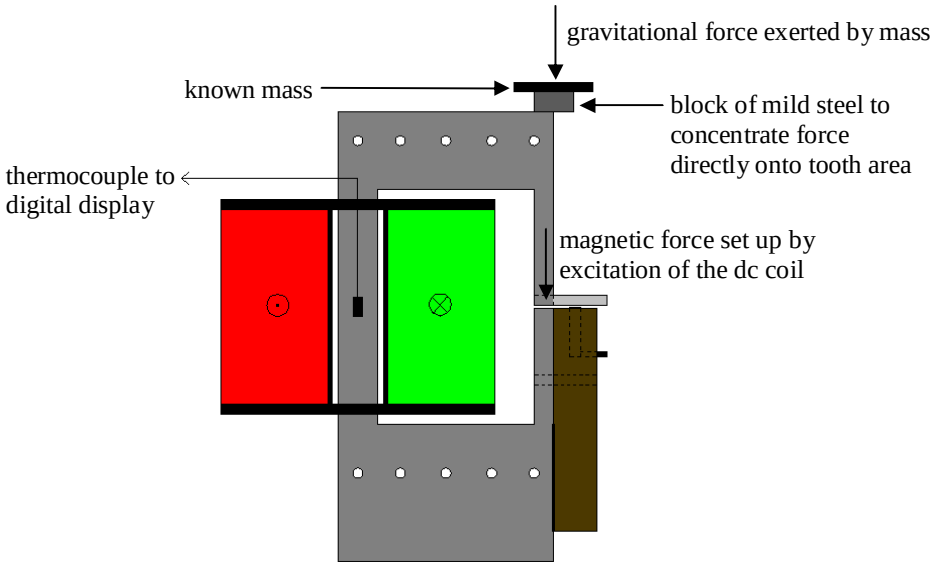

Fig. 4.8 Experiment 1: Concept

Five identical tests are carried out, for mass- and flux-induced force respectively, giving ten tests in total, in order to compare the results of each and observe repeatability. For each measurement, a constant temperature is maintained for the limb and (ambient) environment inside the box, the force is returned to zero before the next force is applied, the starting (zero force) voltage is noted (as the starting position changes slightly each time the force is removed) and the resultant (force applied) voltage is then referenced to the new starting (zero force) point in each case.

4.2.1.2 Results

All data measured by digital multimeter is tabulated and can be found in Appendices GA – GE, giving the results for y-displacement of the tooth as a function of the 'equivalent' gravitational and magnetic force applied for all ten tests, and is shown graphically in Figure 4.9. Here the dashed curves represent mass-induced displacement and the solid curves represent flux-induced displacement. The analogue voltage output signal for mass-induced displacement as a function of time, displayed by the oscilloscope, is shown in the screenshot in Figure 4.10, where the maximum of 9.5kg is placed onto the steel block above the tooth, left to rest for a short time, and then removed. The analogue voltage output signal for flux-induced displacement as a function of time, displayed by the oscilloscope, is shown in the screenshot in Figure 4.11, where the flux density is steadily raised from 0.011T (being the remanent flux density in the air gap) up to 1.009T and steadily returned again to 0.011T.

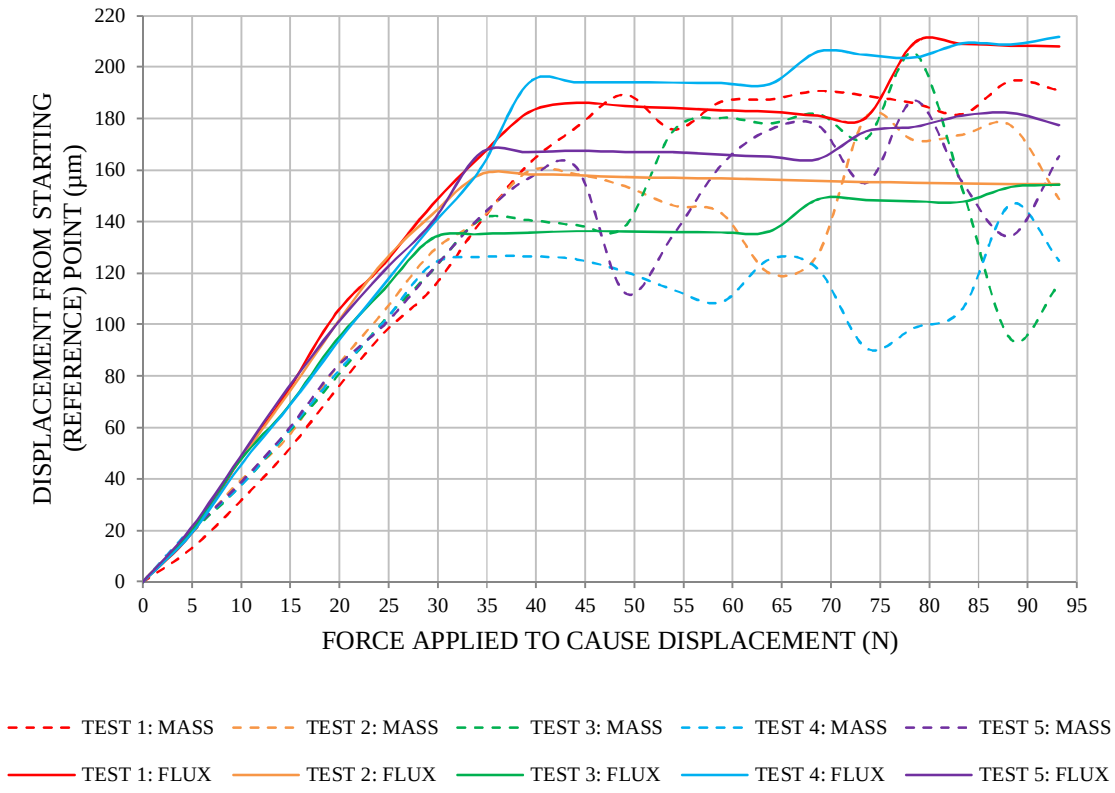

Fig. 4.9 Experiment 1: Measured tooth displacement results

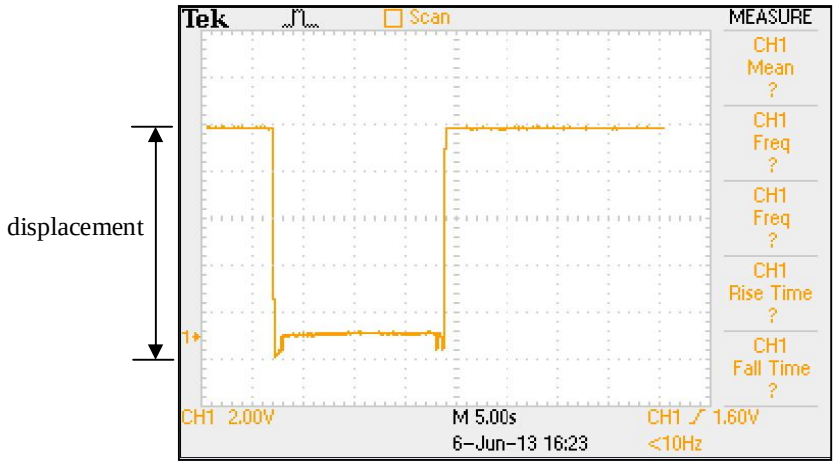

Fig. 4.10 Experiment 1: Oscilloscope screen shot for mass-induced displacement

Fig. 4.11 Experiment 1: Oscilloscope screen shot for flux-induced displacement

Although a difference is noted between the flux- and mass-induced displacement curves in this experiment, the displacement magnitudes associated with both types of force are, however, a lot more than predicted by Hooke's law, i.e. in the micrometer range. A measurement error of this nature was expected, attributed to the mechanical flexibility of the C-core due to its asymmetrical shape.

This is not the case in EMs, where the stator teeth are supported by the core back, which is a mechanically strong yoke, symmetrical at the radial centre position of each tooth. This means that the radial displacement of the stator teeth is not a result of any flexibility

caused by asymmetry in the core. Therefore, the next logical step would be to physically restrict the bending movement of the C-core, in an attempt to reduce its mechanical flexibility as much as possible. By doing this, the difference between elastic displacement of the tooth – caused by magnetic force – and tooth displacement caused only by core constriction – associated with gravitational force – may also become more evident.

4.2.2 Experiment 2

By inserting a non-ferrous metal bar – having a relatively high Young's modulus and machine-engineered to be slightly greater in y-direction length than the left limb – into the space between the coil and the tooth, the bending flexibility of the core would be, in an ideal sense, eliminated. The success of this idea depends on the bar being able to physically fit into the required space while being slightly oversized to provide mechanical support between the yoke and core base. Furthermore, once this is achieved, its effectiveness will depend on how accurately the bar is machined to the required dimensions, and also its elasticity modulus in relation to that of the core. The bar must be non-ferrous so as not to provide an alternative path for the magnetising flux required in the air gap. The concept for this experiment is illustrated in Figure 4.12.

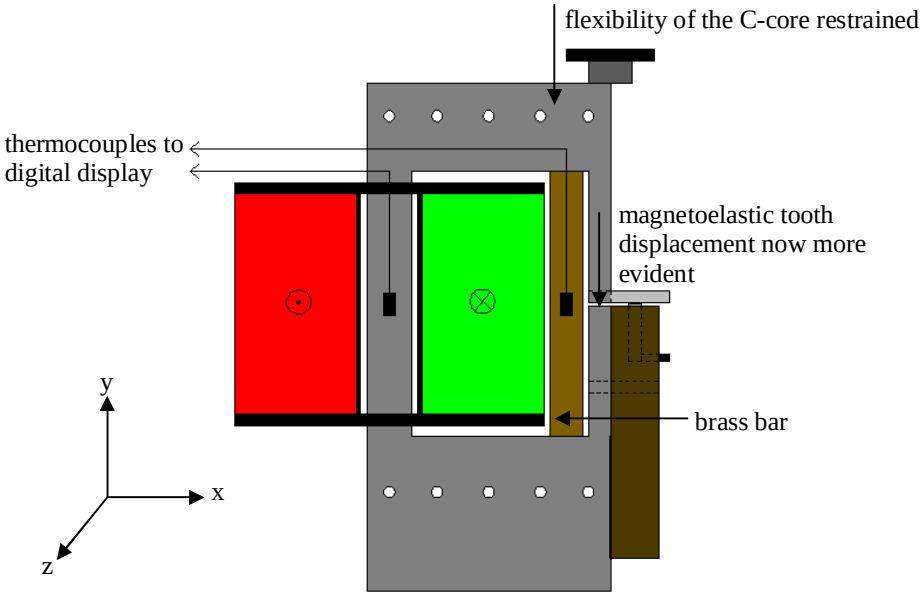

Fig. 4.12 Experiment 2: Concept

4.2.2.1 Description of experiment

The y-direction length of the space between the yoke and core base was measured with a micrometer. A bar made of brass was then machined to be 100μm greater in y-direction length than this measured space, being 16mm wide (x-direction) to fit between the coil and the tooth, and 23mm deep (z-direction) to span the core lamination stack length.

Among the available range of non-ferrous metals, brass was chosen for its superior Young's modulus of $102 - 125 \times 10^9$ Pa. This is less rigid than the M250-35A silicon steel of the force rig (185×10^9 Pa) but was the best available option. The brass bar was then wedged into position by knocking it with a hammer as gently as possible so as not to damage the bar or the laminated core. The glue bond between the target and the tooth was broken and reset once the bar was in position, according to the same procedure as followed previously, and the target was shown to be within measuring range once this bond had set.

In addition to monitoring the temperature of the limb during experiments, it is also necessary to monitor the temperature of the brass bar, as any y-direction flexing of this bar due to changes in temperature would affect the measurement air gap. A thermocouple is therefore also attached onto the brass bar.

It was found that a more stable earth was achieved by grounding the core of the force rig instead of the measurement target. This was done by means of a fork-lug making solid contact with the core, secured in place by one of the nylon bolts. This adjustment resulted in a considerable improvement in the measuring range of the sensor, by causing a noticeable reduction in voltage output at standstill (zero force) as well as a reduction in the amount of noise in the output signal.

A photograph of the force rig for Experiment 2 is shown in Figure 4.13, having all of the above mentioned alterations, with 3.5kg of mass applied to the steel block on the area directly above the tooth.

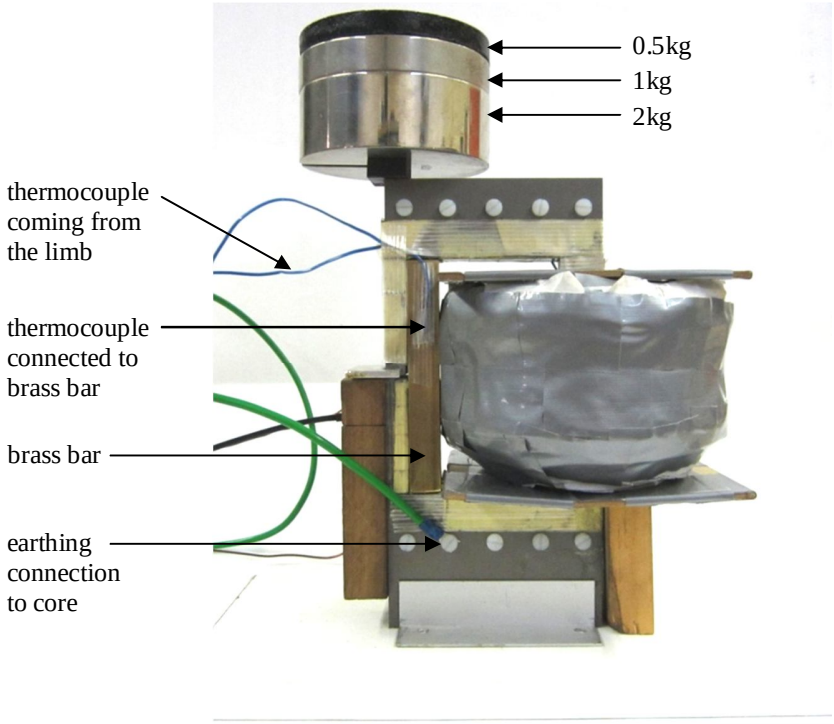

Fig. 4.13 Experiment 2: Photograph of force rig

The same ten tests are carried out as conducted in Experiment 1, in order that the results of the two experiments may be compared, and hence the effectiveness of the addition of the brass bar to the force rig will be shown. For each measurement, a constant temperature is maintained for the limb, brass bar and environment inside the box, the force is returned to zero before the next force is applied, the starting (zero force) voltage is noted and the resultant (force applied) voltage is then referenced to the new starting (zero force) point in each case.

4.2.2.2 Results

All data measured by digital multimeter is tabulated and can be found in Appendices HA – HE, giving the results for y-displacement of the tooth, as a function of the equivalent gravitational and magnetic force applied for all ten tests, and is shown graphically in Figure 4.14. The analogue voltage output signal for mass-induced displacement as a function of time, displayed by the oscilloscope, is shown in the screenshot in Figure 4.15, where the maximum of 9.5kg is placed onto the steel block above the tooth, left to rest for a short time, and then removed. The analogue voltage output signal for flux-induced

displacement as a function of time, displayed by the oscilloscope, is shown in the screenshot in Figure 4.16, where the flux density is steadily raised from 0.012T up to 1.009T and steadily returned again to 0.012T.

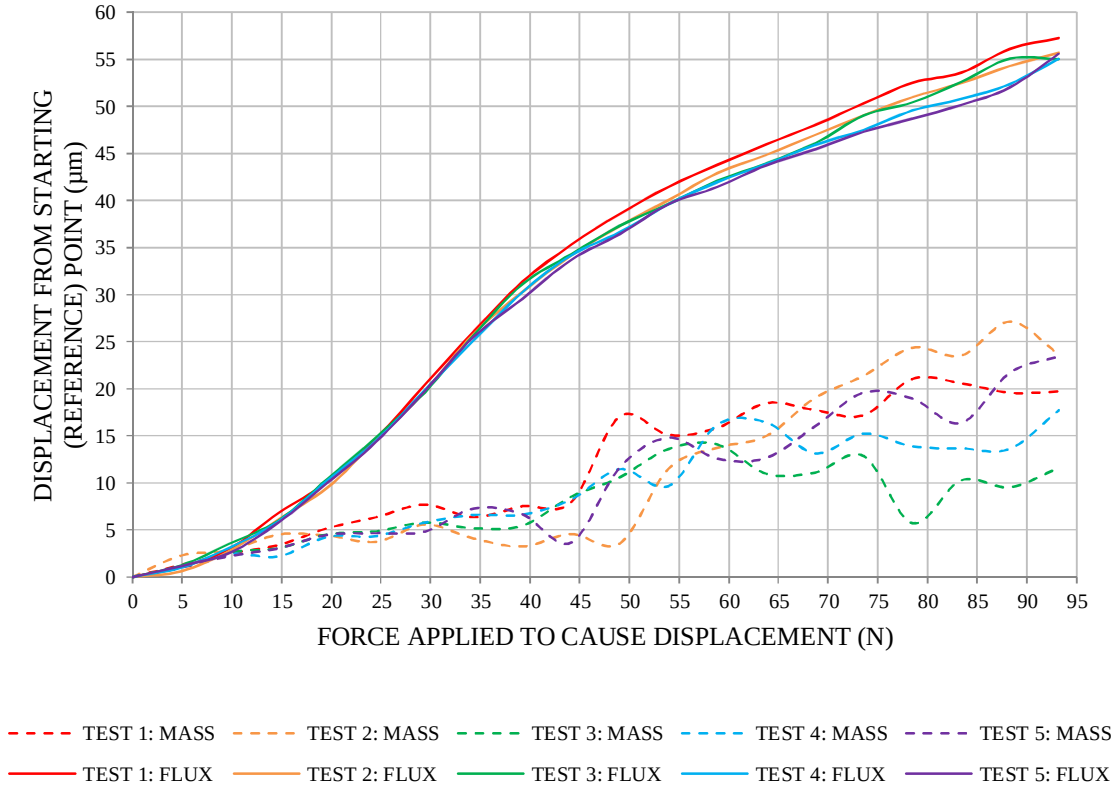

Fig. 4.14 Experiment 2: Measured tooth displacement results

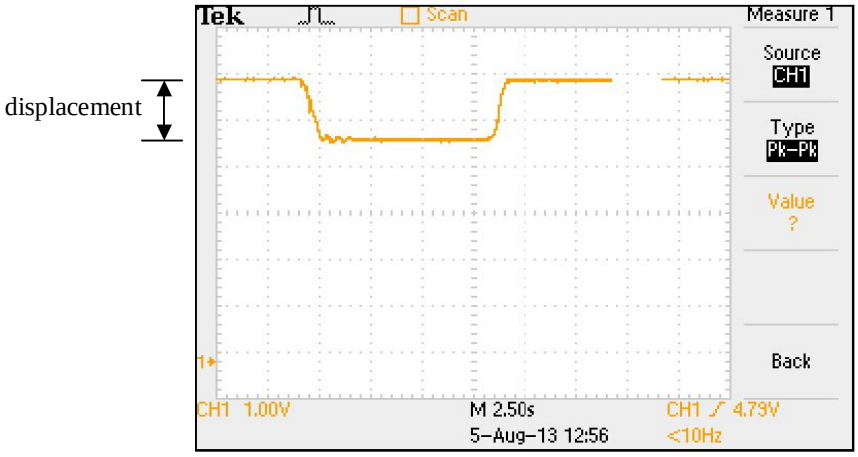

Fig. 4.15 Experiment 2: Oscilloscope screen shot for mass-induced displacement

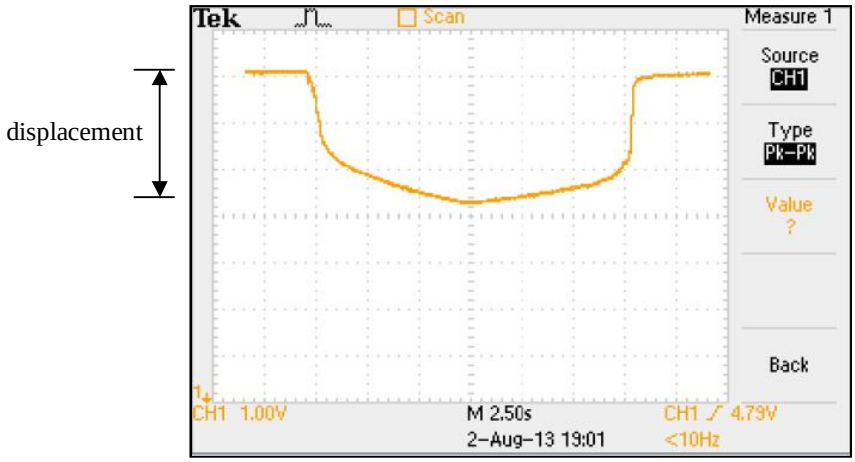

Fig. 4.16 Experiment 2: Oscilloscope screen shot for flux-induced displacement

4.2.3 Experiment 3

The final experiment is performed on force rig Design 4. The mechanical and magnetic symmetry of this design makes the conditions for this experiment more relevant to those of an EM. The major difference is that the forces being induced on the tooth of the force rig are a result of a magnetostatic field whereas those induced on the stator teeth of an EM result from a magnetodynamic field. Nevertheless, the experimental process has been refined, and should now arrive at a set of practical results giving some idea as to the magnetoelastic response of a silicon steel tooth due to magnetic y-force acting over an air gap. The concept for this experiment is illustrated in Figure 4.17.

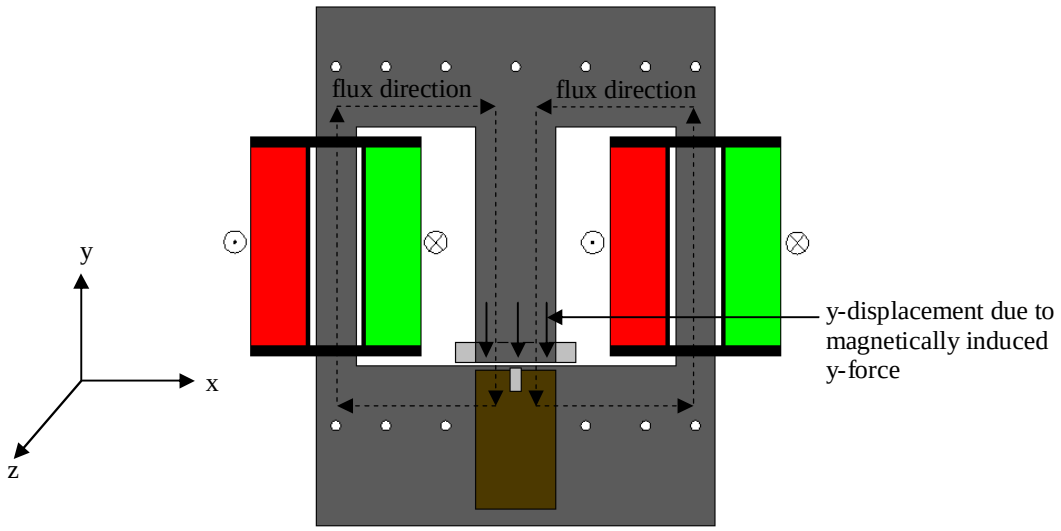

Fig. 4.17 Experiment 3: Concept

4.2.3.1 Description of experiment

Due to the mechanical stiffness and symmetry of the core it is expected that y-displacements of the tooth will now be in the order of nanometres, according to Hooke's law. For this experiment, tests are conducted using magnetic force only and not gravitational force. However, (2.10) is still used to determine the increments of y-force and corresponding air gap flux density applied for each measurement. This is done by equating 2kg increments of hypothetically applied mass (to the area above the tooth) to the relevant y-force and air gap normal flux density in each case. The resulting measurement increments can be seen in the tables of results found in Appendices IA – IJ.

It is now necessary to utilise the measurement system to its full potential, as the 2 nanometre resolution becomes essential in order to measure the displacements expected in this experiment. All possible measures have been taken to cancel out interference and measurement errors; these include:

- providing rigid positioning of the sensor by securing it to the core base,
- ensuring a very close measuring range between sensor and target (around 4V),
- constantly monitoring and regulating the temperature of the rig,
- incorporating the rig inside a box to isolate it from environmental temperature changes and electrostatic fields,
- resting the box on specially designed vibration-absorbing foam to isolate it from external vibrations, and
- providing a solid, double earth connection between the rig and the power supply to the controller, as seen in Figure 3.36.

However, after taking all these precautions, it was not possible to achieve a stable voltage output signal by the oscilloscope at the millivolt level, which exhibited around 20mV of noise, rendering any visual display of a change in voltage output meaningless. But the digital multimeter did manage to stabilise at 0.1mV, which is exactly the measurement resolution required. The digital multimeter is therefore the only output equipment utilised in this experiment.

Ten identical tests are carried out, for flux-induced force only, in order to compare the results of each and observe repeatability. As before, for each measurement, a constant temperature is maintained for both limbs and the environment inside the box, the force is returned to zero before the next force is applied, the starting (zero force) voltage is noted and the resultant (force applied) voltage is then referenced to the new starting (zero force) point in each case.

4.2.3.2 Results

All data measured by digital multimeter is tabulated and can be found in Appendices IA – IJ, giving the y-displacement results for the tooth for all ten tests. Figure 4.18 shows this displacement as a function of the applied magnetic force according to (2.10), Figure 4.19 shows this displacement as a function of the measured normal air gap flux density applied in each case, and Figure 4.20 shows this displacement as a function of the measured dc current applied in each case.

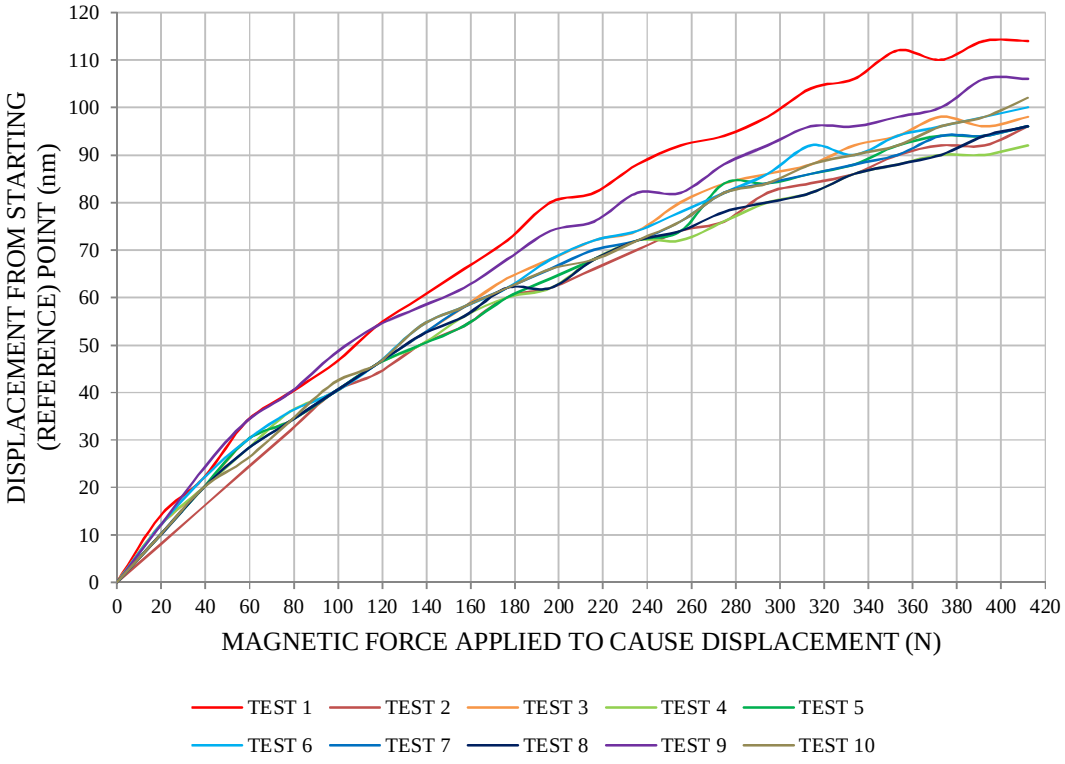

Fig. 4.18 Experiment 3: Measured tooth displacement as a function of force

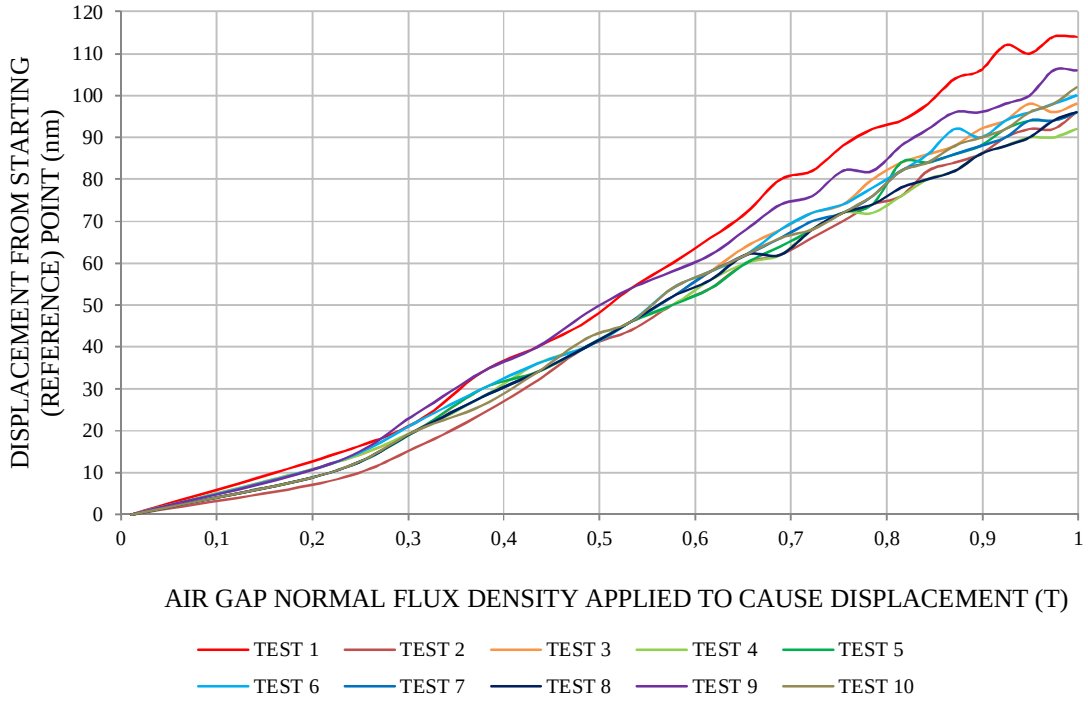

Fig. 4.19 Experiment 3: Measured tooth displacement as a function of flux density

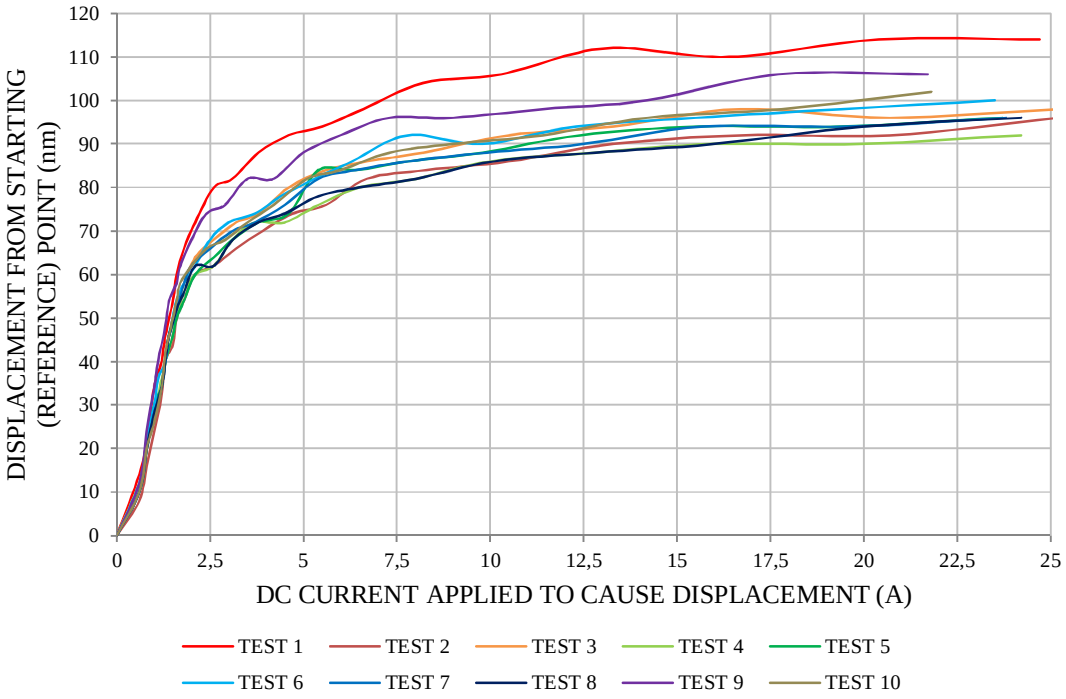

Fig. 4.20 Experiment 3: Measured tooth displacement as a function of dc excitation

Chapter 5

Analysis of results

5.1 Experiment 1

According to the digital multimeter results, shown in Appendices GA – GE, the starting voltage on each test shows that the measurement air gap was in the range 0.22 – 0.28mm (11 – 14V). This measurement range is clearly a deviation from the original intended air gap length of 0.04mm (2V) when the target was set into position, as discussed in Section 3.2.5, falling outside the maximum measuring range of 0.2mm (10V) of the sensor. This is attributed to the mechanical flexibility of the asymmetrical C-core, causing the relative position of the sensor and target to deviate over time. In addition, as the only option to ground the aluminium target was by using a crocodile clip, an inferior earth connection was achieved when compared with the next two experiments. However, this measurement range is not considered a problem, as the sensor is still clearly operational over the full range, and this is only the first step in a process where the experimental conditions are being refined. The observations in Table 5.1 are made with reference to Figure 4.9.

Table 5.1 Observation of results for Experiment 1

TEST	TYPE OF FORCE APPLIED TO TOOTH	END OF LINEAR REGION: X-AXIS (N)	END OF LINEAR REGION: Y-AXIS (μm)
1	GRAVITATIONAL	47	190
	MAGNETIC	40	185
2	GRAVITATIONAL	40	160
	MAGNETIC	35	160
3	GRAVITATIONAL	35	142
	MAGNETIC	30	135
4	GRAVITATIONAL	30	125
	MAGNETIC	40	195
5	GRAVITATIONAL	43	163
	MAGNETIC	35	168

By referencing Figure 4.9 it can be seen that, for all ten tests, the tooth displacement response for both magnetic force and gravitational force is fairly linear up to a certain point, after which the five flux-displacement curves tend to 'plateau' and the five mass-displacement curves tend to become 'erratic'. By referencing Table 5.1 it can be seen that the force at which this linear region ends is similar for both flux- and mass-induced displacement curves, in all five cases respectively, with the displacement at which this occurs being very close in four out of five cases. This linear region therefore applies to the displacement curves of both types of applied force and becomes the range of interest, as it is clear that the range beyond this point yields little to no meaningful results.

Over the linear region it can be clearly seen, for all ten tests, that the displacement associated with magnetic force is almost consistently greater than the displacement associated with gravitational force. Figure 5.1 shows a graph where the mass-induced displacement is subtracted from the flux-induced displacement for the five respective tests, giving the difference in displacement between the two types of applied force. On the x-axis, this is shown over the range of applied force up to 50N, in order to represent the linear region only. On the y-axis, the positive area (above zero) represents the region where flux-induced displacement is greater than mass-induced displacement.

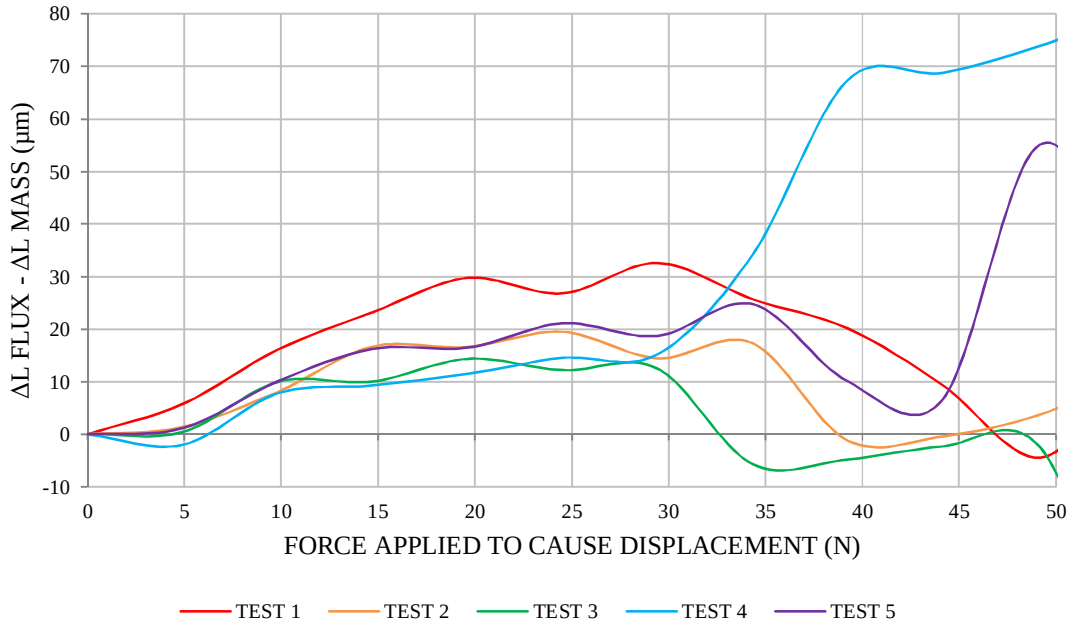

Fig. 5.1 Experiment 1: Difference in tooth displacement for flux- and mass-induced force

The results of this experiment show that the elastic tooth displacement due to magnetic force was generally greater than the tooth displacement caused by constriction of the core, due to gravitational force, where these forces were made equal according to (2.10), and each applied to the tooth, respectively. With reference made once again to Figure 4.9, the reason for the nonlinearity of the displacement curves after approximately 30 - 50N of applied force is considered to be due to the bending of the C-core introducing a tilting angle between the sensor and target. This angle would increase in proportion to the amount of force applied, eventually causing the target to make contact with the edge of the sensor at some point before the full measuring range has been reached. After this point any linearity in displacement response cannot be expected, unless consistently zero.

This is supported by the oscilloscope screen shots in Figures 4.10 and 4.11. As shown in the bottom left corner of the screen shot, each vertical division of the scope panel has a value of 2V. Here it can be seen that in both cases the displacement reaches a maximum of between 9 – 10V. This indicates that, as the core bends, the angle of tilt increases between target and sensor until contact is made, causing the peak in voltage change to be close to but less than the full measuring range in each case. This would explain why the end of the linear region is so similar for both types of force applied, as the tooth displacement is limited by this phenomenon in both cases. However, it does not explain the difference in mass- and flux-induced displacement curves beyond this point.

When flux-induced force is considered, the setting in of saturation, before the maximum flux density in the air gap is reached, may play a role. It has been noted by Binns, *et al.* (1972) and Garrigan, *et al.* (1999) that the magnetic force reaches a peak at saturation and does not increase indefinitely with excitation. This may help to explain the ‘plateau’ characteristic exhibited by all five flux-induced displacement curves.

When mass-induced force is considered, the tilting angle plays a more prominent role. In addition to the aforementioned tilting angle occurring in the x-y-plane, the target may also be experiencing a (sideways) tilting angle in the z-plane. This is due to the fact that the core is made up of individual laminations, bolted together at the yoke and core base, allowing a very small amount (micrometers) of movement with respect to one another.

As the placement of each mass on the area above the tooth is not replicated with perfect precision for every measurement, the centre of gravity of each new mass shifts by degrees from one measurement to the next. This may cause some laminations on one side of the tooth to experience a greater displacement than some laminations on the other side of the tooth. As the measurement target is fixed to both sides of the tooth, this would have the effect of creating a tilting angle in the z-plane as well as the x-y-plane, meaning that the target can make contact with the edge of the sensor in all three dimensions. This would introduce an additional measurement error, and would help to explain the erratic nature of all five mass-induced displacement curves beyond the linear region.

5.2 Experiment 2

According to the digital multimeter results, shown in Appendices HA – HE, the starting voltage on each test shows that the measured air gap was in the range 0.1 – 0.17mm (5 – 8.5V). This measurement range is still a deviation from the original intended air gap length of 0.04mm (2V) when the target was set into position, but falls within the maximum measuring range of 0.2mm (10V) of the sensor. This improvement is attributed to the rigidity provided by the brass bar and the more stable earth connection.

Now that the brass bar has restrained the flexibility of the C-core, some interesting observations are made. By referencing Figures 4.9 and 4.14, it can clearly be seen that the displacement magnitudes are significantly less for Experiment 2 when compared to Experiment 1, for both mass- and flux-induced force. However, these displacements are still in the micrometer range, which is attributed to the shortfalls attached to the brass bar, i.e. having an inferior Young's modulus, and the fact that since it was able to fit into the required space it may have allowed a small micro-range of movement for the laminations.

Here the tooth displacement response due to magnetic force remains relatively linear over the full range of applied force, and consistently greater than that due to gravitational force, over the five respective tests. Once again, the tooth displacement response due to gravitational force exhibited a region of some linearity, falling between 0 – 50N, after

which the five associated curves become ‘erratic’ in nature. This again was not the case for the flux-induced displacement curves, and therefore a conclusion is reached that the z-plane tilting angle associated with the mass-induced displacement is indeed the reason for the difference displayed between these two types of curves. Furthermore, the physical restraint of the C-core does not allow the target to span the full measurement range (the maximum for flux-induced displacement is under 60µm) and therefore it does not make contact with the sensor. Here the displacement response due to magnetic force does not reach a ‘plateau’ point, even though the same excitation is applied in both experiments, and no erratic behaviour is exhibited. This suggests that, in Experiment 1, this response was due only to the target making contact with the sensor and is not linked to saturation.

Once again, a graph is shown in Figure 5.2, where the mass-induced displacement is subtracted from the flux-induced displacement for the five respective tests, giving the difference in displacement between the two types of applied force. This is shown over the range of applied force up to 50N on the x-axis (representing the ‘linear region’ for mass-induced displacement), and the positive area (above zero) of the y-axis represents the region where flux-induced displacement is greater than mass-induced displacement.

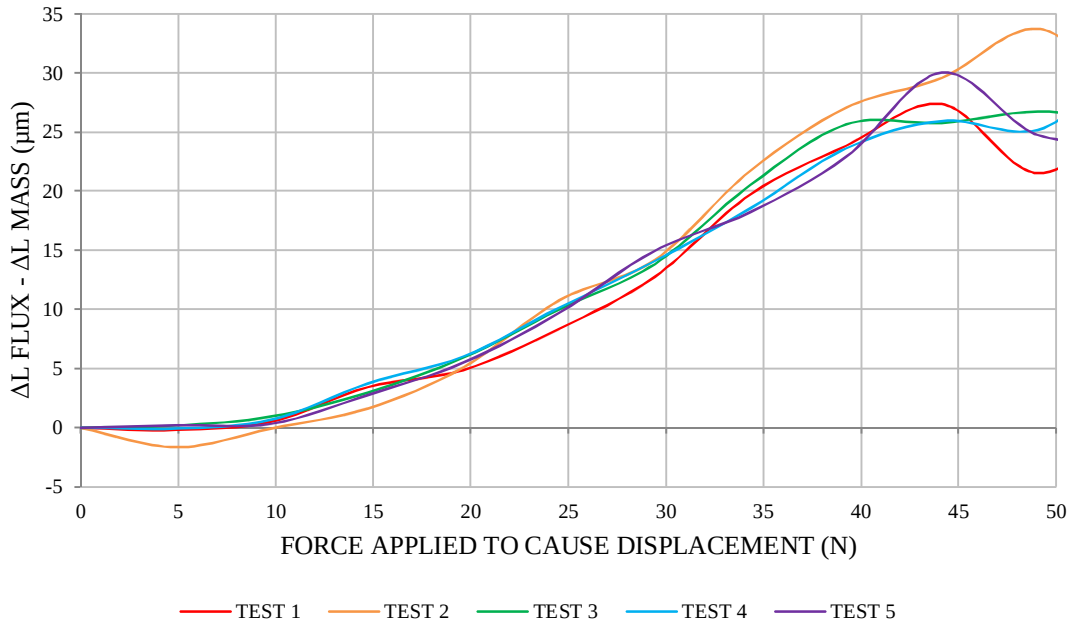

Fig. 5.2 Experiment 2: Difference in tooth displacement for flux- and mass-induced force

5.3 Experiment 3

According to the digital multimeter results, shown in Appendices IA – IJ, the starting voltage on each test shows that the measurement air gap was in the range 0.085 – 0.086mm (4.262 – 4.315V). Although this measurement range is still a deviation from the original intended air gap length of 0.04mm (2V), this is the closest to desired range achieved thus far. This is attributed to the mechanical rigidity of the core shape and that there are now two solid earth connections to the core, as shown in Figure 3.36.

By referencing Figure 4.18, it can be seen that the tooth displacement response due to magnetic force, for all ten tests, remains relatively linear over the full range of applied force. The most significant difference from this experiment to the previous experiments is the fact that the tooth displacement is now in the order of nanometres, which was expected. Now that this has been achieved, it is possible to compare the measured tooth displacement results with those predicted by Hooke's law, according to (2.6), over the same range of applied magnetic force. This is shown in the graph in Figure 5.3.

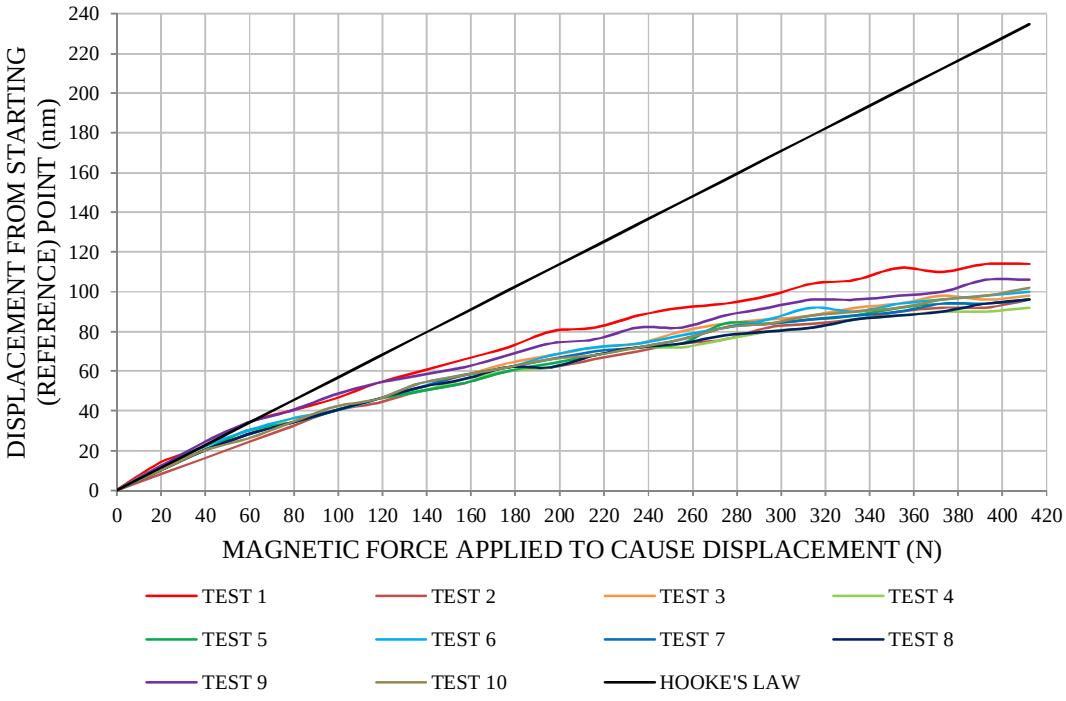

Fig. 5.3 Experiment 3: Comparison between measured displacement and Hooke's law

With regard to the Young's Modulus used in the calculation of Hooke's law, the rolling direction for the laminations used in force rig Design 4 was inspected and found to be in the x-direction. This is perpendicular to the y-displacement of the tooth and it was therefore necessary to apply the transverse direction (TD) value of the Young's Modulus, being 200×10^9 N/m^2, found in Table 3.1 and Appendix B. The calculation of Hooke's law is therefore considered to be correct, and this is supported by the first portion of the graph where the measured and predicted curves are in agreement. Now what remains is to consider what may have caused the drift in the measured displacement response.

The first consideration regarding the deviation between the measured and predicted results is that Hooke's law does not take magnetic saturation of the silicon steel into account. By referencing Figure 4.20, the nonlinear displacement response as a function of applied dc excitation can be seen, where saturation appears to set in somewhere between 60 – 80nm of displacement, at approximately 2.5A of excitation. This can be compared to the air gap normal flux density response to the applied dc excitation, shown in Figure 5.4. Here the knee-point is shown to be closer to 2A dc, with the associated air gap normal flux density shown to be in the region of 0.65T.

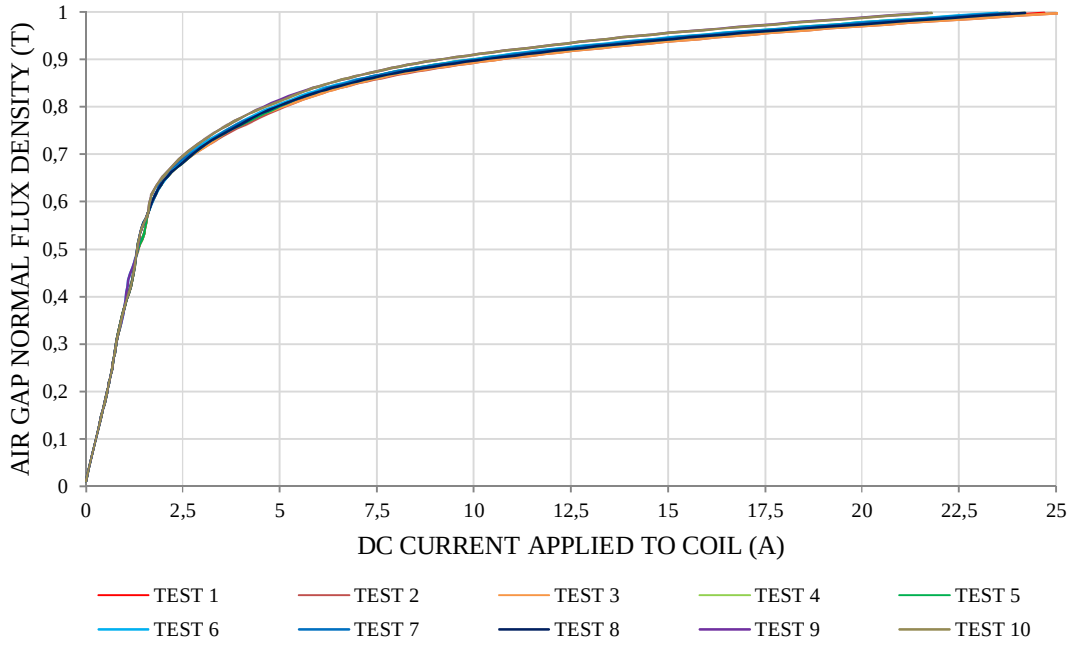

Fig. 5.4 Experiment 3: Nonlinear air gap flux density response to dc excitation

By referencing Figure 5.3 it can be seen that the curves associated with measured displacement and that of Hooke's law remain relatively close until approximately 60N of applied force. According to (2.10), this force equates to an air gap normal flux density of

$$B = \sqrt{\frac{F \times 2\mu_0}{A}} = \sqrt{\frac{60 \times 0.000002513}{0.00104}} = 0.38T$$

This is significantly less than the knee-point of 0.65T according to Figure 5.4, indicating that, although saturation of the silicon steel is considered to play a role in the deviation of these curves, it is not the only contributing factor.

The second consideration is temperature drift, which would cause measurement errors due to heat-flexing of the core. Although precautions have been taken to monitor and regulate the temperature of the core and the ambient environment inside the isolation box, this still remains a possibility. As the dc excitation to the coils is increased for each measurement until the full range of applied magnetic force has been reached, a direct proportion in temperature rise is applied to the limbs around which the coils are wound.

Even if the core is cooled back down to starting temperature for each measurement, and the measured displacement is relative to a measured starting (reference) point in each case, the fact that the limbs are subjected to an increased heat at every incremental step of the measurement process, for between 5 – 10s each time, means that it is likely that the limbs would experience some heat-flexing during this time period. This would result in y-direction elongation of the limbs, increasing at each measurement increment in direct proportion to applied dc excitation, thereby widening the air gap and diminishing the measured value of y-displacement of the tooth into the air gap.

Both of the above mentioned considerations are thought to be responsible for the drifting of the measured displacement curves from that associated with Hooke's law. To finish this study, the force rig used in this experiment is modelled and simulated on the 2D FE software. This is done for three reasons. First, to simulate the nodal force vectors acting in and around the air gap, whereby the distribution of local forces in this region may be

seen. Second, to reproduce the values of air gap normal flux density used in this experiment in the air gap of the simulated model, whereby the associated magnitudes of simulated y-force acting on the tooth can be compared to the y-force physically applied to the tooth in the experiment. And third, to investigate the difference in required dc excitation for the simulated and physical rig in order to produce the air gap flux density.

5.3.1 FE simulation of force rig Design 4

5.3.1.1 Force vectors

In order to model the nodal force vectors in and around the air gap of force rig Design 4, the first step is to increase the discretisation of the mesh in this region, meaning that a higher number of elements is specified. This improves the accuracy of the results when looking at the local force distribution and will also assist in the calculation of the global y-force acting on the tooth tip. The latter is calculated according to (2.16), where, according to Maxwell, a path is defined through air that completely encloses the body on which the force is acting. As seen in Figure 5.5, this is not possible, and after discussions with industry, it has been agreed sufficient to determine the integral of the y-force along the path as shown below.

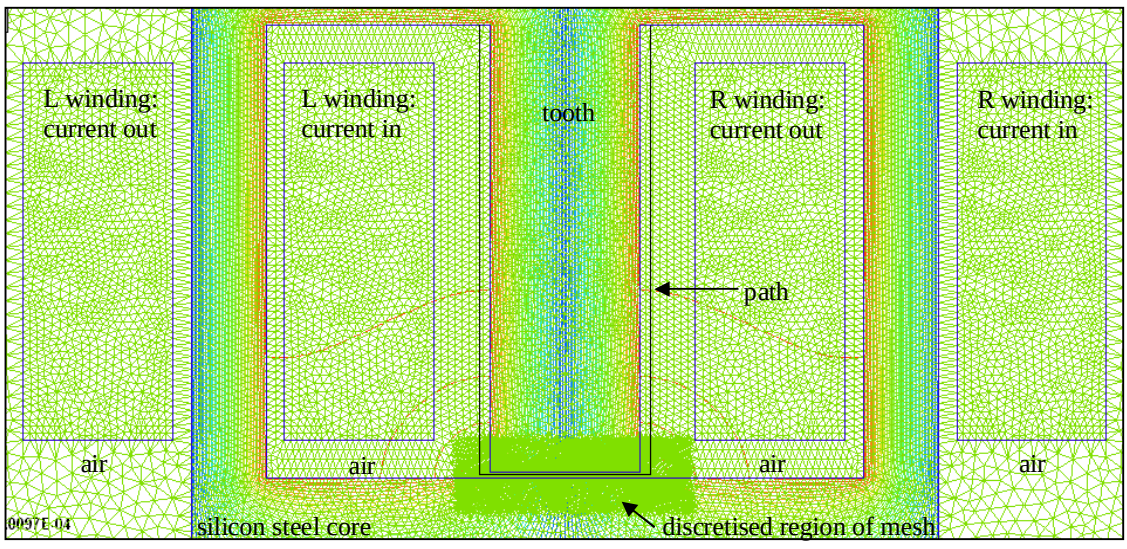

Fig. 5.5 Path defined around the tooth of force rig Design 4

A close-up portion of the discretised region of the mesh is shown in Figure 5.6 and the distribution of local forces in and around the air gap is shown in Figure 5.7.

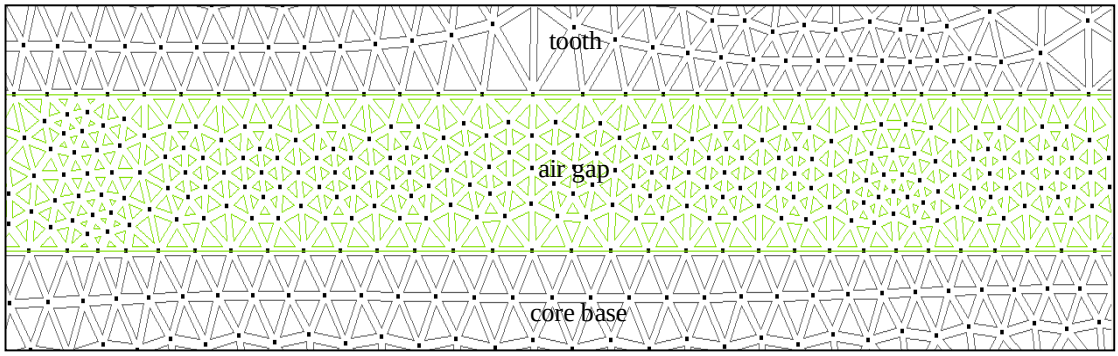

Fig. 5.6 Discretisation of mesh around the air gap of force rig Design 4

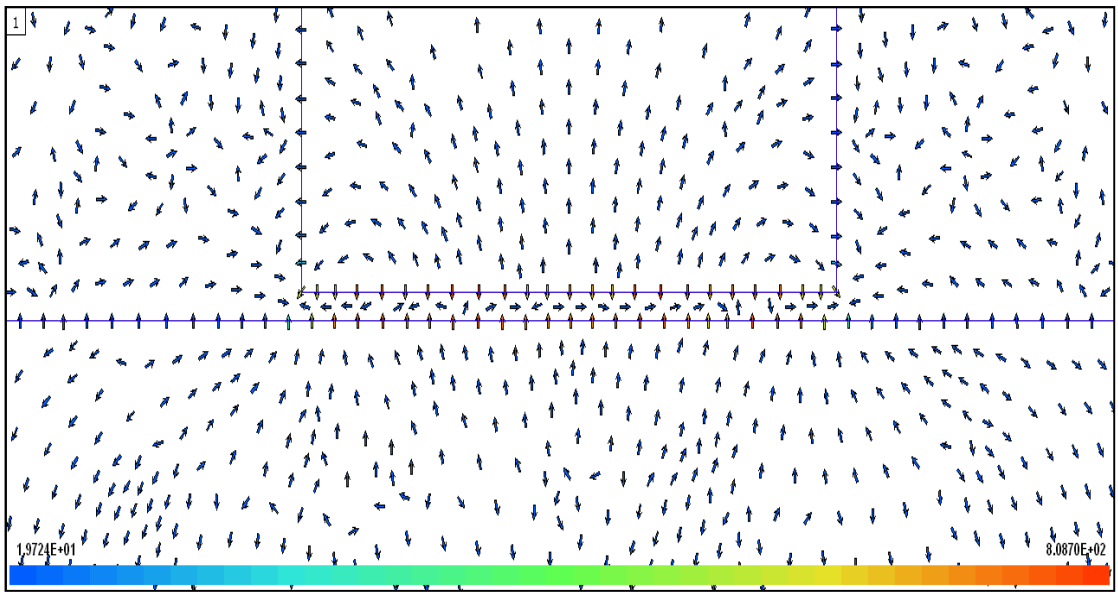

Fig. 5.7 Force vectors around the air gap of force rig Design 4

By looking at the colour shading of the vectors in Figure 5.7 it can be seen that, according to the MST method used by the FE software, the greatest magnitude of force is at the iron-air boundaries between the tooth tip and air gap, and the core base and air gap, respectively. Here it can be seen that the force is acting to try and close the air gap, in an attempt to minimise the reluctance of the magnetic circuit. It is interesting to keep in mind that the force vectors are acting from regions of high permeability to regions of low permeability, which can also be seen at the iron-air boundaries at the sides of the tooth.

5.3.1.2 Comparison of measured and simulated tooth y-forces

By reproducing the values of measured air gap normal flux density used in this experiment in the air gap of the simulated model, the associated y-forces acting on the tooth of the simulated model can be compared to the y-forces applied to the tooth of the physical rig. This comparison is shown in Table 5.2. Here the values of physically applied y-force used in the experiment – shown in the second column – are compared against the integral values of the y-force along the defined path – shown in the fourth column – and the values of y-force confined to the air gap – shown in the sixth column.

Table 5.2 Simulated forces for Experiment 3

MEASURED AND SIMULATED AIR GAP FLUX DENSITY (T)	Y-FORCE APPLIED TO TOOTH IN PHYSICAL TESTS (N)	SIMULATED Y-FORCE ALONG DEFINED PATH (N/m)	Y-FORCE CONVERSION DUE TO DIFFERENCE IN DEPTH (N)	PEAK VALUE OF SIMULATED Y-STRESS IN AIR GAP (N/m^2)	Y-FORCE IN THE AIR GAP DERIVED FROM STRESS (N)
0	0	0	0	0	0
0.218	19.62	791.01	20.566	18971.6	19.73
0.308	39.24	1579.3	41.062	37868.9	39.384
0.377	58.86	2366.6	61.532	56750.9	59.021
0.435	78.48	3150.2	81.905	75542	78.564
0.486	98.1	3934.6	102.3	94274.1	98.045
0.533	117.72	4731.2	123.011	113369	117.904
0.576	137.34	5522.9	143.595	133933	139.29
0.616	156.96	6319	164.294	151451	157.509
0.653	176.58	7100.8	184.621	170187	176.994
0.689	196.2	7905.4	205.54	189415	196.992
0.722	215.82	8685.2	225.815	208016	216.337
0.754	235.44	9465.4	246.1	226849	235.923
0.785	255.06	10258	266.708	245862	255.696
0.815	274.68	11065	287.69	265039	275.641
0.843	294.3	11841	307.866	283606	294.95
0.871	313.92	12639	328.614	302778	314.889
0.898	333.54	13433	349.258	321767	334.638
0.924	353.16	14205	369.33	340665	354.292
0.949	372.78	15002	390.052	359369	373.744
0.974	392.4	15797	410.722	378519	393.66
0.998	412.02	16571	430.846	397380	413.275

The integral of the y-force along the path as defined in Figure 5.5, shown in column 3, is given in N/m, which indicates the 1m depth of the FE model. Therefore, in order to compare the simulated y-force with the physically applied y-force in the experiment, the simulated results are divided by 1000 (1m) and multiplied by 26 (mm) in order to achieve the stack length of the force rig, with results shown in column 4.

By comparing column 2 and column 4, it can be seen that the simulated global y-force in each case is slightly higher than the physically applied y-force, which is due to the fact that the physically applied y-force only takes into account the air gap, according to (2.10), and the simulated y-force is the integral of all the y-forces along the path 'enclosing' the tooth. Therefore, the y-force in column 4 is expected to be greater than the y-force in column 2.

One way of obtaining the force confined to the air gap is by taking the peak value of air gap y-stress, shown in column 5, multiplying it by 0.04 (40mm width of the tooth) to obtain air gap y-force, and performing the same depth conversion as above. This results in the values for air gap y-force shown in column 6, which are seen to agree closely to the physically applied y-force in column 2.

5.3.1.3 Comparison of measured and simulated dc excitation

Although the dc excitation conditions have improved throughout the force rig design process, incongruency still exists between the measured and simulated results, necessitating further investigation.

Table 5.3 shows a comparison between the measured and simulated dc excitation supplied to the coils in order to achieve the required air gap normal flux density for each measurement increment. The values of measured current shown in the table are the averaged measured currents over the ten tests. The measured values are according to the dc power supply and therefore need to be halved (the measured resistances of the two coils being relatively equal) as the coils are split in parallel. These values are then compared to the simulated current supplied to each coil in the FE model.

Table 5.3 Comparison of measured and simulated dc excitation

AIR GAP NORMAL FLUX DENSITY (T)	AVERAGE OF MEASURED CURRENT IN EACH COIL (A)	SIMULATED CURRENT IN EACH COIL (A)	PERCENTAGE DIFFERENCE (%)
0.218	0.3	0.2756	8.134
0.308	0.4	0.3857	3.575
0.377	0.5	0.4701	5.98
0.435	0.59	0.541	8.305
0.486	0.65	0.6034	7.169
0.533	0.72	0.661	8.195
0.576	0.8	0.71395	10.756
0.616	0.89	0.7632	14.247
0.653	1.035	0.8089	21.845
0.689	1.27	0.8534	32.803
0.722	1.535	0.8945	41.726
0.754	1.86	0.93444	49.761
0.785	2.24	0.9733	56.549
0.815	2.685	1.01124	62.337
0.843	3.205	1.04695	67.334
0.871	3.935	1.08295	72.479
0.898	4.945	1.1179	77.393
0.924	6.265	1.15212	81.611
0.949	7.85	1.18575	84.895
0.974	9.785	1.22007	87.531
0.998	11.9	1.25412	89.461

Here it can be seen that the measured and simulated dc excitation supplied to the coils is, in fact, rather close at the lower end of the scale. The disparity between them escalates as the excitation approaches the knee point of 0.65T, after which it increases more dramatically as the excitation is increased toward maximum. This suggests that saturation of the physical rig is playing a prominent role, but the question of where this saturation is occurring still remains, as it is most unlikely that the tooth is saturated when the air gap flux density is only around 1T. The saturation is then most likely occurring in the limbs.

In order to gain more clarity on this issue, industry was consulted to design a 3D FE model for force rig Design 4. This was done, giving the 3D model a stack length (z-axis) of 26mm, and placing it in the centre of a $2m^3$ region of air, in order to include all leakage flux. According to this model, the current required in each coil increased from 1.254A (2D) to 8.8A (3D), in order to achieve 0.998T in the air gap, resulting in saturation of the wound limbs. The 3D model is shown in Figure 5.8, with core flux density included, where, for simplicity, only one quarter of the model is shown.

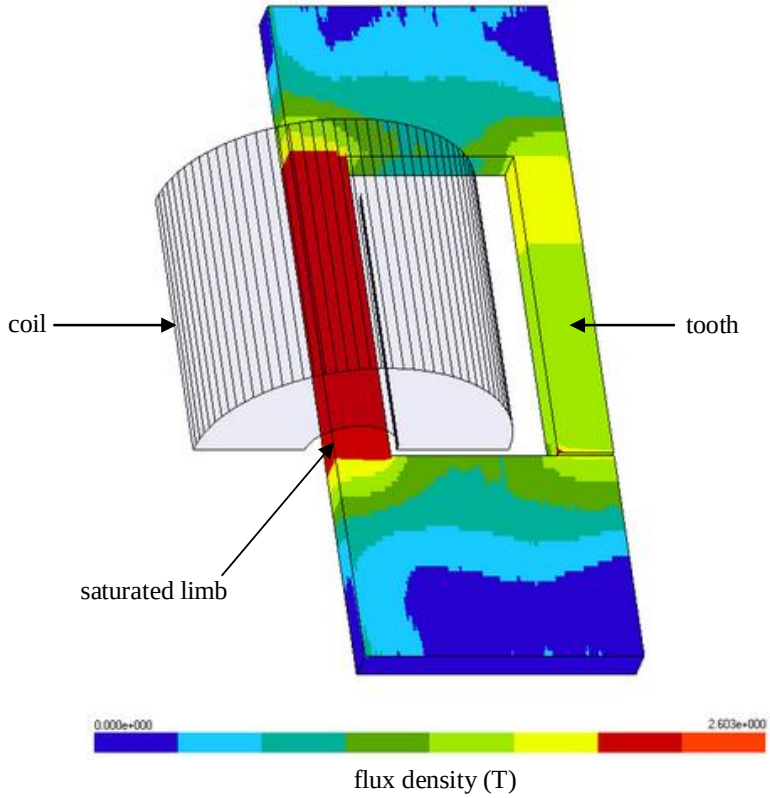

Fig. 5.8 3D FE model of force rig Design 4 showing core flux density

Here, it can clearly be seen that it is the limb(s), and not the tooth, that is saturating. The reason for this is considered to be due to the fact that the limbs carry all the magnetising and core leakage flux, including the leakage in the z-direction, which has yet to be determined. This saturation, together with core leakage and leakage from the large coils, would explain the increasing amount of current required to achieve the air gap flux density at the higher end of the scale. The reason for the 3D simulated excitation (8.8A) being lower than the measured excitation (11.9A) may be due to differences in the real and extrapolated B-H curves in the region of saturation.

In order to see what effect the z-directed leakage flux has on the excitation, the same 3D model was simulated, but this time having no region of air in the z-direction beyond the thickness of the core, i.e. a boundary line of zero potential at z = 13mm and z = -13mm from the z-direction symmetry (centre) line. This model, which shall be called the 'pseudo-2D model', having no z-directed leakage flux, achieved 0.998T in the air gap by

exciting the coil with 1.254A dc. This is exactly the same excitation as in the actual 2D model and shows that leakage flux in the z-direction is playing a very significant role.

In order to gain some idea as to the magnitude of the z-directed leakage flux, a final simulation was done on the pseudo-2D model and the 3D model, both having a core relative permeability μ_r of 5000 and dc excitation of 1.254A. The value of the former was taken as EM laminations usually have $3500 < \mu_r < 5000$ and this experiment is relative to EMs, where the greatest concentration of energy is in the air gap (including the iron-air boundaries at which the forces are acting). In order to guarantee this in the model, a high μ_r in the core means that the reluctance $\Re$ and magnetising force H in the core will be low. As the flux density B in the core and in the air gap is usually assumed to be the same, and $\Re$ and H in the air gap is, by comparison to the core, very high, the magnetic energy will therefore be concentrated in the air gap, as energy is a function of B and H.

The magnetic stored energy in both models was then (theoretically) divided up into two parts – namely, core and air, with the energy in the air including those regions occupied by the coils. For the 3D model, the air was additionally subdivided into two z-directed regions – namely, Region 1, having the thickness of the core ($-13\text{mm} < z < 13\text{mm}$) and Region 2, being the 'leakage region' ($-13\text{mm} > z > 13\text{mm}$). By setting the total for magnetic stored energy for the pseudo-2D model at 100% it becomes possible to see the additional magnetic energy stored in air in the z-direction of the 3D model by comparison. The results are shown in Table 5.4, where it can be seen that the amount of energy in the z-directed 'leakage region' of the 3D model causes its total magnetic stored energy in air to be approximately 40% greater than that in the pseudo-2D model.

Table 5.4 Magnetic stored energy in specified regions of Design 4

REGION WHERE ENERGY IS STORED	PSEUDO-2D MODEL	3D MODEL		
		REGION 1	REGION 2	TOTAL
CORE	5.4%	10.1%	-	10.1%
AIR	94.6%	92%	43.8%	135.8%
TOTAL	100%	102.1%	43.8%	145.9%

Chapter 6

Conclusions and recommendations

The goal of this thesis was the measurement of y-direction elastic displacement of a silicon steel tooth caused by electromagnetically induced force. This tooth formed part of a rig, designed in such a way as to emulate the conditions in an EM, and built in order to simplify the measurement conditions in this practical investigation. The capacitive displacement measurement technique was chosen for its high nanometre resolution, imperviousness to magnetic fields and affordability, and tooth displacements on the nanometre scale were successfully measured.

A number of force rigs were designed and constructed with the aim of producing an air gap normal flux density of 1T by dc coil excitation. This was eventually achieved through a process of error elimination, resulting in two force rigs being used for experiments. The experimental process – as the force rig design process – was refined, until measured displacement results were achieved that were comparable to a well-known formula predicting the force-induced displacement of linear elastic materials.

However, measurement errors were present in the first two experiments due mainly to the force rig geometry, and in the third experiment due mainly to magnetic saturation and heating effects of the excitation. Nevertheless, in the first two experiments an interesting comparison was made between tooth displacements caused by respective gravitational and magnetic forces. And finally, the outcome of the third experiment showed relatively close agreement between measured and predicted results up to a point, after which a deviation occurred in the measured results, which has been explained.

It is put forward for consideration that a starting point has been established for further investigation into the measurement of electromagnetic force-induced displacement of stator teeth in EMs. A summary of the important findings of this work and some ideas for future research are discussed in the following sections.

6.1 Summary of findings

Capacitive displacement measurement has been shown to be a good choice of measuring technique for non-contact, static, electromagnetic force-induced displacement applications. However, there are some important lessons that have been learned, being:

- an isolated environment helps to reduce measurement errors,
- mounting the sensor in a suitable and stable position in relation to the measurement target is absolutely necessary but very difficult,
- the measurement target must be a flat, very smooth (polished) surface,
- earthing of the measurement target greatly affects the measurement range, and
- powerful data acquisition equipment is required when measuring at the nano-range as a clear measurement output signal can be difficult to achieve.

The first three points mentioned above are considered to present problems in as far as the future implementation of this measuring technique in EMs is concerned.

Although the mechanical flexibility associated with the asymmetrical shape of force rig Design 3 does not exist in EMs, experiments on this force rig allowed for an observation to be made. In Experiment 1 it was shown that when a gravitational and magnetic force are equated, using (2.10), and both applied, respectively, to a magnetic body – in the same direction and over the same area – the elastic displacement of the body resulting from the magnetic force is generally greater than the displacement of the body resulting from the gravitational force. In Experiment 2, the flexibility of the C-core was physically restrained in an attempt to reduce the tooth displacement magnitudes due to constriction. This did not have such a significant effect as hoped for, but did show more clearly the difference in tooth displacement responses due to magnetic and gravitational force.

The symmetry and mechanical stiffness of force rig Design 4 made this design more applicable to EMs. This has been validated by tooth displacement results in Experiment 3 being in the same range as those predicted by Hooke's law. However, as Hooke's law predicts a linear displacement response of an elastic material to an applied force, it does

not take into account any additional factors affecting the material such as magnetic saturation and thermal expansion. In EMs, the stator teeth are wound with stator windings producing heat and their cores are constructed from nonlinear material that may approach saturation. Therefore, both of these factors must also affect the tooth displacement in a machine. It is suggested then, that the radial displacement of the stator teeth in EMs may possibly bear more relation to the findings of this work than to the linear elastic displacement predicted by Hooke's law.

Repeatability of the measured results was considered in order to add credibility to the experimental outcomes. Therefore, each experiment comprised ten tests. In the first two experiments, the ten tests comprised five identical tests for mass-induced force and five identical tests for flux-induced force, respectively, with results compared. In the third experiment, only the displacement by flux-induced force was considered, where ten identical tests were carried out, with results compared. Repeatability was especially significant in the third experiment, as taking measurements on the nano-scale is an extremely sensitive process prone to many possible measurement errors. However, it was found that the results for all ten tests in Experiment 3 showed relatively close agreement.

Temperature change and saturation of the core were shown to be the biggest contributors toward measurement errors in this work. A temperature regulating system was constructed in order to cool down the core in between measurements, thereby ensuring that each measurement was taken at the same core temperature. However, heat-flexing of the limbs was still experienced during the time that the coils were being energised, resulting in a reduction in measured tooth displacement due to widening of the air gap in the y-direction. An attempt was also made to reduce the possibility of core saturation by making geometrical design improvements. However, a 3D FE study on Design 4 showed that the wound limbs were, in fact, saturated, resulting in more current being required by the coils, which in turn caused more heat to be dissipated by them.

The results of the 2D FE simulations in Section 3.2 showed that this method is not suitable for electromagnetic modelling where the depth of the core in the z-direction is small compared to the radial depth of the coil and where, in consequence, the core can

become saturated. In this study it was shown that the required excitation was greatly affected by the z-direction leakage flux, contributing towards the wound limbs becoming saturated, which was not possible to model in 2D. This resulted in the maximum required dc excitation per coil in the physical rig being in the order of ten times greater than that per coil in the FE simulation, leading to measurement errors. In Section 5.3.1.3, a 3D FE model gave results which agreed more closely to the required dc excitation associated with the physical rig.

The 2D – 3D force conversion in Section 5.3.1.2 has shown that the depth (z-direction) of the FE software is indeed not affected by the mesh scaling factor and that 1m can safely be assumed. The magnetic y-forces physically applied to the tooth of force rig Design 4 (associated with measured air gap normal flux density) compared well with the simulated y-forces in the air gap of the FE model of force rig Design 4 (associated with equivalent values of simulated air gap normal flux density). This provides some comfort in the knowledge of the y-forces associated with the measured tooth displacements in this work.

6.2 Recommendations

Future research, using this experimental force rig (Design 4) for magnetostatic tooth displacement measurements, suggests a number of improvements.

- In an attempt to eliminate saturation, the limbs should be increased in x-direction and the stack length should be increased in z-direction.
- Permanent magnets with known flux densities could be used instead of coils in order to eliminate heat-flexing. This may also simplify the force rig construction.
- Coils may still be a viable option, as the depth of the core will be compatible with the radial depth of the coil, thereby greatly reducing z-directed leakage flux and saturation, therefore requiring less exciting current, and generating less heat.
- The structure of the rig should be made more realistic by having an arch-shaped yoke, emulating the shape of the stator core back in an EM.
- Notwithstanding all of the above, the rig should be modelled by 3D FE software.

A good starting point for the implementation of the capacitive displacement measuring technique in EMs could be to incorporate the sensor into the rotor of an IM and perform a locked rotor test, with the sensor positioned underneath a tooth tip. This way, the sensor can operate under static measurement conditions while the flux pattern in the EM is dynamic. A suitable measuring target will be required, which may be solved by having a strip of iron embedded in a cavity cut out from the tooth tip, with a polished surface facing the sensor. The iron strip will be flush with the tooth tip surface, in order to affect the flux pattern as little as possible. This concept is illustrated in the enlarged portion of Figure 6.1

In an IM, the sensor may disturb the current distribution in the rotor bars, in addition to the rotor flux pattern, due to the sensor cavity in the rotor iron. A reluctance synchronous machine (RSM) has no rotor conductors and therefore may be a good first choice for the implementation of this measuring technique in the locked rotor test. An idea of how the CS02 sensor may be incorporated in a 5.5kW RSM is illustrated in Figure 6.1. Here a 90° cable connector would be used, and the sensor cable would exit the rotor iron in the z-direction.

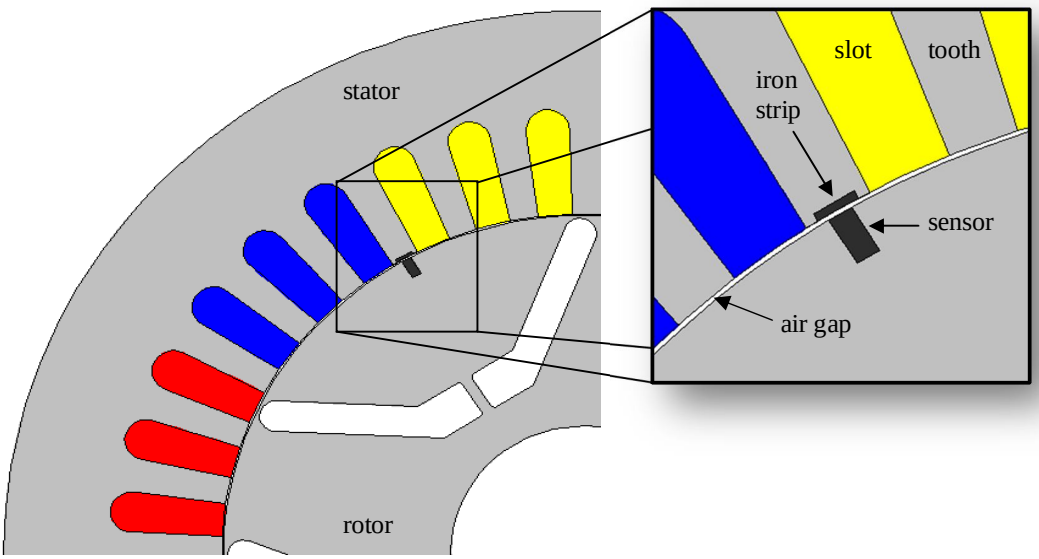

Fig. 6.1 Sensor position in a RSM

This measuring technique in large machines may allow an experiment in local force-induced displacements to be undertaken, by positioning three or more sensors facing the large tooth tip at different locations, possibly one at either end and one in the middle. However, it must be kept in mind that the greatest measuring range available with CapaNCDT is 10mm, limiting the maximum size of air gap that can be used. In addition, the size of the sensor increases as the required measuring range is increased. The measured force distributions from this experiment may be compared to published results.

For a PMSM it must be taken under consideration that the field of the permanent magnets needs to be incorporated into the referencing of the starting point for tooth displacement measurements. This would need to be done for both static (locked rotor) and dynamic (rotor moving) measurement conditions.

Dynamic measurement conditions are also made possible by CapaNCDT. An example of this is the measurement of deformation of a rotating brake disc under stress (Micro-Epsilon, 2013). Here, the target rotated at 2000r/min and a measurement resolution of 400nm was achieved. This opens up the possibility of exploring displacement measurements on the stator teeth of EMs as the rotor rotates.

The measurement of peripheral force-induced displacements on a tooth is a natural follow-up to this research, offering new challenges to be solved.

References

Agilent Technologies, 1999. *Practical Strain Gage Measurements*. Technical Manual.

AK Steel Corporation, 2007. *Selection of Electrical Steels for Magnetic Cores*. [Online] West Chester, USA Available at: http://www.aksteel.com/pdf/markets_products/electrical/Mag_Cores_Data_Bulletin.pdf [Accessed 26 January 2012].

Allcock, Andrew, 2011. *Machinery*. [Online] Available at: http://www.machinery.co.uk/machinery-features/non-contact-measurement/36676/ [Accessed 31 May 2012].

Balan, A. and Verma, S.P., 1993. Measurement techniques for vibration and acoustic noise of electrical machines. In *Proceedings of 6th international conference on Electrical machines and drives*. Oxford, UK, 1993. IEE Conf. Publ. No.376.

Balan, A. and Verma, S.P., 1994. Determination of radial forces in relation to noise and vibration problems of squirrel-cage induction motors. *IEEE Transactions on Energy Conversion*, 9(June), pp.404-12.

Balan, A and Verma, S.P., 1998. Experimental Investigations on the Stators of Electrical Machines in Relation to Vibration and Noise Problems. *IEE Proceedings on Electrical Power Applications*, 145(September), pp.455-61.

Barre, Olivier; Brochet, Pascal and Hecquet, Michel, 2006. Experimental Validation of Magnetic and Electric Local Force Formulations Associated to Energy Principle. *IEEE Transactions on Magnetics*, 42(4).

Barre, Olivier; Brochet, Pascal and Hecquet, Michel, n.d. Description of TEAM Workshop Problem 33a: Experimental Validation of Magnetic Local Force Formulations. *IEEE TEAM Workshop Paper*.

Belahcen, Anouar, 1999. Overview of the Calculation Methods for Forces in Magnetised Iron Cores of Electrical Machines. In *Seminar on Modelling and Simulation of Multi-Technological Machine Systems*. Espoo, Finland, 1999.

Belahcen, Anouar, 2004. *Magnetoelasticity, Magnetic Forces and Magnetostriction in Electrical Machines*. Ph.D. Thesis. Helsinki: Helsinki University of Technology.

Cameron, D.E.; Lang, J.H. and Umans, S.D., 1989. The origin of acoustic noise in variable-reluctance motors. *IEEE*.

Carpenter, C.J., 1959. Surface-integral Methods of Calculating Forces on Magnetised Iron Parts. *The Institution of Electrical Engineers*, Monograph No. 342(August).

Cogent, 2011. *Cogent*. [Online] Available at: http://www.sura.se/Sura/hp_products.nsf/vOpendocument/03A8B2433FAE16C4C1256AA8002280E6/$FILE/datasheets.pdf?OpenElement [Accessed 10 April 2012].

Collett, C.V. and Hope, A.D., 1983. Strain Measurement. In *Engineering Measurements*. 2nd ed. Pitman Publishing Inc. p.166.

Delaere, Koen; Heylen, Ward; Belmans, Ronnie and Hameyer, Kay, 2002. Comparison of Inductor Machine Stator Vibration Spectra Induced by Reluctance Forces and Magnetostriction. *I.E.E.E. Transactions on Magnetics*, 38(2).

Dwight, H.B., 1920. Calculation of Magnetic Force on Disconnecting Switches. In *36th Annual Convention of the American Institute of Electrical Engineers*. White Sulphur Springs, 1920. AIEE Transactions.

Dye, M. and Binns, K.J., 1972. Identification of Principal Factors Causing Unbalanced Magnetic Pull in Cage Induction Motors. In *IEE Annual Conference*., 1972. IEE.

Ekreem, N.B.; Olabi, A.G.; Prescott, T.; Rafferty, A. and Hashmi, M.S.J., 2007. An overview of magnetostriction, its use and methods to measure these properties. *Elsevier Journal of Materials Processing Technology*, 191, pp.96-101.

Garrigan, Neil R.; Soong, Wen L.; Stephens, Charles M.; Storace, A. and Lipo, Thomas A., 1999. Radial Force Characteristics of a Switched Reluctance Machine. In *Industry Applications Conference, 34th IAS Annual Meeting*., 1999. IEEE.

Ghalamestani, Setareh Gorji; Hilgert, Tom G.D.; Vandevelde, Lieven; Dirckx, Joris J.J. and Melkebeek, Jan A.A., 2010. Magnetostriction Measurement by Using Dual Heterodyne Laser Interferometers. *IEEE Transactions on Magnetics*, 46(February), pp.505-08.

Griffiths, D.J., 1999. *Introduction to Electrodynamics*. 3rd ed. New Jersey: Prentice-Hall International Inc.

Heyns, Gideon, 2011. *Analysis of Harmonic Field Effects in Reluctance Synchronous Machines*. MTech Thesis. Cape Town: Cape Peninsula University of Technology.

Husain, Iqbal and Islam, Rakib, 2010. Analytical Model for Predicting Noise and Vibration in Permanent Magnet Synchronous Motors. *IEEE Transactions on Industry Applications*, 46(November), pp.2346-54.

Ito, M.; Tajima, F. and Kanazawa, H., 1990. Evaluation of Force Calculating Methods. *IEEE Transactions on Magnetics*, 26(March), pp.1035-38.

Kabashima, Takefumi; Kawahara, Atsushi and Goto, Tadahiko, 1988. Force calculation using magnetising currents. *IEEE Transactions on Magnetics*, 24(January), pp.451-54.

Kuphaldt, T.R., 2000. *Sensorland*. [Online] Available at: http://www.sensorland.com/HowPage002.html [Accessed 14 June 2012].

Lee, Thomas H., 1957. Forces and Stresses in an Electromagnetic Field. In *Winter General Meeting of the A.I.E.E.* New York, 1957.

Lee, Se-hee; Park, Il-han and Lee, Ki-sik, 2000. Comparison of Mechanical Deformations Due to Different Force Distributions of Two Equivalent Magnetisation Models. *I.E.E.E. Transactions on Magnetics*, 36(4).

Levinson, I.J., 1978. *Machine Design*. Reston Publishing Company, Inc.

Melkebeek, Jan A.A. and Vandevelde, Lieven, 2001. A Survey of Magnetic Force Distributions Based on Different Magnetisation Models and on the Virtual Work Principle. *IEEE Transactions on Magnetics*, 37(5).

Melkebeek, Jan A.A. and Vandevelde, Lieven, 2001. Magnetic forces and Magnetostriction in Ferromagnetic Material. *Compel*, 20(1), pp.32-50.

Melkebeek, Jan A.A. and Vandevelde, Lieven, 2002. Modelling of Magnetoelastic Material. *IEEE Transactions on Magnetics*, 38(2), pp.993-96.

Melkebeek, Jan A.A. and Vandevelde, Lieven, 2003. Magnetic Forces and Magnetostriction in Electrical Machines and Transformer Cores. *IEEE Transactions on Magnetics*, 39(3), pp.1618-21.

Micro-Epsilon, 2012. *capaNCDT: High resolution capacitive displacement sensors and systems*. Product Catalogue. Ortenburg, Germany: Micro-Epsilon.

Micro-Epsilon, 2012. *Confocal chromatic displacement sensors*. Product Catalogue. Ortenburg, Germany: Micro-Epsilon.

Micro-Epsilon, 2012. *eddyNCDT3300: Non contact eddy current sensors*. Product Catalogue. Ortenburg, Germany: Micro-Epsilon.

Micro-Epsilon, 2012. *Laser Triangulation Displacement Sensors*. Product Catalogue. Ortenburg, Germany: Micro-Epsilon.

Micro-Epsilon, 2013. *Deformation of a brake disc under stress*. Capacitive Displacement Sensors. Ortenburg, Germany: Micro-Epsilon.

Morris, A.S., 2001. *Measurement and Instrumentation Principles*. 3rd ed. Oxford: Butterworth-Heinemann.

Muller, W., 1990. Comparison of Different Methods of Force Calculation. *IEEE Transactions on Magnetics*, 26(March), pp.1058-61.

National Instruments, 2011. *Fundamentals of FBG Optical Sensing*. Tutorial. Midrand, South Africa: National Instruments.

Park, R.H. and Doherty, R.E., 1926. Mechanical Force Between Electric Circuits. In *Midwinter Convention of the AIEE*. New York, 1926. AIEE Transactions.

Priday, G.L. and Seletzky, A.C., 1935. Bridge Measurement of Electromagnetic Forces. *A.I.E.E.*, (November), pp.1149-52.

Reichert, K.; Freundl, H. and Vogt, W., 1976. *The Calculation of Forces and Torques Within Numerical Magnetic Field Calculation Methods.* Article. Canada: Compumag University of Victoria.

Ren, Z., 1994. Comparison of Different Force Calculation Methods in 3D Finite Element Modelling. *IEEE Transactions on Magnetics*, 30(September), pp.3471-74.

Reyne, G.; Sabonnadierre, J.C.; Coulomb, J.L. and Brissonneau, P., 1987. A Survery of the Main Aspects of Magnetic Forces and Mechanical Behaviour of Ferromagnetic Materials under Magnetisation. *I.E.E.E. Transactions on Magnetics*, Mag-23(5).

Rodriguez, Pedro Vicente Jover; Belahcen, Anouar; Arkkio, Antero; Laiho, Antti and Antonino-Daviu, Jose A., 2007. Air-gap force distribution and vibration pattern of Induction motors under dynamic eccentricity. *Springer-Verlag (Electr Eng)*, pp.209-18.

Roper, J.W., 1927. Experimental Measurement of Mechanical Forces in Electric Circuits. In *Regional Meeting of District No.1 of the AIEE*. Pittsfield, Massachusetts, 1927. AIEE Transactions.

Shahaj, Annabel, 2010. *Mitigation of Vibration in Large Electrical Machines*. Ph.D. dissertation. Nottingham, UK: University of Nottingham.

Somkun, Sakda; Moses, Anthony J and Anderson, Philip I., 2012. Measurement and Modelling of 2-D Magnetostriction of Nonoriented Electrical Steel. *IEEE Transactions on Magnetics*, 48(February), pp.711-14.

Steinmetz, C.P., 1911. Mechanical Forces in Magnetic Fields. In *Mid-year Convention of the American Institute of Electrical Engineers*. Pittsfield-Schenectady, 1911. AIEE.

Sturgess, Jonathan and Voss, Egon, 2007. Tooth Forces in Small Machines. In *Modelling & Design of Electromagnetic Actuators and Machines*. Newcastle, England, 2007. UK Magnetics Society.

The Engineering Toolbox, 2013. *Coefficients of Linear Thermal Expansion*. [Online] Available at: http://www.engineeringtoolbox.com/linear-expansion-coefficients-d_95.html [Accessed 7 May 2013].

Torregrossa, Dimitri; Peyraut, Francois; Fahimi, Babak; M'Boua, Jeremie and Miraoui, Abdellatif, 2011. Multiphysics Finite-Element Modelling for Vibration and Acoustic Analysis of Permanent Magnet Synchronous Machine. *IEEE Transactions on Energy Conversion*, 26(June), pp.490-500.

Umenei, A.E.; Melikhov, Y. and Jiles, D.C., 2011. Models for Extrapolation of Magnetization Data on Magnetic Cores to High Fields. *IEEE*, 47(12), pp.4707-11.

Vandevelde, L.; Hilgert, T.G.D. and Melkebeek, J.A.A., 2004. Magnetostriction and magnetic forces in electrical steel: finite element computations and measurements. *IEE Proceedings on science, measurement and technology*, 151(November), pp.456-59.

Vaske, P. and Moeller, F., 1976. *Elektrische Maschinen und Umformer, Teil 1*. Hamburg: B.G. Teubner Stuttgart.

Wignall, A.N.; Gilbert, A.J. and Yang, S.J., 1988. Calculation of Forces on Magnetised Ferrous Cores Using the Maxwell Stress Method. *IEEE Transactions on Magnetics*, 24(1), pp.459-62.

Zhu, Weidong; Fahimi, Babak and Pekarek, Steve, 2006. A Field Reconstruction Method for Optimal Excitation of Permanent Magnet Synchronous Machines. *IEEE Transactions on Energy Conversion*, 21(2), pp.305-13.

Appendices

Appendix A: M270-35A (M-19, 0.35mm) silicon steel datasheet

Typical data for SURA® M270-35A

T	W/kg at 50 Hz	VA/kg at 50 Hz	A/m at 50 Hz	W/kg at 100 Hz	W/kg at 200 Hz	W/kg at 400 Hz	W/kg at 1000 Hz	W/kg at 2500 Hz
0,1	0,03	0,06	30,0	0,04	0,09	0,21	0,99	4,10
0,2	0,07	0,17	39,6	0,16	0,37	0,92	3,67	14,9
0,3	0,13	0,29	46,0	0,34	0,79	1,99	7,63	30,7
0,4	0,22	0,44	52,0	0,55	1,31	3,33	12,7	52,0
0,5	0,31	0,61	58,2	0,80	1,91	4,94	18,9	79,1
0,6	0,43	0,81	65,2	1,06	2,61	6,84	26,4	113
0,7	0,54	1,04	73,3	1,38	3,39	9,00	35,4	156
0,8	0,68	1,31	83,1	1,73	4,26	11,4	46,0	209
0,9	0,83	1,63	95,5	2,10	5,23	14,2	58,4	274
1,0	1,01	2,04	112	2,51	6,30	17,3	73,0	353
1,1	1,20	2,58	136	2,98	7,51	20,9	90,1	
1,2	1,42	3,38	178	3,51	8,88	24,9		
1,3	1,70	4,90	272	4,15	10,5	29,5		
1,4	2,12	9,64	596	4,97	12,5	35,4		
1,5	2,47	28,0	1700	5,92	14,9	41,8		
1,6	2,80	72,3	3880					
1,7	3,05	149	7160					
1,8	3,25	264	11600					

Loss at 1.5 T , 50 Hz, W/kg	2,47
Loss at 1.0 T , 50 Hz, W/kg	1,01
Anisotropy of loss, %	10
Magnetic polarization at 50 Hz	
H = 2500 A/m, T	1,54
H = 5000 A/m, T	1,65
H = 10000 A/m, T	1,77
Coercivity (DC), A/m	40
Relative permeability at 1.5 T	700
Resistivity, μΩcm	52
Yield strength, N/mm²	450
Tensile strength, N/mm²	565
Young's modulus, RD, N/mm²	185 000
Young's modulus, TD, N/mm²	200 000
Hardness HV5 (VPN)	215

RD represents the rolling direction
TD represents the transverse direction
Values for yield strength (0.2 % proof strength) and tensile strength are given for the rolling direction
Values for the transverse direction are approximately 5% higher

cogent
Surahammars Bruks AB

Appendix B: M250-35A (M-15, 0.35mm) silicon steel datasheet

Typical data for SURA® M250-35A

T	W/kg at 50 Hz	VA/kg at 50 Hz	A/m at 50 Hz	W/kg at 100 Hz	W/kg at 200 Hz	W/kg at 400 Hz	W/kg at 1000 Hz	W/kg at 2500 Hz
0,1	0,02	0,06	26,8	0,04	0,08	0,21	0,98	4,09
0,2	0,06	0,15	35,7	0,14	0,33	0,90	3,65	14,8
0,3	0,13	0,27	41,8	0,31	0,73	1,93	7,58	30,6
0,4	0,21	0,40	47,5	0,51	1,23	3,24	12,7	51,7
0,5	0,31	0,56	53,4	0,75	1,82	4,81	18,8	78,8
0,6	0,41	0,74	60,0	1,01	2,49	6,69	26,3	113
0,7	0,52	0,95	67,9	1,31	3,26	8,82	35,2	155
0,8	0,66	1,21	77,5	1,64	4,12	11,2	45,7	208
0,9	0,81	1,52	90,0	2,00	5,07	14,0	58,1	273
1,0	0,98	1,92	107	2,41	6,14	17,1	72,6	352
1,1	1,15	2,46	133	2,87	7,33	20,6	89,6	
1,2	1,37	3,30	179	3,40	8,69	24,6		
1,3	1,65	4,97	284	4,03	10,3	29,2		
1,4	2,00	10,3	642	4,83	12,4	35,1		
1,5	2,35	30,0	1810	5,72	14,7	41,6		
1,6	2,65	75,7	4030					
1,7	2,87	153	7290					
1,8	3,06	267	11700					

Loss at 1.5 T , 50 Hz, W/kg	2,35
Loss at 1.0 T , 50 Hz, W/kg	0,98
Anisotropy of loss, %	10
Magnetic polarization at 50 Hz	
H = 2500 A/m, T	1,53
H = 5000 A/m, T	1,64
H = 10000 A/m, T	1,76
Coercivity (DC), A/m	40
Relative permeability at 1.5 T	660
Resistivity, μΩcm	55
Yield strength, N/mm²	455
Tensile strength, N/mm²	575
Young's modulus, RD, N/mm²	185 000
Young's modulus, TD, N/mm²	200 000
Hardness HV5 (VPN)	215

RD represents the rolling direction
TD represents the transverse direction
Values for yield strength (0.2 % proof strength)
and tensile strength are given for the rolling direction
Values for the transverse direction are approximately 5% higher

cogent
Surahammars Bruks AB

Appendix C: Information on enamel conductor insulation

aev
Qualities that Bond

TECHNICAL BULLETIN

PRODUCT INFORMATION

ULTIMEG 2000-372#
ANTI TRACKING
AIR DRYING ALKYD
CLEAR, GOLDEN
PIGMENTED VERSIONS AVAILABLE
CLASS H – UL File no. E220579
AEROSOL VERSIONS AVAILABLE

ULTIMEG 2000-372# ANTI-TRACKING ENAMELS AND VARNISHES

GENERAL DESCRIPTION

The Ultimeg 2000-372# range of anti-tracking varnishes and enamels provide tough, impervious, insulating seals in difficult environments. The system dries rapidly in thin film to give very effective sealing off of electrical leakage paths together with excellent noise reduction characteristics. The cured product conforms to BSEN 600464 type 1.1 (IEC600464), has excellent resistance to transformer oils and moisture, and is suitable for use in Class H insulating systems. The system has been tested to ASTM D2307 and achieved 20,000hrs rating at >180°C and is recognised to UL1446 file number E220579. A low hazard fungicide is included in the varnished enamels, which gives a 0 rating (no growth) fungal resistance when tested to BS 3900 PTG6. This makes the system particularly suited for tropicalisation and for use on equipment working in warm humid climates.

APPLICATION

Suitable for noise reduction in small transformers and moisture protection, anti-tracking and tropicalisation on all types of electrical equipment.

SPECIFICATION

Viscosity	200-300 cPs at 25°C	
Non-volatile content	38-42%	(Clear & golden versions)
Specific Gravity	0.96-99	(Clear & golden versions)
Flashpoint	27°C	
Shelf life	12 months at 21°C	
Drying time	Touch dry	15 minutes
	Hard dry	45-60 minutes
	Full cure	24 hour

NOTE: Due to the introduction of improvements from time to time the right is reserved to supply products that may differ slightly from those illustrated or described in this publication.

Email: aev@aev.co.uk
www.aev.co.uk

AEV Limited,
Marion Street, Birkenhead,
Wirral. U.K CH41 6LT
Tel: ++ 44 (0) 151 647 3322
Fax: ++ 44 (0) 151 647 3377

Appendix D: Current carrying capacities of copper conductors at specific insulation temperature ratings

ISO 10133:2000(E)

Table A.1 — Cross-sectional area of conductor, allowable continuous current and stranding

Cross-sectional area	Maximum current, in amperes, for single conductors at insulation temperature ratings						Minimum number of strands	
mm²	60 °C	70 °C	85 °C to 90 °C	105 °C	125 °C	200 °C	Type A	Type B
0,75	6	10	12	16	20	25	16	—
1	8	14	18	20	25	35	16	—
1,5	12	18	21	25	30	40	19	26
2,5	17	25	30	35	40	45	19	41
4	22	35	40	45	50	55	19	65
6	29	45	50	60	70	75	19	105
10	40	65	70	90	100	120	19	168
16	54	90	100	130	150	170	37	266
25	71	120	140	170	185	200	49	420
35	87	160	185	210	225	240	127	665
50	105	210	230	270	300	325	127	1 064
70	135	265	285	330	360	375	127	1 323
95	165	310	330	390	410	430	259	1 666
120	190	360	400	450	480	520	418	2 107
150	220	380	430	475	520	560	418	2 107

Conductors with at least Type A stranding shall be used for general wiring of the craft. Conductors with Type B stranding shall be used for any wiring where frequent flexing is involved during use.

NOTE Conductor current ratings may be interpolated for cross-sectional areas between those shown above.

Appendix E: Static characteristics of measurement systems

Accuracy

This describes how close the instrument's output reading is to the correct value of the measurand. It is common to state an instrument's inaccuracy figure rather than its accuracy figure, given as a percentage of full-scale output (FSO) of the instrument.

Full scale output (FSO)

FSO describes the difference between the minimum and maximum output value of a measurement device, in this case the measuring range for the CapaNCDT CS02 sensor is 0 - 0.2mm which equates to 0 - 10V dc, 10V then being the FSO for this device.

Precision

This describes to what degree an instrument's readings will be affected by random errors. If a high-precision instrument takes a large number of readings then the extent to which these readings differ from each other will be very small.

Repeatability

This describes the extent to which an instrument's output readings deviate from one another when the same input is repeatedly applied over a short time period with the same instrument, user, measurement conditions, location and conditions of use.

Sensitivity

This describes the relationship concerning change in instrument output when there is a change in the input, being either linear or nonlinear in nature. This is also known as scale factor. Sensitivity is the ratio of scale deflection to measurand value producing deflection.

Linearity

When incremental changes are applied to the input of an instrument and the output values remain constant relative to these inputs over the instruments specified operating range that instrument is said to be linear. Nonlinearity is usually stated as a percentage of FSO.

Resolution

This describes the smallest change in an instrument's input that produces a small but definite change in the output. This can either be specified as an absolute value or as a percentage of FSO.

Threshold

This describes the minimum value of input change increased from zero that causes a detectable output change in the instrument. This can be specified as an absolute value or as a percentage of FSO.

Dead band

This describes a range of input values over which the output of an instrument does not respond. This can be caused either by backlash in gears, friction or hysteresis in the instrument.

Hysteresis

This can be described as the non-coincidence between loading and unloading curves of an instrument for a given measurement. Due to energy stored in the system, the decreasing input curve (unloading), once increased to maximum, will not correspond to the curve produced when the input was increasing (loading).

Sensitivity to disturbance

This describes any change in an instrument's static characteristics caused by a variation in the standard ambient conditions under which the instrument was calibrated and/or specified to operate. Such environmental changes may affect an instrument in two ways. When a change in ambient conditions modifies the zero reading of an instrument, causing a constant error existing over the full measurement range, it is known as zero drift or bias. The degree to which an instrument's sensitivity varies relative to a change in ambient conditions is known as sensitivity drift or scale factor drift.

(Collett, 1983) (Morris, 2001)

Appendix F: **Technical specifications of capacitive sensor and controller** (Micro-Epsilon, 2012)

CAPACITIVE SENSOR	**CS02**
MEASURING RANGE	0.2mm
LINEARITY	0.2% FSO
RESOLUTION (STATIC, 2Hz)	0.15nm
RESOLUTION (DYNAMIC, 8.5kHz)	4nm
TEMPERATURE STABILITY ZERO	60nm/°C
TEMPERATURE STABILITY SENSITIVITY	-10ppm/°C
TEMPERATURE RANGE (OPERATION)	-50 … +200 °C
AIR HUMIDITY	0 … 95% r.H.
SENSOR DIMENSIONS	6 × 12mm
ACTIVE MEASURING AREA	2.3mm
GUARD RING WIDTH	1mm
MINIMUM TARGET DIAMETER	5mm
WEIGHT	2g
MATERIAL (HOUSING)	MAGNESIUM
CONTROLLER TYPE	**DT6300**
RESOLUTION STATIC	0.001% FSO
RESOLUTION DYNAMIC	0.01% FSO
BANDWIDTH	8kHz
BANDWIDTH ADJUSTABLE	20Hz / 1kHz / 8kHz
LINEARITY	+0.2% FSO
MAXIMUM SENSITIVITY DEVIATION	+0.1% FSO
LONG TERM STABILITY	0.02% /MONTH
AMBIENT PRESSURE	ATMOSPHERIC
TEMPERATURE STABILITY	0.01% FSO / °C
TEMPERATURE RANGE (OPERATION)	+10 … +50 °C
SUPPLY	15Vdc / 150mA
OUTPUT	0-10Vdc / 4-20mA

Appendix GA: Experiment 1 Test 1: Measured results

MASS (kg)	FORCE (N)	STARTING VOLTAGE / REFERENCE POINT (V)	VOLTAGE DUE TO APPLIED MASS (V)	AIR GAP LENGTH FROM SENSOR TO TARGET (mm)	CHANGE IN AIR GAP LENGTH FROM REFERENCE POINT (µm)
0	0	14.011	14.011	0.28022	0
0.5	4.905	14.011	13.369	0.26738	12.84
1	9.81	14.003	12.455	0.2491	30.96
1.5	14.715	13.995	11.454	0.22908	50.82
2	19.62	13.99	10.2655	0.20531	74.49
2.5	24.525	13.986	9.148	0.18296	96.76
3	29.43	13.982	8.285	0.1657	113.94
3.5	34.335	13.98	6.99155	0.139831	139.769
4	39.24	13.91	5.794	0.11588	162.32
4.5	44.145	13.786	4.94812	0.0989624	176.7576
5	49.05	13.815	4.346	0.08692	189.38
5.5	53.955	13.308	4.5191	0.090382	175.778
6	58.86	13.593	4.2614	0.085228	186.632
6.5	63.765	13.686	4.31425	0.086285	187.435
7	68.67	13.959	4.42075	0.088415	190.765
7.5	73.575	13.821	4.3769	0.087538	188.882
8	78.48	13.679	4.37955	0.087591	185.989
8.5	83.385	13.601	4.51165	0.090233	181.787
9	88.29	13.96	4.22935	0.084587	194.613
9.5	93.195	13.958	4.4105	0.08821	190.95

FLUX (T)	FORCE (N)	STARTING VOLTAGE / REFERENCE POINT (V)	VOLTAGE DUE TO APPLIED FLUX (V)	AIR GAP LENGTH FROM SENSOR TO TARGET (mm)	CHANGE IN AIR GAP LENGTH FROM REFERENCE POINT (µm)
0.12	0	13.194	13.194	0.26388	0
0.2315	4.905	13.194	12.265	0.2453	18.58
0.3274	9.81	13.394	11.0425	0.22085	47.03
0.4009	14.715	13.384	9.682	0.19364	74.04
0.463	19.62	13.35	8.139	0.16278	104.22
0.5176	24.525	13.295	7.11695	0.142339	123.561
0.567	29.43	13.277	5.951	0.11902	146.52
0.6125	34.335	13.255	4.981665	0.0996333	165.4667
0.6548	39.24	13.768	4.64595	0.092919	182.441
0.6945	44.145	13.69	4.3846	0.087692	186.108
0.732	49.05	13.64	4.3945	0.08789	184.91
0.7678	53.955	13.617	4.4101	0.088202	184.138
0.802	58.86	13.594	4.43225	0.088645	183.235
0.8346	63.765	13.57	4.43555	0.088711	182.689
0.866	68.67	13.525	4.46985	0.089397	181.103
0.8965	73.575	13.508	4.48625	0.089725	180.435
0.926	78.48	13.494	3.0174	0.060348	209.532
0.9545	83.385	13.483	3.0338	0.060676	208.984
0.982	88.29	13.475	3.055	0.0611	208.4
1.009	93.195	13.47	3.06825	0.061365	208.035

Appendix GB: Experiment 1 Test 2: Measured results

MASS (kg)	FORCE (N)	STARTING VOLTAGE / REFERENCE POINT (V)	VOLTAGE DUE TO APPLIED MASS (V)	AIR GAP LENGTH FROM SENSOR TO TARGET (mm)	CHANGE IN AIR GAP LENGTH FROM REFERENCE POINT (µm)
0	0	13.609	13.609	0.27218	0
0.5	4.905	13.609	12.6685	0.25337	18.81
1	9.81	13.59	11.6445	0.23289	38.91
1.5	14.715	13.544	10.7365	0.21473	56.15
2	19.62	13.508	9.347	0.18694	83.22
2.5	24.525	13.389	8.1307	0.162614	105.166
3	29.43	13.156	6.74155	0.134831	128.289
3.5	34.335	12.81	5.7608	0.115216	140.984
4	39.24	12.76	4.783005	0.0956601	159.5399
4.5	44.145	12.69	4.7697	0.095394	158.406
5	49.05	12.042	4.3544	0.087088	153.752
5.5	53.955	11.66	4.3478	0.086956	146.244
6	58.86	11.6	4.43395	0.088679	143.321
6.5	63.765	10.41	4.41745	0.088349	119.851
7	68.67	11.04	4.67545	0.093509	127.291
7.5	73.575	13.471	4.43795	0.088759	180.661
8	78.48	13.047	4.46835	0.089367	171.573
8.5	83.385	13.088	4.39885	0.087977	173.783
9	88.29	13.295	4.427	0.08854	177.36
9.5	93.195	12.385	4.94259	0.0988518	148.8482
FLUX (T)	**FORCE (N)**	**STARTING VOLTAGE / REFERENCE POINT (V)**	**VOLTAGE DUE TO APPLIED FLUX (V)**	**AIR GAP LENGTH FROM SENSOR TO TARGET (mm)**	**CHANGE IN AIR GAP LENGTH FROM REFERENCE POINT (µm)**
0.12	0	12.6895	12.6895	0.25379	0
0.2315	4.905	12.6895	11.681	0.23362	20.17
0.3274	9.81	12.822	10.474	0.20948	46.96
0.4009	14.715	12.793	9.152	0.18304	72.82
0.463	19.62	12.74	7.74975	0.154995	99.805
0.5176	24.525	12.694	6.46155	0.129231	124.649
0.567	29.43	12.54	5.4026	0.108052	142.748
0.6125	34.335	12.527	4.6122	0.092244	158.296
0.6548	39.24	12.52	4.60275	0.092055	158.345
0.6945	44.145	12.51	4.6104	0.092208	157.992
0.732	49.05	12.488	4.6216	0.092432	157.328
0.7678	53.955	12.48	4.6297	0.092594	157.006
0.802	58.86	12.485	4.64545	0.092909	156.791
0.8346	63.765	12.477	4.66145	0.093229	156.311
0.866	68.67	12.474	4.6783	0.093566	155.914
0.8965	73.575	12.467	4.69706	0.0939412	155.3988
0.926	78.48	12.468	4.71045	0.094209	155.151
0.9545	83.385	12.468	4.725825	0.0945165	154.8435
0.982	88.29	12.474	4.741675	0.0948335	154.6465
1.009	93.195	12.493	4.76671	0.0953342	154.5258

Appendix GC: Experiment 1 Test 3: Measured results

MASS (kg)	FORCE (N)	STARTING VOLTAGE / REFERENCE POINT (V)	VOLTAGE DUE TO APPLIED MASS (V)	AIR GAP LENGTH FROM SENSOR TO TARGET (mm)	CHANGE IN AIR GAP LENGTH FROM REFERENCE POINT (µm)
0	0	12.031	12.031	0.24062	0
0.5	4.905	12.031	11.0745	0.22149	19.13
1	9.81	12.043	10.2	0.204	36.86
1.5	14.715	12.042	9.156	0.18312	57.72
2	19.62	12.034	8.07305	0.161461	79.219
2.5	24.525	12.011	6.93645	0.138729	101.491
3	29.43	11.955	5.9078	0.118156	120.944
3.5	34.335	11.93	4.890605	0.0978121	140.7879
4	39.24	11.89	4.862945	0.0972589	140.5411
4.5	44.145	11.832	4.900335	0.0980067	138.6333
5	49.05	11.7	4.79113	0.0958226	138.1774
5.5	53.955	11.857	3.09305	0.061861	175.279
6	58.86	11.874	2.8586	0.057172	180.308
6.5	63.765	11.988	3.07865	0.061573	178.187
7	68.67	11.957	2.8638	0.057276	181.864
7.5	73.575	12.029	3.4166	0.068332	172.248
8	78.48	13.26	2.9858	0.059716	205.484
8.5	83.385	12.935	5.318685	0.1063737	152.3263
9	88.29	10.084	5.3679	0.107358	94.322
9.5	93.195	11.048	5.263455	0.1052691	115.6909

FLUX (T)	FORCE (N)	STARTING VOLTAGE / REFERENCE POINT (V)	VOLTAGE DUE TO APPLIED FLUX (V)	AIR GAP LENGTH FROM SENSOR TO TARGET (mm)	CHANGE IN AIR GAP LENGTH FROM REFERENCE POINT (µm)
0.12	0	11.237	11.237	0.22474	0
0.2315	4.905	11.237	10.26	0.2052	19.54
0.3274	9.81	11.342	9.0015	0.18003	46.81
0.4009	14.715	11.325	7.9376	0.158752	67.748
0.463	19.62	11.316	6.63815	0.132763	93.557
0.5176	24.525	11.298	5.61445	0.112289	113.671
0.567	29.43	11.29	4.61945	0.092389	133.411
0.6125	34.335	11.34	4.58545	0.091709	135.091
0.6548	39.24	11.372	4.5852	0.091704	135.736
0.6945	44.145	11.409	4.59385	0.091877	136.303
0.732	49.05	11.416	4.605	0.0921	136.22
0.7678	53.955	11.417	4.61845	0.092369	135.971
0.802	58.86	11.429	4.6389	0.092778	135.802
0.8346	63.765	11.462	4.6511	0.093022	136.218
0.866	68.67	12.083	4.64895	0.092979	148.681
0.8965	73.575	12.096	4.67485	0.093497	148.423
0.926	78.48	12.088	4.6907	0.093814	147.946
0.9545	83.385	12.097	4.7095	0.09419	147.75
0.982	88.29	12.383	4.71109	0.0942218	153.4382
1.009	93.195	12.444	4.728285	0.0945657	154.3143

Appendix GD: Experiment 1 Test 4: Measured results

MASS (kg)	FORCE (N)	STARTING VOLTAGE / REFERENCE POINT (V)	VOLTAGE DUE TO APPLIED MASS (V)	AIR GAP LENGTH FROM SENSOR TO TARGET (mm)	CHANGE IN AIR GAP LENGTH FROM REFERENCE POINT (µm)
0	0	11.052	11.052	0.22104	0
0.5	4.905	11.052	10.0235	0.20047	20.57
1	9.81	11.043	9.1995	0.18399	36.87
1.5	14.715	11.044	8.13005	0.162601	58.279
2	19.62	11.024	6.98845	0.139769	80.711
2.5	24.525	10.99	5.9357	0.118714	101.086
3	29.43	10.96	4.78976	0.0957952	123.4048
3.5	34.335	10.805	4.49275	0.089855	126.245
4	39.24	10.86	4.5335	0.09067	126.53
4.5	44.145	10.827	4.56065	0.091213	125.327
5	49.05	10.789	4.764995	0.0952999	120.4801
5.5	53.955	10.899	5.22365	0.104473	113.507
6	58.86	10.606	5.17087	0.1034174	108.7026
6.5	63.765	10.58	4.31135	0.086227	125.373
7	68.67	10.773	4.6944	0.093888	121.572
7.5	73.575	9.369	4.825635	0.0965127	90.8673
8	78.48	9.587	4.6497	0.092994	98.746
8.5	83.385	9.752	4.43915	0.088783	106.257
9	88.29	10.396	3.0557	0.061114	146.806
9.5	93.195	10.587	4.34575	0.086915	124.825

FLUX (T)	FORCE (N)	STARTING VOLTAGE / REFERENCE POINT (V)	VOLTAGE DUE TO APPLIED FLUX (V)	AIR GAP LENGTH FROM SENSOR TO TARGET (mm)	CHANGE IN AIR GAP LENGTH FROM REFERENCE POINT (µm)
0.12	0	12.804	12.804	0.25608	0
0.2315	4.905	12.804	11.8765	0.23753	18.55
0.3274	9.81	12.907	10.675	0.2135	44.64
0.4009	14.715	12.887	9.509	0.19018	67.56
0.463	19.62	12.85	8.241	0.16482	92.18
0.5176	24.525	12.812	7.0315	0.14063	115.61
0.567	29.43	12.75	5.8194	0.116388	138.612
0.6125	34.335	12.67	4.6497	0.092994	160.406
0.6548	39.24	12.555	2.8597	0.057194	193.906
0.6945	44.145	12.525	2.81955	0.056391	194.109
0.732	49.05	12.525	2.8147	0.056294	194.206
0.7678	53.955	12.515	2.8152	0.056304	193.996
0.802	58.86	12.515	2.8228	0.056456	193.844
0.8346	63.765	12.505	2.83715	0.056743	193.357
0.866	68.67	13.132	2.83235	0.056647	205.993
0.8965	73.575	13.0827	2.8464	0.056928	204.726
0.926	78.48	13.0535	2.86635	0.057327	203.743
0.9545	83.385	13.3242	2.86185	0.057237	209.247
0.982	88.29	13.3257	2.88295	0.057659	208.855
1.009	93.195	13.4784	2.88985	0.057797	211.771

Appendix GE: Experiment 1 Test 5: Measured results

MASS (kg)	FORCE (N)	STARTING VOLTAGE / REFERENCE POINT (V)	VOLTAGE DUE TO APPLIED MASS (V)	AIR GAP LENGTH FROM SENSOR TO TARGET (mm)	CHANGE IN AIR GAP LENGTH FROM REFERENCE POINT (µm)
0	0	12.788	12.788	0.25576	0
0.5	4.905	12.788	11.80285	0.236057	19.703
1	9.81	12.81	10.9091	0.218182	38.018
1.5	14.715	12.7722	9.82775	0.196555	58.889
2	19.62	12.715	8.56055	0.171211	83.089
2.5	24.525	12.721	7.7346	0.154692	99.728
3	29.43	12.741	6.68635	0.133727	121.093
3.5	34.335	12.6809	5.589105	0.1117821	141.8359
4	39.24	12.6551	4.81234	0.0962468	156.8552
4.5	44.145	12.6235	4.578645	0.0915729	160.8971
5	49.05	10.592	4.979177	0.09958354	112.25646
5.5	53.955	11.0973	4.356175	0.0871235	134.8225
6	58.86	11.2452	3.14525	0.062905	161.999
6.5	63.765	11.6634	2.87675	0.057535	175.733
7	68.67	11.8471	2.9786	0.059572	177.37
7.5	73.575	12.0104	4.260875	0.0852175	154.9905
8	78.48	12.1906	2.8371	0.056742	187.07
8.5	83.385	12.0162	4.262415	0.0852483	155.0757
9	88.29	11.9028	5.18276	0.1036552	134.4008
9.5	93.195	11.1645	2.8969	0.057938	165.352

FLUX (T)	FORCE (N)	STARTING VOLTAGE / REFERENCE POINT (V)	VOLTAGE DUE TO APPLIED FLUX (V)	AIR GAP LENGTH FROM SENSOR TO TARGET (mm)	CHANGE IN AIR GAP LENGTH FROM REFERENCE POINT (µm)
0.12	0	11.4	11.4	0.228	0
0.2315	4.905	11.4	10.35745	0.207149	20.851
0.3274	9.81	11.5	9.0976	0.181952	48.048
0.4009	14.715	11.47	7.71435	0.154287	75.113
0.463	19.62	11.44	6.4616	0.129232	99.568
0.5176	24.525	11.4	5.35829	0.1071658	120.8342
0.567	29.43	11.4	4.410165	0.0882033	139.7967
0.6125	34.335	11.35	3.02	0.0604	166.6
0.6548	39.24	11.35	3.0036	0.060072	166.928
0.6945	44.145	11.365	2.98975	0.059795	167.505
0.732	49.05	11.3545	3.0001	0.060002	167.088
0.7678	53.955	11.355	3.0031	0.060062	167.038
0.802	58.86	11.34	3.0395	0.06079	166.01
0.8346	63.765	11.33	3.0679	0.061358	165.242
0.866	68.67	11.3	3.0859	0.061718	164.282
0.8965	73.575	11.8	3.0472	0.060944	175.056
0.926	78.48	11.873	3.03155	0.060631	176.829
0.9545	83.385	12.095	3.0353	0.060706	181.194
0.982	88.29	12.155	3.04435	0.060887	182.213
1.009	93.195	11.98	3.10525	0.062105	177.495

Appendix HA: Experiment 2 Test 1: Measured results

MASS (kg)	FORCE (N)	STARTING VOLTAGE / REFERENCE POINT (V)	VOLTAGE DUE TO APPLIED MASS (V)	AIR GAP LENGTH FROM SENSOR TO TARGET (mm)	CHANGE IN AIR GAP LENGTH FROM REFERENCE POINT (µm)
0	0	6.212	6.212	0.12424	0
0.5	4.905	6.212	6.149	0.12298	1.26
1	9.81	6.212	6.088	0.12176	2.48
1.5	14.715	6.215	6.046	0.12092	3.38
2	19.62	6.214	5.955	0.1191	5.18
2.5	24.525	6.218	5.901	0.11802	6.34
3	29.43	6.215	5.831	0.11662	7.68
3.5	34.335	6.207	5.89	0.1178	6.34
4	39.24	6.215	5.84	0.1168	7.5
4.5	44.145	6.218	5.821	0.11642	7.94
5	49.05	6.335	5.482	0.10964	17.06
5.5	53.955	6.248	5.494	0.10988	15.08
6	58.86	6.265	5.473	0.10946	15.84
6.5	63.765	6.265	5.342	0.10684	18.46
7	68.67	6.255	5.369	0.10738	17.72
7.5	73.575	6.271	5.412	0.10824	17.18
8	78.48	6.31	5.258	0.10516	21.04
8.5	83.385	6.282	5.254	0.10508	20.56
9	88.29	6.288	5.31	0.1062	19.56
9.5	93.195	6.3	5.315	0.1063	19.7

FLUX (T)	FORCE (N)	STARTING VOLTAGE / REFERENCE POINT (V)	VOLTAGE DUE TO APPLIED FLUX (V)	AIR GAP LENGTH FROM SENSOR TO TARGET (mm)	CHANGE IN AIR GAP LENGTH FROM REFERENCE POINT (µm)
0.12	0	6.368	6.368	0.12736	0
0.2315	4.905	6.368	6.315	0.1263	1.06
0.3274	9.81	6.367	6.217	0.12434	3
0.4009	14.715	6.371	6.031	0.12062	6.8
0.463	19.62	6.36	5.857	0.11714	10.06
0.5176	24.525	6.355	5.62	0.1124	14.7
0.567	29.43	6.352	5.33	0.1066	20.44
0.6125	34.335	6.347	5.043	0.10086	26.08
0.6548	39.24	6.337	4.77	0.0954	31.34
0.6945	44.145	6.328	4.563	0.09126	35.3
0.732	49.05	6.315	4.386	0.08772	38.58
0.7678	53.955	6.305	4.233	0.08466	41.44
0.802	58.86	6.295	4.107	0.08214	43.76
0.8346	63.765	6.278	3.98	0.0796	45.96
0.866	68.67	6.271	3.871	0.07742	48
0.8965	73.575	6.27	3.755	0.0751	50.3
0.926	78.48	5.512	2.887	0.05774	52.5
0.9545	83.385	5.47	2.792	0.05584	53.56
0.982	88.29	5.58	2.776	0.05552	56.08
1.009	93.195	5.58	2.717	0.05434	57.26

Appendix HB: Experiment 2 Test 2: Measured results

MASS (kg)	FORCE (N)	STARTING VOLTAGE / REFERENCE POINT (V)	VOLTAGE DUE TO APPLIED MASS (V)	AIR GAP LENGTH FROM SENSOR TO TARGET (mm)	CHANGE IN AIR GAP LENGTH FROM REFERENCE POINT (µm)
0	0	7.909	7.909	0.15818	0
0.5	4.905	7.905	7.792	0.15584	2.26
1	9.81	7.905	7.763	0.15526	2.84
1.5	14.715	7.907	7.682	0.15364	4.5
2	19.62	7.905	7.685	0.1537	4.4
2.5	24.525	8.307	8.121	0.16242	3.72
3	29.43	8.275	7.997	0.15994	5.56
3.5	34.335	8.265	8.061	0.16122	4.08
4	39.24	8.275	8.114	0.16228	3.22
4.5	44.145	8.275	8.047	0.16094	4.56
5	49.05	8.288	8.11	0.1622	3.56
5.5	53.955	8.281	7.705	0.1541	11.52
6	58.86	8.261	7.575	0.1515	13.72
6.5	63.765	8.266	7.518	0.15036	14.96
7	68.67	8.288	7.338	0.14676	19
7.5	73.575	8.261	7.193	0.14386	21.36
8	78.48	8.26	7.043	0.14086	24.34
8.5	83.385	8.262	7.087	0.14174	23.5
9	88.29	8.287	6.931	0.13862	27.12
9.5	93.195	8.269	7.087	0.14174	23.64
FLUX (T)	**FORCE (N)**	**STARTING VOLTAGE / REFERENCE POINT (V)**	**VOLTAGE DUE TO APPLIED FLUX (V)**	**AIR GAP LENGTH FROM SENSOR TO TARGET (mm)**	**CHANGE IN AIR GAP LENGTH FROM REFERENCE POINT (µm)**
0.12	0	7.722	7.722	0.15444	0
0.2315	4.905	7.722	7.692	0.15384	0.6
0.3274	9.81	7.74	7.601	0.15202	2.78
0.4009	14.715	7.745	7.439	0.14878	6.12
0.463	19.62	7.749	7.274	0.14548	9.5
0.5176	24.525	7.748	7.024	0.14048	14.48
0.567	29.43	7.739	6.752	0.13504	19.74
0.6125	34.335	7.733	6.442	0.12884	25.82
0.6548	39.24	7.714	6.2	0.124	30.28
0.6945	44.145	7.707	6	0.12	34.14
0.732	49.05	7.7	5.835	0.1167	37.3
0.7678	53.955	7.672	5.67	0.1134	40.04
0.802	58.86	7.68	5.535	0.1107	42.9
0.8346	63.765	7.652	5.411	0.10822	44.82
0.866	68.67	7.64	5.293	0.10586	46.94
0.8965	73.575	7.64	5.188	0.10376	49.04
0.926	78.48	7.193	4.645	0.0929	50.96
0.9545	83.385	7.13	4.508	0.09016	52.44
0.982	88.29	7.165	4.451	0.08902	54.28
1.009	93.195	7.161	4.377	0.08754	55.68

Appendix Hc: Experiment 2 Test 3: Measured results

MASS (kg)	FORCE (N)	STARTING VOLTAGE / REFERENCE POINT (V)	VOLTAGE DUE TO APPLIED MASS (V)	AIR GAP LENGTH FROM SENSOR TO TARGET (mm)	CHANGE IN AIR GAP LENGTH FROM REFERENCE POINT (µm)
0	0	7.286	7.286	0.14572	0
0.5	4.905	7.286	7.234	0.14468	1.04
1	9.81	7.274	7.144	0.14288	2.6
1.5	14.715	7.282	7.13	0.1426	3.04
2	19.62	7.292	7.066	0.14132	4.52
2.5	24.525	7.288	7.046	0.14092	4.84
3	29.43	7.3	7.011	0.14022	5.78
3.5	34.335	7.293	7.035	0.1407	5.16
4	39.24	7.288	7.016	0.14032	5.44
4.5	44.145	7.285	6.859	0.13718	8.52
5	49.05	7.277	6.748	0.13496	10.58
5.5	53.955	7.275	6.595	0.1319	13.6
6	58.86	7.272	6.569	0.13138	14.06
6.5	63.765	7.283	6.735	0.1347	10.96
7	68.67	7.288	6.734	0.13468	11.08
7.5	73.575	7.281	6.639	0.13278	12.84
8	78.48	7.279	6.994	0.13988	5.7
8.5	83.385	7.314	6.801	0.13602	10.26
9	88.29	7.289	6.813	0.13626	9.52
9.5	93.195	7.285	6.706	0.13412	11.58
FLUX (T)	**FORCE (N)**	**STARTING VOLTAGE / REFERENCE POINT (V)**	**VOLTAGE DUE TO APPLIED FLUX (V)**	**AIR GAP LENGTH FROM SENSOR TO TARGET (mm)**	**CHANGE IN AIR GAP LENGTH FROM REFERENCE POINT (µm)**
0.12	0	7.25	7.25	0.145	0
0.2315	4.905	7.25	7.189	0.14378	1.22
0.3274	9.81	7.244	7.067	0.14134	3.54
0.4009	14.715	7.239	6.939	0.13878	6
0.463	19.62	7.235	6.713	0.13426	10.44
0.5176	24.525	7.231	6.489	0.12978	14.84
0.567	29.43	7.215	6.234	0.12468	19.62
0.6125	34.335	7.22	5.936	0.11872	25.68
0.6548	39.24	7.239	5.685	0.1137	31.08
0.6945	44.145	7.222	5.507	0.11014	34.3
0.732	49.05	7.208	5.342	0.10684	37.32
0.7678	53.955	7.192	5.211	0.10422	39.62
0.802	58.86	7.206	5.102	0.10204	42.08
0.8346	63.765	7.183	4.986	0.09972	43.94
0.866	68.67	7.185	4.882	0.09764	46.06
0.8965	73.575	6.865	4.414	0.08828	49.02
0.926	78.48	6.775	4.255	0.0851	50.4
0.9545	83.385	6.732	4.103	0.08206	52.58
0.982	88.29	5.583	2.83	0.0566	55.06
1.009	93.195	5.485	2.736	0.05472	54.98

Appendix HD: Experiment 2 Test 4: Measured results

MASS (kg)	FORCE (N)	STARTING VOLTAGE / REFERENCE POINT (V)	VOLTAGE DUE TO APPLIED MASS (V)	AIR GAP LENGTH FROM SENSOR TO TARGET (mm)	CHANGE IN AIR GAP LENGTH FROM REFERENCE POINT (µm)
0	0	5.567	5.567	0.11134	0
0.5	4.905	5.567	5.514	0.11028	1.06
1	9.81	5.555	5.433	0.10866	2.44
1.5	14.715	5.565	5.456	0.10912	2.18
2	19.62	5.589	5.376	0.10752	4.26
2.5	24.525	5.591	5.374	0.10748	4.34
3	29.43	5.605	5.316	0.10632	5.78
3.5	34.335	5.608	5.279	0.10558	6.58
4	39.24	5.633	5.302	0.10604	6.62
4.5	44.145	5.661	5.25	0.105	8.22
5	49.05	5.641	5.069	0.10138	11.44
5.5	53.955	5.639	5.156	0.10312	9.66
6	58.86	5.665	4.857	0.09714	16.16
6.5	63.765	5.646	4.825	0.0965	16.42
7	68.67	5.681	5.025	0.1005	13.12
7.5	73.575	5.696	4.935	0.0987	15.22
8	78.48	5.678	4.985	0.0997	13.86
8.5	83.385	5.701	5.018	0.10036	13.66
9	88.29	5.724	5.044	0.10088	13.6
9.5	93.195	5.734	4.849	0.09698	17.7
FLUX (T)	**FORCE (N)**	**STARTING VOLTAGE / REFERENCE POINT (V)**	**VOLTAGE DUE TO APPLIED FLUX (V)**	**AIR GAP LENGTH FROM SENSOR TO TARGET (mm)**	**CHANGE IN AIR GAP LENGTH FROM REFERENCE POINT (µm)**
0.12	0	6.218	6.218	0.12436	0
0.2315	4.905	6.218	6.169	0.12338	0.98
0.3274	9.81	6.224	6.068	0.12136	3.12
0.4009	14.715	6.213	5.917	0.11834	5.92
0.463	19.62	6.217	5.703	0.11406	10.28
0.5176	24.525	6.206	5.482	0.10964	14.48
0.567	29.43	6.18	5.187	0.10374	19.86
0.6125	34.335	6.171	4.914	0.09828	25.14
0.6548	39.24	6.184	4.672	0.09344	30.24
0.6945	44.145	6.156	4.448	0.08896	34.16
0.732	49.05	6.139	4.308	0.08616	36.62
0.7678	53.955	6.143	4.164	0.08328	39.58
0.802	58.86	6.133	4.035	0.0807	41.96
0.8346	63.765	6.121	3.929	0.07858	43.84
0.866	68.67	6.118	3.823	0.07646	45.9
0.8965	73.575	6.104	3.73	0.0746	47.48
0.926	78.48	5.523	3.046	0.06092	49.54
0.9545	83.385	5.463	2.924	0.05848	50.78
0.982	88.29	5.446	2.828	0.05656	52.36
1.009	93.195	5.356	2.605	0.0521	55.02

Appendix HE: Experiment 2 Test 5: Measured results

MASS (kg)	FORCE (N)	STARTING VOLTAGE / REFERENCE POINT (V)	VOLTAGE DUE TO APPLIED MASS (V)	AIR GAP LENGTH FROM SENSOR TO TARGET (mm)	CHANGE IN AIR GAP LENGTH FROM REFERENCE POINT (μm)
0	0	6.351	6.351	0.12702	0
0.5	4.905	6.351	6.303	0.12606	0.96
1	9.81	6.358	6.247	0.12494	2.22
1.5	14.715	6.37	6.218	0.12436	3.04
2	19.62	6.375	6.151	0.12302	4.48
2.5	24.525	6.385	6.153	0.12306	4.64
3	29.43	6.388	6.147	0.12294	4.82
3.5	34.335	6.418	6.054	0.12108	7.28
4	39.24	6.424	6.092	0.12184	6.64
4.5	44.145	6.452	6.27	0.1254	3.64
5	49.05	6.461	5.878	0.11756	11.66
5.5	53.955	6.482	5.743	0.11486	14.78
6	58.86	6.474	5.847	0.11694	12.54
6.5	63.765	6.514	5.882	0.11764	12.64
7	68.67	6.492	5.692	0.11384	16
7.5	73.575	6.5	5.521	0.11042	19.58
8	78.48	6.492	5.545	0.1109	18.94
8.5	83.385	6.505	5.688	0.11376	16.34
9	88.29	6.489	5.404	0.10808	21.7
9.5	93.195	6.521	5.351	0.10702	23.4

FLUX (T)	FORCE (N)	STARTING VOLTAGE / REFERENCE POINT (V)	VOLTAGE DUE TO APPLIED FLUX (V)	AIR GAP LENGTH FROM SENSOR TO TARGET (mm)	CHANGE IN AIR GAP LENGTH FROM REFERENCE POINT (μm)
0.12	0	6.56	6.56	0.1312	0
0.2315	4.905	6.56	6.502	0.13004	1.16
0.3274	9.81	6.565	6.437	0.12874	2.56
0.4009	14.715	6.595	6.305	0.1261	5.8
0.463	19.62	6.59	6.091	0.12182	9.98
0.5176	24.525	6.572	5.855	0.1171	14.34
0.567	29.43	6.573	5.584	0.11168	19.78
0.6125	34.335	6.583	5.308	0.10616	25.5
0.6548	39.24	6.572	5.095	0.1019	29.54
0.6945	44.145	6.577	4.893	0.09786	33.68
0.732	49.05	6.565	4.744	0.09488	36.42
0.7678	53.955	6.568	4.588	0.09176	39.6
0.802	58.86	6.563	4.492	0.08984	41.42
0.8346	63.765	6.581	4.395	0.0879	43.72
0.866	68.67	6.593	4.323	0.08646	45.4
0.8965	73.575	6.595	4.231	0.08462	47.28
0.926	78.48	5.877	3.444	0.06888	48.66
0.9545	83.385	5.83	3.323	0.06646	50.14
0.982	88.29	5.84	3.24	0.0648	52
1.009	93.195	5.712	2.934	0.05868	55.56

Appendix IA: Experiment 3 Test 1: Measured results

AIR GAP FLUX (T)	CURRENT APPLIED TO COILS (A)	STARTING VOLTAGE / REFERENCE POINT (V)	VOLTAGE DUE TO APPLIED FLUX (V)	AIR GAP LENGTH FROM SENSOR TO TARGET (µm)	CHANGE IN AIR GAP LENGTH FROM REFERENCE POINT (nm)
0.011	0	4.2827	4.2827	85.654	0
0.218	0.6	4.2827	4.282	85.64	14
0.308	0.8	4.2825	4.2814	85.628	22
0.377	1	4.2825	4.2808	85.616	34
0.435	1.2	4.2824	4.2804	85.608	40
0.486	1.3	4.2823	4.28	85.6	46
0.533	1.5	4.2823	4.2796	85.592	54
0.576	1.6	4.2822	4.2792	85.584	60
0.616	1.8	4.2821	4.2788	85.576	66
0.653	2.1	4.2821	4.2785	85.57	72
0.689	2.6	4.2821	4.2781	85.562	80
0.722	3.1	4.282	4.2779	85.558	82
0.754	3.8	4.282	4.2776	85.552	88
0.785	4.6	4.2814	4.2768	85.536	92
0.815	5.5	4.2812	4.2765	85.53	94
0.843	6.6	4.2812	4.2763	85.526	98
0.871	8.2	4.2813	4.2761	85.522	104
0.898	10.3	4.2811	4.2758	85.516	106
0.924	13.1	4.281	4.2754	85.508	112
0.949	16.4	4.2808	4.2753	85.506	110
0.974	20.4	4.2806	4.2749	85.498	114
0.998	24.7	4.2804	4.2747	85.494	114

Appendix IB: Experiment 3 Test 2: Measured results

AIR GAP FLUX (T)	CURRENT APPLIED TO COILS (A)	STARTING VOLTAGE / REFERENCE POINT (V)	VOLTAGE DUE TO APPLIED FLUX (V)	AIR GAP LENGTH FROM SENSOR TO TARGET (µm)	CHANGE IN AIR GAP LENGTH FROM REFERENCE POINT (nm)
0.011	0	4.2646	4.2646	85.292	0
0.218	0.6	4.2647	4.2643	85.286	8
0.308	0.8	4.2649	4.2641	85.282	16
0.377	1	4.2651	4.2639	85.278	24
0.435	1.2	4.2653	4.2637	85.274	32
0.486	1.3	4.2654	4.2634	85.268	40
0.533	1.5	4.2655	4.2633	85.266	44
0.576	1.6	4.2657	4.2632	85.264	50
0.616	1.8	4.2659	4.2632	85.264	54
0.653	2.1	4.2659	4.2629	85.258	60
0.689	2.6	4.2658	4.2627	85.254	62
0.722	3.2	4.2659	4.2626	85.252	66
0.754	3.9	4.266	4.2625	85.25	70
0.785	4.7	4.2661	4.2624	85.248	74
0.815	5.6	4.2661	4.2623	85.246	76
0.843	6.7	4.2662	4.2621	85.242	82
0.871	8.3	4.2662	4.262	85.24	84
0.898	10.5	4.2662	4.2619	85.238	86
0.924	13.3	4.2663	4.2618	85.236	90
0.949	16.7	4.2662	4.2616	85.232	92
0.974	20.7	4.266	4.2614	85.228	92
0.998	25.2	4.266	4.2612	85.224	96

Appendix IC: Experiment 3 Test 3: Measured results

AIR GAP FLUX (T)	CURRENT APPLIED TO COILS (A)	STARTING VOLTAGE / REFERENCE POINT (V)	VOLTAGE DUE TO APPLIED FLUX (V)	AIR GAP LENGTH FROM SENSOR TO TARGET (µm)	CHANGE IN AIR GAP LENGTH FROM REFERENCE POINT (nm)
0.011	0	4.269	4.269	85.38	0
0.218	0.6	4.2692	4.2686	85.372	12
0.308	0.8	4.2692	4.2682	85.364	20
0.377	1	4.2693	4.2678	85.356	30
0.435	1.2	4.2693	4.2676	85.352	34
0.486	1.3	4.2694	4.2674	85.348	40
0.533	1.5	4.2694	4.2671	85.342	46
0.576	1.6	4.2694	4.2668	85.336	52
0.616	1.8	4.2695	4.2666	85.332	58
0.653	2.1	4.2694	4.2662	85.324	64
0.689	2.6	4.2693	4.2659	85.318	68
0.722	3.2	4.2694	4.2658	85.316	72
0.754	3.8	4.2694	4.2657	85.314	74
0.785	4.6	4.2694	4.2654	85.308	80
0.815	5.6	4.2694	4.2652	85.304	84
0.843	6.7	4.2693	4.265	85.3	86
0.871	8.2	4.2693	4.2649	85.298	88
0.898	10.5	4.2693	4.2647	85.294	92
0.924	13.3	4.2691	4.2644	85.288	94
0.949	16.7	4.269	4.2641	85.282	98
0.974	20.7	4.2688	4.264	85.28	96
0.998	25.2	4.2687	4.2638	85.276	98

Appendix ID: Experiment 3 Test 4: Measured results

AIR GAP FLUX (T)	CURRENT APPLIED TO COILS (A)	STARTING VOLTAGE / REFERENCE POINT (V)	VOLTAGE DUE TO APPLIED FLUX (V)	AIR GAP LENGTH FROM SENSOR TO TARGET (µm)	CHANGE IN AIR GAP LENGTH FROM REFERENCE POINT (nm)
0.011	0	4.2792	4.2792	85.584	0
0.218	0.6	4.2792	4.2786	85.572	12
0.308	0.8	4.279	4.278	85.56	20
0.377	1	4.279	4.2776	85.552	28
0.435	1.2	4.2791	4.2773	85.546	36
0.486	1.3	4.2791	4.2771	85.542	40
0.533	1.4	4.279	4.2767	85.534	46
0.576	1.6	4.2789	4.2764	85.528	50
0.616	1.8	4.279	4.2762	85.524	56
0.653	2.1	4.279	4.276	85.52	60
0.689	2.6	4.279	4.2759	85.518	62
0.722	3.1	4.279	4.2756	85.512	68
0.754	3.7	4.279	4.2754	85.508	72
0.785	4.5	4.2789	4.2753	85.506	72
0.815	5.4	4.279	4.2752	85.504	76
0.843	6.5	4.279	4.275	85.5	80
0.871	8	4.2788	4.2747	85.494	82
0.898	10	4.2789	4.2746	85.492	86
0.924	12.8	4.2787	4.2743	85.486	88
0.949	16	4.2786	4.2741	85.482	90
0.974	20	4.2785	4.274	85.48	90
0.998	24.2	4.2784	4.2738	85.476	92

Appendix IE: Experiment 3 Test 5: Measured results

AIR GAP FLUX (T)	CURRENT APPLIED TO COILS (A)	STARTING VOLTAGE / REFERENCE POINT (V)	VOLTAGE DUE TO APPLIED FLUX (V)	AIR GAP LENGTH FROM SENSOR TO TARGET (µm)	CHANGE IN AIR GAP LENGTH FROM REFERENCE POINT (nm)
0.011	0	4.2726	4.2723	85.446	6
0.218	0.6	4.2724	4.2719	85.438	10
0.308	0.8	4.2724	4.2714	85.428	20
0.377	1	4.2726	4.2711	85.422	30
0.435	1.2	4.2726	4.2709	85.418	34
0.486	1.3	4.2726	4.2706	85.412	40
0.533	1.5	4.2726	4.2703	85.406	46
0.576	1.6	4.2726	4.2701	85.402	50
0.616	1.8	4.2727	4.27	85.4	54
0.653	2.1	4.2728	4.2698	85.396	60
0.689	2.6	4.2727	4.2695	85.39	64
0.722	3.1	4.2727	4.2693	85.386	68
0.754	3.8	4.2728	4.2692	85.384	72
0.785	4.6	4.2728	4.2691	85.382	74
0.815	5.4	4.2732	4.269	85.38	84
0.843	6.4	4.2731	4.2689	85.378	84
0.871	7.8	4.2731	4.2688	85.376	86
0.898	9.8	4.273	4.2686	85.372	88
0.924	12.4	4.2731	4.2685	85.37	92
0.949	15.6	4.273	4.2683	85.366	94
0.974	19.4	4.2729	4.2682	85.364	94
0.998	23.7	4.2728	4.268	85.36	96

Appendix IF: Experiment 3 Test 6: Measured results

AIR GAP FLUX (T)	CURRENT APPLIED TO COILS (A)	STARTING VOLTAGE / REFERENCE POINT (V)	VOLTAGE DUE TO APPLIED FLUX (V)	AIR GAP LENGTH FROM SENSOR TO TARGET (µm)	CHANGE IN AIR GAP LENGTH FROM REFERENCE POINT (nm)
0.011	0	4.276	4.276	85.52	0
0.218	0.6	4.276	4.2754	85.508	12
0.308	0.8	4.276	4.2749	85.498	22
0.377	1	4.276	4.2745	85.49	30
0.435	1.1	4.276	4.2742	85.484	36
0.486	1.3	4.276	4.274	85.48	40
0.533	1.4	4.276	4.2737	85.474	46
0.576	1.6	4.2761	4.2734	85.468	54
0.616	1.8	4.2761	4.2732	85.464	58
0.653	2.1	4.2761	4.273	85.46	62
0.689	2.5	4.2761	4.2727	85.454	68
0.722	3	4.2761	4.2725	85.45	72
0.754	3.7	4.2761	4.2724	85.448	74
0.785	4.4	4.2761	4.2722	85.444	78
0.815	5.3	4.2761	4.272	85.44	82
0.843	6.3	4.2762	4.2719	85.438	86
0.871	7.8	4.2762	4.2716	85.432	92
0.898	9.8	4.276	4.2715	85.43	90
0.924	12.3	4.2761	4.2714	85.428	94
0.949	15.5	4.2761	4.2713	85.426	96
0.974	19.4	4.276	4.2711	85.422	98
0.998	23.5	4.2759	4.2709	85.418	100

Appendix IG: Experiment 3 Test 7: Measured results

AIR GAP FLUX (T)	CURRENT APPLIED TO COILS (A)	STARTING VOLTAGE / REFERENCE POINT (V)	VOLTAGE DUE TO APPLIED FLUX (V)	AIR GAP LENGTH FROM SENSOR TO TARGET (µm)	CHANGE IN AIR GAP LENGTH FROM REFERENCE POINT (nm)
0.011	0	4.2682	4.2682	85.364	0
0.218	0.6	4.2682	4.2677	85.354	10
0.308	0.8	4.2682	4.2672	85.344	20
0.377	1	4.2682	4.2668	85.336	28
0.435	1.2	4.2682	4.2665	85.33	34
0.486	1.3	4.2682	4.2662	85.324	40
0.533	1.4	4.2682	4.2659	85.318	46
0.576	1.6	4.2683	4.2657	85.314	52
0.616	1.8	4.2684	4.2655	85.31	58
0.653	2	4.2684	4.2653	85.306	62
0.689	2.5	4.2684	4.2651	85.302	66
0.722	3.1	4.2683	4.2648	85.296	70
0.754	3.7	4.2682	4.2646	85.292	72
0.785	4.5	4.2684	4.2646	85.292	76
0.815	5.4	4.2683	4.2642	85.284	82
0.843	6.4	4.2684	4.2642	85.284	84
0.871	7.8	4.2683	4.264	85.28	86
0.898	9.9	4.2682	4.2638	85.276	88
0.924	12.5	4.2682	4.2637	85.274	90
0.949	15.7	4.2682	4.2635	85.27	94
0.974	19.6	4.2681	4.2634	85.268	94
0.998	23.8	4.268	4.2632	85.264	96

Appendix IH: Experiment 3 Test 8: Measured results

AIR GAP FLUX (T)	CURRENT APPLIED TO COILS (A)	STARTING VOLTAGE / REFERENCE POINT (V)	VOLTAGE DUE TO APPLIED FLUX (V)	AIR GAP LENGTH FROM SENSOR TO TARGET (µm)	CHANGE IN AIR GAP LENGTH FROM REFERENCE POINT (nm)
0.011	0	4.2617	4.2617	85.234	0
0.218	0.6	4.2617	4.2612	85.224	10
0.308	0.8	4.2617	4.2607	85.214	20
0.377	1	4.2617	4.2603	85.206	28
0.435	1.2	4.2617	4.26	85.2	34
0.486	1.3	4.2621	4.2601	85.202	40
0.533	1.4	4.2621	4.2598	85.196	46
0.576	1.6	4.2621	4.2595	85.19	52
0.616	1.8	4.262	4.2592	85.184	56
0.653	2.1	4.2621	4.259	85.18	62
0.689	2.6	4.262	4.2589	85.178	62
0.722	3.1	4.2621	4.2587	85.174	68
0.754	3.8	4.2621	4.2585	85.17	72
0.785	4.5	4.262	4.2583	85.166	74
0.815	5.4	4.262	4.2581	85.162	78
0.843	6.5	4.262	4.258	85.16	80
0.871	8	4.2621	4.258	85.16	82
0.898	10.1	4.2621	4.2578	85.156	86
0.924	12.8	4.262	4.2576	85.152	88
0.949	16	4.262	4.2575	85.15	90
0.974	20	4.262	4.2573	85.146	94
0.998	24.2	4.2619	4.2571	85.142	96

Appendix II: Experiment 3 Test 9: Measured results

AIR GAP FLUX (T)	CURRENT APPLIED TO COILS (A)	STARTING VOLTAGE / REFERENCE POINT (V)	VOLTAGE DUE TO APPLIED FLUX (V)	AIR GAP LENGTH FROM SENSOR TO TARGET (µm)	CHANGE IN AIR GAP LENGTH FROM REFERENCE POINT (nm)
0.011	0	4.3153	4.3153	86.306	0
0.218	0.6	4.3154	4.3148	86.296	12
0.308	0.8	4.3153	4.3141	86.282	24
0.377	1	4.3151	4.3134	86.268	34
0.435	1.1	4.3149	4.3129	86.258	40
0.486	1.3	4.3147	4.3123	86.246	48
0.533	1.4	4.3145	4.3118	86.236	54
0.576	1.6	4.3145	4.3116	86.232	58
0.616	1.7	4.3143	4.3112	86.224	62
0.653	2	4.3141	4.3107	86.214	68
0.689	2.4	4.3139	4.3102	86.204	74
0.722	2.9	4.3135	4.3097	86.194	76
0.754	3.5	4.3132	4.3091	86.182	82
0.785	4.2	4.3128	4.3087	86.174	82
0.815	5	4.3126	4.3082	86.164	88
0.843	6	4.3124	4.3078	86.156	92
0.871	7.3	4.312	4.3072	86.144	96
0.898	9	4.3114	4.3066	86.132	96
0.924	11.4	4.311	4.3061	86.122	98
0.949	14.2	4.3106	4.3056	86.112	100
0.974	17.7	4.3103	4.305	86.1	106
0.998	21.7	4.3099	4.3046	86.092	106

Appendix IJ: Experiment 3 Test 10: Measured results

AIR GAP FLUX (T)	CURRENT APPLIED TO COILS (A)	STARTING VOLTAGE / REFERENCE POINT (V)	VOLTAGE DUE TO APPLIED FLUX (V)	AIR GAP LENGTH FROM SENSOR TO TARGET (µm)	CHANGE IN AIR GAP LENGTH FROM REFERENCE POINT (nm)
0.011	0	4.2984	4.2984	85.968	0
0.218	0.6	4.2986	4.2981	85.962	10
0.308	0.8	4.2987	4.2977	85.954	20
0.377	1	4.2987	4.2974	85.948	26
0.435	1.2	4.299	4.2973	85.946	34
0.486	1.3	4.2992	4.2971	85.942	42
0.533	1.4	4.2993	4.297	85.94	46
0.576	1.6	4.2995	4.2968	85.936	54
0.616	1.7	4.2994	4.2965	85.93	58
0.653	2	4.2996	4.2965	85.93	62
0.689	2.4	4.2995	4.2962	85.924	66
0.722	2.9	4.2994	4.296	85.92	68
0.754	3.5	4.2995	4.2959	85.918	72
0.785	4.2	4.2995	4.2957	85.914	76
0.815	5.1	4.2997	4.2956	85.912	82
0.843	6	4.2996	4.2954	85.908	84
0.871	7.3	4.2996	4.2952	85.904	88
0.898	9	4.2997	4.2952	85.904	90
0.924	11.4	4.2997	4.2951	85.902	92
0.949	14.2	4.2998	4.295	85.9	96
0.974	17.8	4.2997	4.2948	85.896	98
0.998	21.8	4.2997	4.2946	85.892	102